Nonlinear Chemical Dynamics and Synchronization

A Dissertation

Presented to

The Faculty of the Graduate School of Arts and Sciences

Brandeis University

Martin A. Fisher School of Physics

Seth Fraden, Department of Physics, Advisor

In Partial Fulfillment

of the Requirements for the Degree

Doctor of Philosophy

by

Ning Li

October, 2014

This dissertation, directed and approved by Ning Li's committee, has been accepted and approved by the Graduate Faculty of Brandeis University in partial fulfillment of the requirements for the degree of:

DOCTOR OF PHILOSOPHY

Eric Chasalow, Dean of Arts and Sciences

Dissertation Committee:

Seth Fraden, Department of Physics, Chair

Jané Kondev, Department of Physics

Irving R. Epstein, Department of Chemistry

To,

Father & Mother

To,

My wife Lijie

Acknowledgments

I wish to express my sincere thanks to my adviser, Prof. Seth Fraden, for his guidance and support in my research career at Brandeis.

I would like to thank Prof. Irving Epstein and Prof. Bing Xu, for their kindly support in the collaborations with our group. I would also like to thank Prof. Bulbul Chakraborty, Prof. Aparna Baskaran and Prof. Michael Hagan, for helpful and inspiring discussions.

I am thankful to Dr. Hector Gonzalez-Ochoa, Dr. Jorge Delgado, Dr. Marcin Leda and Dr. Ye Zhang, from whom I have learned a lot during our collaborations. I am also thankful to Dr. Francesco Pontiggia for his technical support on cluster computing.

I thank my current and former colleagues in Fraden group, Dr. Dongshin Kim, Dr. Michael Heymann, Dr. Sathish Akella, Mr. Nathan Tompkins and Mr. Camille Girabawe, for their help in my work.

Last but not least, I thank the support from the National Science Foundation Brandeis MRSEC-0820492 and use of the MRSEC microfluidics facility and the support from the Army Research Office, grant W911 NF-09-1-0496.

Abstract

Nonlinear Chemical Dynamics and Synchronization

A dissertation presented to the Faculty of
the Graduate School of Arts and Sciences of
Brandeis University, Waltham, Massachusetts

by Ning Li

Alan Turing's work on morphogenesis, more than half a century ago, continues to motivate and inspire theoretical and experimental biologists even today. That said, there are very few experimental systems for which Turing's theory is applicable. In this thesis we present an experimental reaction-diffusion system ideally suited for testing Turing's ideas in synthetic "cells" consisting of microfluidically produced surfactant-stabilized emulsions in which droplets containing the Belousov-Zhabotinsky (BZ) oscillatory chemical reactants are dispersed in oil.

The BZ reaction has become the prototype of nonlinear dynamics in chemistry and a preferred system for exploring the behavior of coupled nonlinear oscillators. Our system consists of a surfactant stabilized monodisperse emulsion of drops of aqueous BZ solution dispersed in a continuous phase of oil. In contrast to biology, here the chemistry is understood, rate constants are measured and interdrop coupling is purely diffusive. We explore a large set of parameters through control of rate constants, drop size, spacing, and spatial arrangement of the drops in lines and rings in one-dimension (1D) and hexagonal arrays in two-dimensions (2D). The Turing model is regarded as a metaphor for morphogenesis in biology but not for prediction. Here, we develop a quantitative and falsifiable reaction-diffusion model that we experimentally test with synthetic cells. We quantitatively establish the extent to which the Turing model in 1D describes both stationary pattern formation and temporal synchronization of chemical oscillators via reaction-diffusion and in 2D demonstrate that chemical morphogenesis drives physical differentiation in synthetic cells.

Contents

List of Tables

List of Figures

Chapter 1

Introduction

Men are born ignorant, not stupid.

They are made stupid by education.

Bertrand Russell

Alan Turing (1912 - 1954), English mathematician and logician, was one of the most influential scientists in history. He is often considered to be the father of modern computer science. Less well known than his contribution in computer science and artificial intelligence, *The Chemical Basis of Morphogenesis*, written in 1952 by Turing[1], was a ground breaking work on mathematical biology that continues to motivate and inspire theoretical and experimental biologists even today. In this paper, he described how in circular arrays of identical biological cells and continuous rings of tissue diffusion can interact with chemical reactions to generate up to six spatial-temporal periodic chemical structures. In the paper he wrote,

> "It is suggested that a system of chemical substances, called morphogens, reacting together and diffusing through a tissue, is adequate to account for the main phenomena of morphogenesis. Such a system, although it may originally be quite homogeneous, may later develop a pattern or structure due to an instability of the homogeneous equilibrium, which is triggered off by random disturbances. Such

reaction-diffusion systems are considered in some detail in the case of an isolated ring of cells, a mathematically convenient, though biologically unusual system. The investigation is chiefly concerned with the onset of instability. It is found that there are six essentially different forms which this may take. In the most interesting form stationary waves appear on the ring. It is suggested that this might account, for instance, for the tentacle patterns on *Hydra* and for whorled leaves..."

After 60 years the Turing mechanism remains controversial in biology because of uncertainty in both the reaction kinetics and transport mechanisms. While numerous examples in biological tissue patterning, such as lateral inhibition between contacting cells in Delta-Notch signaling[2, 3, 4], resemble the reaction-diffusion (RD) systems Turing proposed, only a very limited set of biological patterns have been established to be based on RD Turing instabilities[5, 6].

In chemistry, all six Turing patterns have been established in continuous systems on the centimeter scale[7, 8], but not for diffusively coupled cells on the micron scale. Here we report an experimental reaction-diffusion system ideally suited for testing Turing's ideas in synthetic "cells" consisting of microfluidically produced surfactant-stabilized emulsions[9, 10] in which droplets containing the Belousov-Zhabotinsky (BZ) oscillatory chemical reactants[11] are dispersed in oil. In contrast to biology, here the chemistry is understood, rate constants are measured and interdrop coupling is purely diffusive.

The BZ reaction[11], the metal-ion-catalyzed oscillatory oxidation of an organic substrate, typically malonic acid (MA), by acidic bromate, has become the prototype of nonlinear dynamics in chemistry[12] and a preferred system for exploring the behavior of coupled nonlinear oscillators[13, 14]. Microfluidically produced emulsions of BZ solution are a convenient chemical experimental system which exhibits multiple phenomena that can be semi-quantitatively explained by Turing's RD mechanism[15]. Microfluidic techniques pro-

vide a convenient method for emulsifying BZ solution into monodispersed droplets with the dimension of tens to hundreds of microns. The diffusive coupling of the chemical species acting as activators and inhibitors between BZ aqueous droplets suspended in a continuous oil media render the BZ emulsion system ideal for the study of synchronization and pattern formation in networks of coupled nonlinear chemical oscillators.

Our system consists of a surfactant stabilized[16] monodisperse emulsion of drops of aqueous BZ solution whose size ranges from 20 μm to 200 μm diameter dispersed in a continuous phase of oil[9, 10]. The drops are surfactant-stabilized to prevent coalescence[16]. Chemical coupling between drops is mediated through a small subset of less polar intermediates: an inhibitory component, bromine (Br_2), and two excitatory components, bromine dioxide radical ($BrO_2^{\bullet}$) and bromous acid ($HBrO_2$), which diffuse from drop to drop through the intervening oil[17]. Because the inhibitory bromine strongly partitions into the oil, whereas the excitatory bromous acid does so only weakly, we satisfy the long-range inhibition and short-range excitation condition needed for the stationary Turing state[18]. Since the system is closed and the BZ reactants are not replenished, the reaction lasts about 100 oscillations until the final uniform equilibrium state is approached. However, the system evolves sufficiently slowly that the system can adiabatically adopt the dynamical states predicted by Turing for open systems[19, 9, 10].

In the next chapter, we will first introduce our experimental and computational methods used in the rest of this thesis. Then we will describe in detail the studies about one-dimensional (1D) BZ oscillators in Chapter 3.

For samples composed of many drops and in the absence of well defined initial conditions, the anti-phase attractor, in which adjacent droplets oscillate 180° out of phase, is observed for relatively weak coupling in 1D arrays. The initial transients in the phase difference between neighboring droplets persist until the BZ reactants are exhausted. In order to make quantitative comparison with theory for limited oscillations in closed systems, we use photo-

sensitive $Ru(bipy)_3^{2+}$-catalyzed BZ droplets and set both boundary and initial conditions of arrays of small numbers of oscillating BZ droplets with a programmable illumination source. In these small collections of droplets, transient patterns decay rapidly and we observe several more complex attractors, including ones in which some adjacent droplets are in-phase. Excellent agreement between experiment and numerical simulations is achieved.

In closed system, the malonic acid concentration decreases as the reaction proceeds. Starting with a low initial malonic acid concentration, we observe a series of attractors as a function of time in the following order: anti-phase attractors; in-phase attractors, which evolve into traveling waves; and mixed modes that contain either regions of in-phase droplets separated by anti-phase oscillators, or in-phase oscillators combined with non-oscillatory droplets. Most of the observations are consistent with numerical models of the BZ reaction in which components that participate in the excitatory (bromine dioxide and bromous acid) and inhibitory (bromine) pathways diffuse between the droplets. Three kinds of models (point model, phase model and finite element model) are used to quantitatively assess the inter-drop coupling strength as a function of drop separation, drop size and malonic acid concentration.

In Chapter 4, we will demonstrate the results for two-dimensional (2D) patterns and Turing morphogenesis. We summarize all the 1D and 2D results into one phase diagram with Turing linear stability analysis and nonlinear simulation side by side. Further, we examine 2D arrays of drops in more detail through experiments and finite element simulations. We describe the transition from oscillatory to stationary chemical states with increasing coupling strength, as well as the trend that the ratio of stationary oxidized to stationary reduced drops increases with coupling strength. We will also provide simulation results to quantify the degree of chemical heterogeneity of BZ drops sufficient to generate mixed oscillatory and stationary patterns in this chapter. Last but not least, we will demonstrate the evidence of Turing morphogenesis.

Chapter 2

Experimental & Computational Methods

There is much pleasure to be gained from useless knowledge.

Bertrand Russell

In this chapter, we summarize some of the experimental and computational techniques used in our BZ oscillator studies. Some of the data that are briefly mentioned here as examples will be explained more thoroughly in the following chapters.

2.1 Experimental Methods

2.1.1 Chemical Preparation

Our BZ solution in droplets is usually composed of six components (supplied by Sigma-Aldrich): sulfuric acid (H_2SO_4), malonic acid (MA, $CH_2(COOH)_2$), sodium bromide (NaBr), sodium bromate($NaBrO_3$), ferroin redox indicator (1, 10 - Phenanthroline iron(II) sulfate complex, $[Fe(C_{12}H_8N_2)_3]SO_4$), and $Ru(bipy)_3$ (Ruthenium - tris (2,2'- bipyridyl) dichloride,

$C_{30}H_{24}Cl_2N_6Ru \cdot 6H_2O$). We normally write reduced form of ferroin (the useful part without counterion) as $Fe(phen)_3^{2+}$ or Fe(II), oxidized form $Fe(phen)_3^{3+}$ or Fe(III); and we write reduced form of $Ru(bipy)_3$ as $Ru(bipy)_3^{2+}$ or Ru(II), oxidized form $Ru(bipy)_3^{3+}$ or Ru(III).

Most of these chemicals can be stored at room temperature in glass bottles, except that $Ru(bipy)_3$ is light sensitive and should be covered with aluminum foil to avoid light.

The oil separating aqueous BZ droplets is a fluorinated oil HFE 7500 (3 - ethoxy - 1,1,1,2,3,4,4,5,5,6,6,6 - dodecafluoro - 2 - trifluoromethyl - hexane, 3M Corp., St. Paul, MN, USA). We add a surfactant "EA" (2% v/v) to prevent the coalescence of the BZ droplets. EA (RainDance Technologies, Lexington, MA, USA) is a fluorinated surfactant consisting of a PEG - PFPE amphiphilic block copolymer. The choice of surfactant is crucial as bromine oxidizes double bonds. Therefore surfactants with unsaturated alkyl tails, such as Span80, are unsuitable because they consume the available bromine, thereby preventing BZ oscillation[19]. We note that a very satisfactory alternative is now commercially available (RAN Biotechnologies, Inc.).

A typical recipe of BZ mixture in a droplet is listed here as the "default condition" in the unit of M (molar, mol/L): $[H_2SO_4] = 0.08$ M = 80 mM, [MA] = 0.4 M = 400 mM, [NaBr] = 0.01 M = 10 mM, $[NaBrO_3] = 0.3$ M = 300 mM, [Ferroin] = 3 mM, $[Ru(bipy)_3] = 0.4$ mM, both in reduced form. This default condition will be frequently mentioned in the rest of the thesis. However, sometimes we also changed some of the concentrations in our experiments such as lower or higher [MA], with or without NaBr, with or without $Ru(bipy)_3$, etc. We will specify these changes like "default condition with 60 mM [MA]", "default condition without NaBr", "default condition without $Ru(bipy)_3$", etc. The unspecified species would be the same as default condition, so that the chemical conditions would be clear without redundancy.

2.1.2 Microfluidics: Droplet Generator

To generate chemically and physically uniform BZ droplets of some 1 nL in volume, we use poly - dimethyl - siloxane (PDMS) based microfluidic device (sometimes referred as PDMS chip or microfluidic chip). The concept of our chip design is sketched in Fig. 2.1.

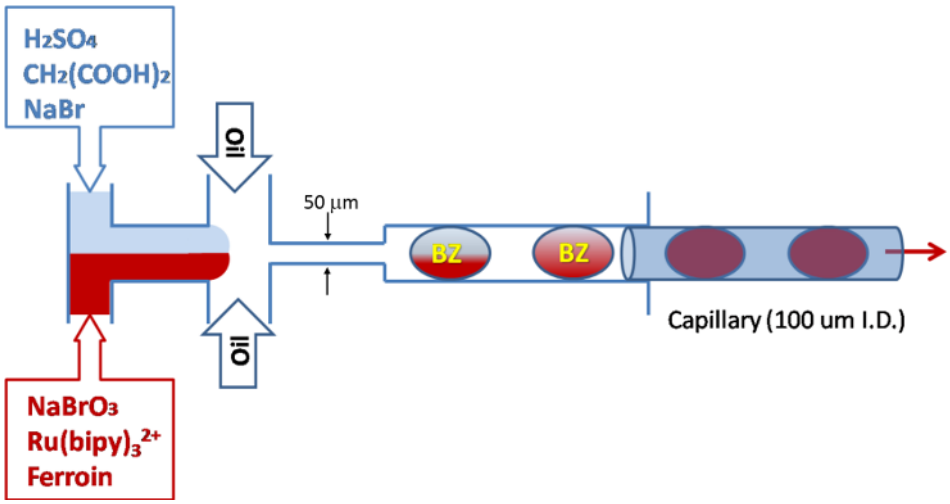

Figure 2.1: Schematic drawing of the microfluidic PDMS drop generator. At left, two different aqueous streams containing complementary reactants of the BZ solution are injected into the drop generator (light blue and red). The streams merge and co-flow down a central channel, meeting two perpendicular oil flows that generate BZ droplets in a nozzle. The co-flow of the BZ solution is preserved immediately after the drops are formed, but complete mixing takes place in less than 1 s. A glass capillary (100 μm ID) was inserted in the PDMS chip a few millimetres downstream from the nozzle to collect the BZ droplets. Adapted from previous work[10].

This chip has two inlets for injecting equal amounts of complementary components of the aqueous BZ solution into a central channel, where the two BZ reactant streams merge and form a co-flow without mixing. All chemicals are injected at six times the final desired concentration in the BZ droplets as we used equal volume from each of the six species. After merging, the BZ co-flow encounters two streams of fluorinated oil entering perpendicularly from both sides. The oil and BZ streams are immiscible and flow into a 50 μm nozzle, which produces droplets by flow-focusing[20, 21]. After their formation, the droplets enter a hydrophobized glass capillary of 100 μm internal diameter (I.D.) previously inserted into

the microfluidic chip and we have a system of one-dimensional (1D) diffusively coupled BZ oscillators if the drops are larger than the capillary I.D. (droplets larger than the capillary diameter distort into spherocylinders). The experiments cannot be conducted in PDMS devices because bromine is soluble in PDMS, which allows so much bromine to leave the drops that the oscillations cease. The outlet channel of the PDMS chip has a width of 150 μm and height of 40 μm to ensure a snug fit for the glass capillary, which has an outer diameter of 170 μm. The capillaries are hydrophobized using a vacuum chamber in which the capillaries and a small amount of liquid (tridecafluoro - 1,1,2,2 - tetrahydrooctyl) trichlorosilane are placed. We reduce the pressure in order to evaporate the silane, which enters the capillaries via diffusion. The trichlorosilane group of this molecule reacts with the oxygen groups of the silica on the internal glass surface, covering the surface with hydrophobic fluorinated carbon tails[22]. After two hours in the vacuum chamber, which is sufficient for hydrophobizing the capillaries, we remove the capillaries. Air stops the reaction, because oxygen reacts with the chlorosilane groups.

More Details and Personal Experience

Sometimes we treat newly made PDMS chips with Aquapel (Aquapel Glass Treatment, Pittsburgh Glass Works LLC, Pittsburgh, PA) to increase the hydrophobicity of the PDMS channel and thereby improve the performance of the chip.

It is important to monitor the co-flow and only collect emulsions during conditions when the flow is stable. We place both catalysts in the same co-flow, thereby generating one colored stream and one clear stream, making it simple to visualize the steady state flow that is necessary to ensure that all drops have identical chemical compositions.

The total flow rate is typically about 1000 μL/hr (for example, 300 μL/hr for both BZ channels and 400 μL/hr for the oil channel). The size of BZ droplets mainly depend on the nozzle size in the design. But changing flow rate can also change the drop size to a certain

degree: inceasing total flow rate and increasing oil/BZ flow rate ratio will decrease the drop size; decreasing total flow rate and decreasing oil/BZ flow rate ratio will increase the drop size.

2.1.3 Optics: Programmable Illumination

Capillaries containing identical, equidistant BZ droplets were sealed on both ends with commercial epoxy (Quick-Cure 5min epoxy, Bob Smith Ind.) on a microscope slide and observed with a CCD camera through a homemade microscope with Köhler illumination[23]. We observe droplets placed in the central part of the capillary, at least 15 droplets away from the epoxy seal. Typically, more than 100 drops are contained in each capillary.

Exposure of the $Ru(bipy)_3$ catalyzed BZ reaction solution to 450 nm (blue) light triggers the photochemical production of bromide[24, 25], inhibiting the BZ oscillations and forcing ferroin into its reduced state. This phenomenon offers a strategy to externally control and/or drive the droplet state in a programmable way. To accomplish this goal, we built the experimental setup shown in Fig. 2.2, similar to those employed for maskless photolithography purposes[26, 27, 28].

Lenses L1 and L2 (f1 = f2 = 30 mm) form a Köhler illumination optical path. Ferroin, the catalyst, which also serves as an indicator for the oscillation, has an absorption peak near 510 nm[29]. We accordingly use a cyan LED [Lumiled, LXML-PE01-0050] as a light source for observation and an interference filter centered at 515 nm to narrow the incident wavelength. Therefore the reduced state of ferroin, which is dark red, appears dark in the black and white camera due to absorbance of the transmitted light and the oxidized state (blue) is bright.

The projector arm consists of a LCD computer projector (NEC VT800), which uses three 0.63" LCDs of 1024 x 768 pixels resolution to display color images. Lens L3, a continuous variable zoom lens with a focal distance range of f = 18.9 to 22.7 mm forms a 4x reduced

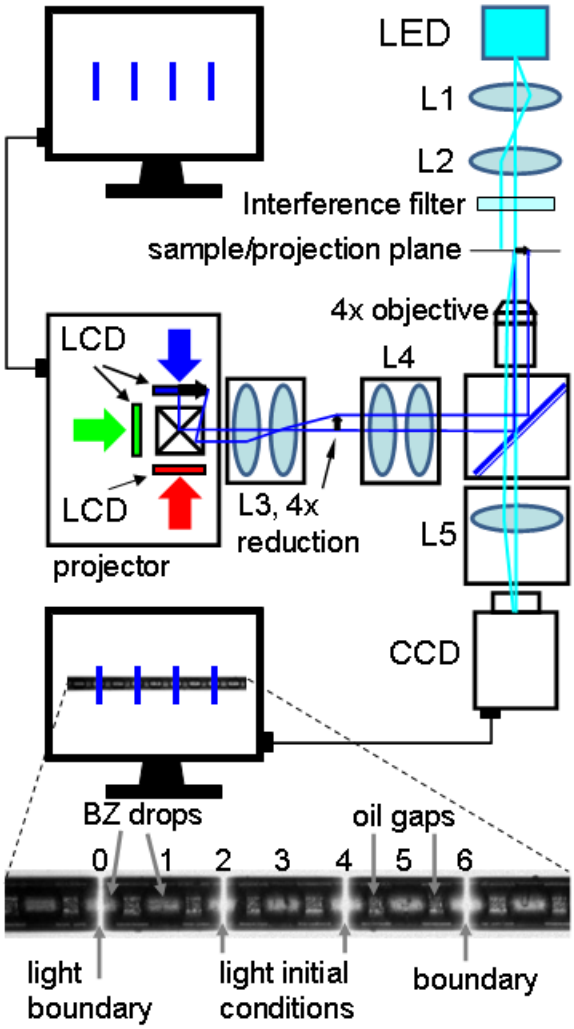

Figure 2.2: Schematic drawing of programmable illumination. Optical path for programmable illumination and optical microscope using transmitted light. A consumer electronics computer projector was modified to project an image onto the capillaries containing the BZ micro-droplets. Programs, such as Microsoft PowerPoint, were used to create patterned illumination. Photograph: section of a capillary of 100 μm diameter showing 9 BZ drops. The outermost lines of light, labeled "boundary", remain illuminated for the duration of the experiment, suppressing oscillations and thereby isolating the five drops between the light induced boundaries from the rest of the drops in the capillary. To establish initial conditions, the five isolated drops are exposed to light for one oscillation period and another two drops receive additional illumination, labeled "initial condition", to phase shift these two with respect to the other drops. Adapted from previous work[10].

image of the computer projector LCD. For this particular computer projector, we were able to remove the manufacturer's projector lens and remount it with its direction reversed so that instead of magnifying the image located on the three LCDs, the lens (L3) reduces the image. Lens L4 (a discarded 35mm film Minolta photographic lens, f = 50 mm) and the microscope objective (Olympus 4X, RMS4X, f = 45mm) together form an infinite conjugate lens pair through the beam-splitter [Chroma 21000 50/50]. The pair transfers the LCD image formed by L3 onto the sample plane with roughly a 1:1 magnification. The tube lens of the objective, lens L5 (Olympus, f = 180 mm), and the microscope objective form another infinite conjugate pair lens that transfers the sample image onto the CCD sensor.

The contrast ratio between "on" and "off" pixels in these LCD computer projectors is about 180:1. A more significant problem is leakage of light through the projector in the off state. In some circumstances this leakage light can influence the experiments, in which case we insert a neutral density filter to lower this background light enough so that it does not affect the period of the BZ oscillations, but still allows enough transmitted light so that when the projector is on there is sufficient light to suppress the BZ oscillation. Typically, to illuminate the samples we use 90 μW intensity of 510 nm wavelength light integrated over the field of view of approximately 8 mm^2. The computer projector has three colors; RGB, each with 8 bits of intensity. To synchronize the BZ reaction we set the R and G values to zero and use B only, because that is the color for which the Ru(bipy)$_3$ is most sensitive. When the blue is fully turned on (B = 255), the intensity over the entire 8 mm^2 area is 3.6 mW. When the blue is turned off (B = 0), light leaks through the LCDs giving an integrated intensity of 20 μW. To synchronize drops, we use patterned illumination with B = 150.

This approach allows us to perform spatio - temporal manipulation of the BZ reaction with a spatial resolution of a single drop and a time resolution of 1 s. In order to minimize the effect on neighboring drops, the intensity of the light is set at the minimal level necessary to suppress oscillation in the illuminated drops. In this way, a localized light pulse on a par-

ticular droplet of interest suppresses its oscillation for the duration of illumination, thereby allowing the phase of the oscillator to be set photochemically. This programmable illumination permits the initial phase of each member of a chosen set of droplets to be arbitrarily specified. As described in more detail below, droplets held by constant illumination in the reduced state of the catalyst can act to establish constant chemical boundary conditions in a 1D array, so with the use of a programmable computer projector we are able to control both the boundary and initial conditions of a set of coupled nonlinear chemical oscillators. Our setup allows the simultaneous spatial and temporal illumination of up to 30 droplets individually in a 100 μm capillary.

We can image up to 100 droplets (in a linear array) with a different lower magnification setup, but are no longer able to independently illuminate individual droplets. When we study 100 droplets we illuminate the entire capillary with uniform, bright light in order to set all the drops in-phase.

2.1.4 Data Analysis

From digital images captured at constant rate (normally 2 - 5 s per frame) we extract a single row of pixels from each frame along the center of the cylindrical capillary. So each row of pixels represents the full spatial information of the system (i.e. brightness of all droplets) for that moment. We then accumulate these rows of pixels in the natural temporal sequence to build the experimental space-time plots as shown in Fig. 2.3. In the space-time plot, each thin white line parallel to the space axis in each BZ droplet corresponds to oxidation of the catalyst ferroin from Fe(II) to Fe(III), which occurs in each cycle of this redox oscillation. The dark regions between the narrow white lines in time axis correspond to intervals during which the catalyst is at reduced form. The period of BZ oscillation in one droplet is the shortest time this drop spend to repeat a previous status. The thin white lines in the space time plot provided a convenient method for defining the periods, and further more, the phase

of each droplet at any time. The percent of time (within one period) the catalyst spends in oxidized state is called the duty cycle. We will discuss in more detail later on about the duty cycle and how it depends on chemical conditions.

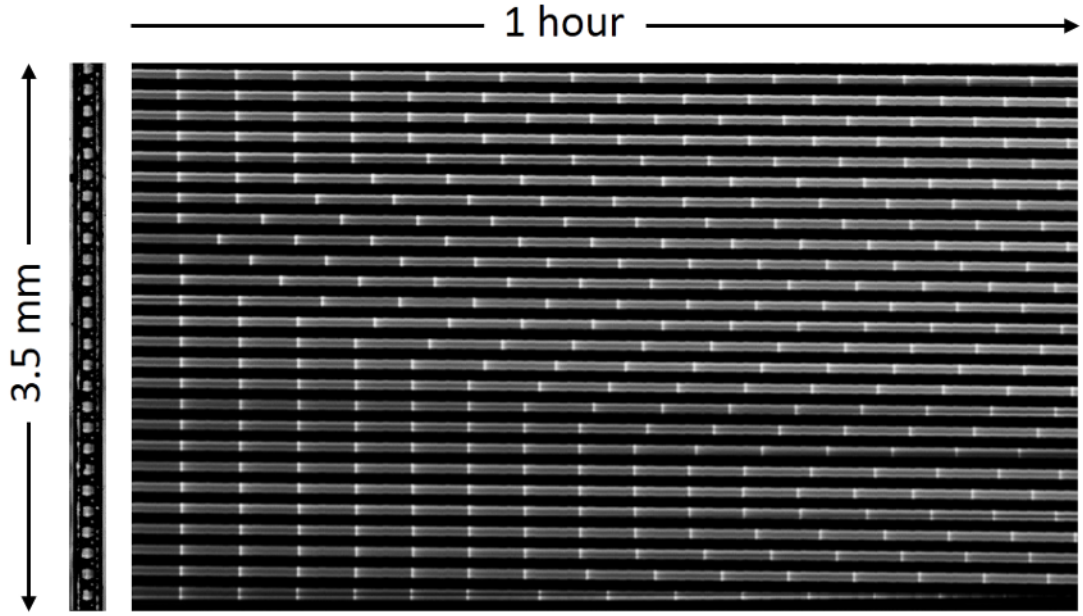

Figure 2.3: An example image of a capillary of close packed BZ droplets and its space-time plot.

2.2 Computational Methods

2.2.1 Chemical Mechanism of Oscillation

FKN mechanism

Field, Körös and Noyes presented a series of fundamental works in the 70's demonstrating a detailed mechanism of the BZ oscillation[30, 31, 32], later known as the FKN mechanism. All of our simulations are essentially based on this mechanism, sometimes with minor variances[33, 34]. We will briefly introduce the FKN mechanism here.

We can treat the complete BZ cycle as the result of three processes. In process A, there is sufficient bromide ion in an acid solution of bromate and malonic acid. The sequence (2.1) + (2.2) + 3(2.3) + 3(2.4) results in net process A (2.5).

Process A:

$$BrO_3^- + Br^- + 2H^+ \xrightarrow{k_2} HBrO_2 + HOBr \tag{2.1}$$

$$HBrO_2 + Br^- + H^+ \xrightarrow{k_1} 2HOBr \tag{2.2}$$

$$HOBr + Br^- + H^+ \underset{k_6}{\overset{k_5}{\rightleftharpoons}} Br_2 + H_2O \tag{2.3}$$

$$Br_2 + CH_2(COOH)_2 \xrightarrow{k_7} BrCH(COOH)_2 + Br^- + H^+ \tag{2.4}$$

Net process A:

$$BrO_3^- + 2Br^- + 3CH_2(COOH)_2 + 3H^+ \rightarrow 3BrCH(COOH)_2 + 3H_2O \tag{2.5}$$

When bromide ion is virtually absent, bromate ion reacts with the catalyst (Ce(III) in the original paper[30], Fe(II) in our case) and malonic acid. The sequence 2(2.6) + 4(2.7) + (2.8) + (2.9) results in the net process B (2.10). And the sequence (2.6) + 2(2.7) leads to autocatalytic production of $HBrO_2$.

Process B:

$$BrO_3^- + HBrO_2 + H^+ \underset{k_r}{\overset{k_4}{\rightleftharpoons}} 2BrO_2\cdot + H_2O \tag{2.6}$$

$$BrO_2\cdot + Fe(phen)_3^{2+} + H^+ \xrightarrow{k_{red}} HBrO_2 + Fe(phen)_3^{3+} \tag{2.7}$$

$$2HBrO_2 \xrightarrow{k_3} BrO_3^- + HOBr + H^+ \tag{2.8}$$

$$HOBr + CH_2(COOH)_2 \xrightarrow{k_8} BrCH(COOH)_2 + H_2O \tag{2.9}$$

Net process B:

$$\begin{aligned}\mathrm{BrO_3^-} + 4\mathrm{Fe(phen)_3^{2+}} + \mathrm{CH_2(COOH)_2} + 5\mathrm{H^+} \rightarrow \\ \mathrm{BrCH(COOH)_2} + 4\mathrm{Fe(phen)_3^{3+}} + 3\mathrm{H_2O}\end{aligned} \tag{2.10}$$

The irreversible processes A and B will take place under different conditions in the same system and a solution reacting by process A will eventually convert itself to one reacting by process B. To have oscillation, however, we need to get back from B to A. This is accomplished by Fe(III) produced in process B reacting with the organic species by overall processes (2.11) and, more importantly (2.12). When the rate of (2.12) becomes sufficiently great, process B is "turned off" and process A is re-initiated, so that the oscillatory cycle and begin again. The net process C is the result of the sequence $x(2.5) + (3-x)(2.10) + (2-2x)(2.11) + 2x(2.12)$ where $x \in [0,1]$.

Process C:

$$\begin{aligned}6\mathrm{Fe(phen)_3^{3+}} + \mathrm{CH_2(COOH)_2} + 2\mathrm{H_2O} \xrightarrow{k_{10}} \\ 6\mathrm{Fe(phen)_3^{2+}} + \mathrm{HCOOH} + 2\mathrm{CO_2} + 6\mathrm{H^+}\end{aligned} \tag{2.11}$$

$$\begin{aligned}4\mathrm{Fe(phen)_3^{3+}} + \mathrm{BrCH(COOH)_2} + 2\mathrm{H_2O} \xrightarrow{k_9} \\ \mathrm{Br^-} + 4\mathrm{Fe(phen)_3^{2+}} + \mathrm{HCOOH} + 2\mathrm{CO_2} + 5\mathrm{H^+}\end{aligned} \tag{2.12}$$

Net process C:

$$\begin{aligned}3\mathrm{BrO_3^-} + 5\mathrm{CH_2(COOH)_2} + 3\mathrm{H^+} \rightarrow \\ 3\mathrm{BrCH(COOH)_2} + 2\mathrm{HCOOH} + 4\mathrm{CO_2} + 5\mathrm{H_2O}\end{aligned} \tag{2.13}$$

Reactions with Light

To have light control of BZ oscillation we need to use $\mathrm{Ru(bipy)_3}$. In principle we can use $\mathrm{Ru(bipy)_3}$ only. However, to have better contrast in the space time plot, we also use ferroin

as previously mentioned in the default condition which is using 3 mM ferroin and 0.4 mM $Ru(bipy)_3$. The photosensitive reactions involving Ru(II) complex (i.e. $Ru(bipy)_3^{2+}$) are listed here[33].

$$Ru(bipy)_3^{2+} + h\nu \xrightarrow{k_I} Ru(bipy)_3^{2+}* \tag{2.14}$$

$$Ru(bipy)_3^{2+}* + BrCH(COOH)_2 + H^+ \xrightarrow{k_C} Ru(bipy)_3^{3+} + Br^- + \text{products} \tag{2.15}$$

$$Ru(bipy)_3^{2+}* \xrightarrow{k_d} Ru(bipy)_3^{2+} \tag{2.16}$$

Differential Equations for Reaction

I summarized the constant and variable chemical species and the reaction rates for the full FKN model in the following table 2.1. With the variables and constants defined in this table, we have the set of ordinary differential Eqs. 2.17 to 2.23 derived from reactions 2.1 to 2.16.

For light control reactions, $k_I = 10^{-3} \sim 10^{-4}$ s^{-1}, $b_C = k_d/k_C = 0.05$ M. While we use two catalysts $Fe(phen)_3$ and $Ru(bipy)_3$ in our experiments, in simulation we disregard this distinction and consider only one photosensitive catalyst represented by c/z in its reduced/oxidized form.

concentration	**constant**	**reaction rate**	**value**
$[H^+]$	h	k_1	2×10^6 $[M^{-2}s^{-1}]h$
$[BrO_3^-]$	A	k_2	2 $[M^{-3}s^{-1}]h^2A$
$[CH_2(COOH)_2]$	m	k_3	3000 $[M^{-1}s^{-1}]$
$[BrCH(COOH)_2]$	$B(=0.1m)$	k_4	42 $[M^{-2}s^{-1}]hA$
concentration	**variable**	k_5	5×10^9 $[M^{-2}s^{-1}]h$
$[HBrO_2]$	x	k_6	10 $[s^{-1}]$
$[Br^-]$	y	k_7	29 $[M^{-1}s^{-1}]m$
$[HOBr]$	p	k_8	9.3 $[M^{-1}s^{-1}]m$
$[BrO_2\cdot]_{BZ}$ / $[BrO_2\cdot]_{Oil}$	w / r	k_9	$0.07 \sim 0.12$ $[M^{-1}s^{-1}]m$
$[Br_2]_{BZ}$ / $[Br_2]_{Oil}$	u / s	k_{10}	0.05 $[M^{-1}s^{-1}]m$
$[Fe(phen)_3^{2+}]$	c	k_r	2×10^8 $[M^{-1}s^{-1}]$
$[Fe(phen)_3^{3+}]$	z	k_{red}	5×10^6 $[M^{-1}s^{-1}]$

Table 2.1: Summary of chemical concentrations and reaction rates.

$$\frac{dx}{dt} = -k_1xy + k_2y - 2k_3x^2 - k_4x + k_rw^2 + k_{red}wc \tag{2.17}$$

$$\frac{dy}{dt} = -k_1xy - k_2y - k_5yp + k_6u + k_7u + k_9z + \frac{k_Ic_IB}{b_C + B} \tag{2.18}$$

$$\frac{dz}{dt} = k_{red}wc - k_9z - k_{10}z + \frac{k_Ic_IB}{b_C + B} \tag{2.19}$$

$$\frac{dp}{dt} = 2k_1xy + k_2y + k_3x^2 - k_5yp + k_6u - k_8p \tag{2.20}$$

$$\frac{du}{dt} = k_5yp - k_6u - k_7u \tag{2.21}$$

$$\frac{dw}{dt} = 2k_4x - 2k_rw^2 - k_{red}wc \tag{2.22}$$

$$\frac{dc}{dt} = -k_{red}wc + k_9z + k_{10}z - \frac{k_Ic_IB}{b_C + B} \tag{2.23}$$

2.2.2 Point Oscillator Model

Now that we have a understanding about the reaction, let us have a look at diffusion. Fig. 2.4 draws a simple vision of bromine diffusion through the oil gap between two BZ drops oscillating alternatively. The figure is showing the moment that left drop is at the oxidized status of the redox (R/O) cycle, releasing bromine, which is a product of BZ oscillation, to the right drop, and therefore suppressing the right drop to reduced state. The right drop later on will do the same to the left, so that the two drops are coupled by bromine inhibition, naturally leading to a 180° anti-phase oscillation. The red/blue color represent the reduced/oxidized state of ferroin. The concentration profile [Fe(III)] as a function of time for both of the drops is shown at the lower half of the figure. Dashed line and solid line are used to distinguish the two drops.

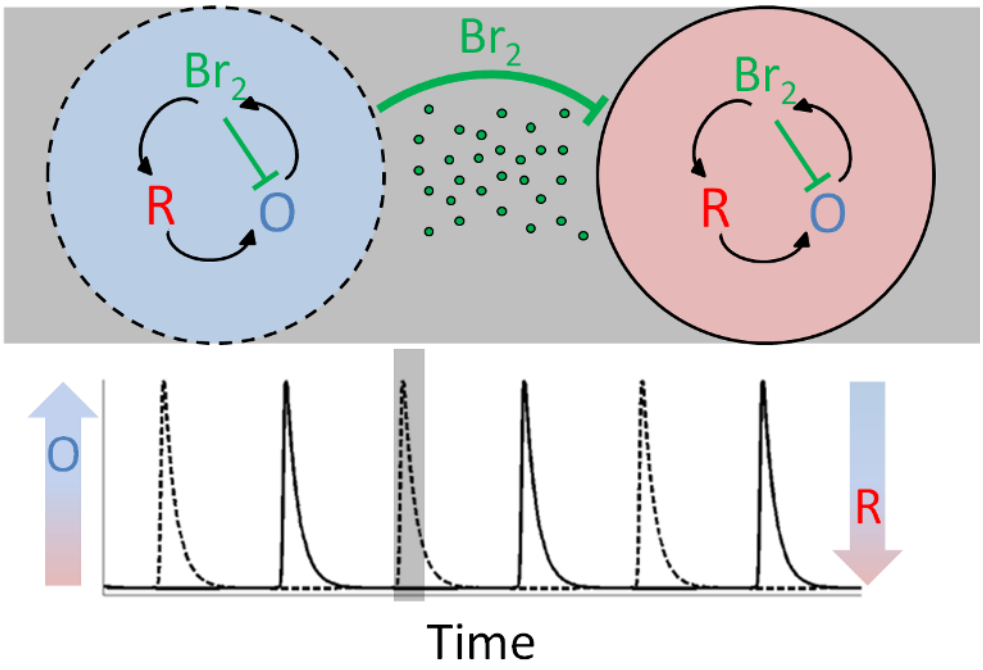

Figure 2.4: Schematic drawing of two BZ droplets diffusively coupled to each other. Adapted from previous work[10].

To quantitatively model the diffusion, we established a point model as shown in Fig. 2.5.

There are four subfigures here arranged in the same order of simplifying the geometry and building the point model: a) The camera image of a small portion of a capillary where we can see two BZ droplets (~ 200 μm wide) separated by a oil gap (~ 80 μm wide). b) Ignoring the curvature of water/oil interphase, we simplify the experimental scenario to a 2D box of oil containing two BZ rectangles, BZ_1 and BZ_2. We define the maximum width of the BZ droplet (i.e. the width at the center) to be the width of BZ_1 and BZ_2, namely a; and the center width of the oil gap to be b. Box BZ_1 and BZ_2 are assumed to have the same width a, which is based on the fact the microfluidic generated droplets are highly identical - the diameters varied by less than 2%. For this rectangular geometry the height of BZ and oil cells (which is the same) is somewhat irrelevant as the variances only happen along the capillary. Therefore this 2D rectangular model is essentially a 1D model. c) Assuming the bromine concentrations in BZ_1, BZ_2 and the oil in between are spatially linear, as demonstrated by the solid red lines. Partition coefficient is the ratio of concentrations of a chemical in a mixture of two immiscible phases at equilibrium. The partition coefficient of bromine at BZ/oil interphase, $[Br_2]_{oil}{}^*/[Br_2]_{BZ}{}^*$, is about 2. So at equilibrium, $[Br_2]$ at the right boundary of BZ_1 is about half of that at the left boundary of oil. Similarly $[Br_2]$ at the right boundary of oil is twice of that at the left boundary of BZ_2. However, we want to simplify this model even more, that is to assume the concentration in each cell is uniform, as the dashed red lines. On one hand, this further simplification is justified by the fact that the droplets are very small so that gradient within a drop can be ignored. On the other hand, a uniform concentration in oil cannot satisfy the boundary partition coefficient on both sides of oil simultaneously when $[Br_2]$ in BZ_1 is different from that in BZ_2. We will see in the next chapter that despite these flaws and approximations, this model works fairly well comparing to experimental results. d) Now that $[Br_2]$ in each cell can be represented by its center concentration, we can think of the cells as points at the center with the same concentration. Diffusive fluxes J_1 from BZ_1 to oil, J_2 from oil to BZ_2 are caused by the concentration gradient from point to point, yet

the points are separated by the center-to-center distance, $(a+b)/2$.

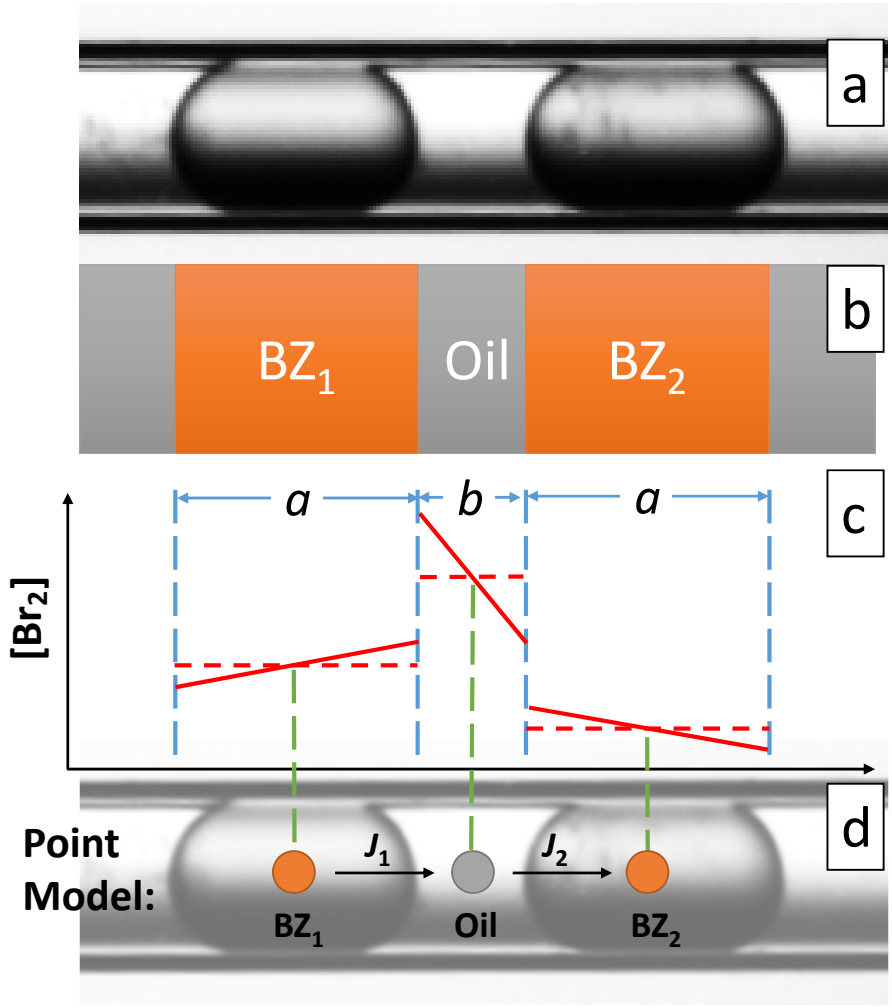

Figure 2.5: Illustration for point model

The mathematical form we derived for the point model is based on Fick's law of diffusion and mass conservation. The bromine flux between oil and BZ drop according to Fick's first law is as follows:

$$\begin{aligned} J &= -D\frac{\partial u}{\partial x} \\ &\approx -D\frac{\Delta u}{\Delta x} \\ &= D\left[\frac{s-uP_{\mathrm{U}}}{(a+b)/2}\right] \end{aligned} \tag{2.24}$$

where D is the diffusion coefficient of bromine molecule, P_{U} is partition coefficient of bromine. We assume the diffusion coefficient is the same for all species in oil and water. Flux by definition can also be written as:

$$\begin{aligned} J &= \frac{\Delta N}{\Delta t A} \\ &= \frac{\Delta u V_{\mathrm{drop}}}{\Delta t A} \\ &= \frac{\Delta u a}{\Delta t} \end{aligned} \tag{2.25}$$

where V_{drop} is the volume of a BZ droplet which equals the cross section area of the capillary A times the width of the drop a. With Eqs. 2.24 and 2.25, we have:

$$\frac{\Delta u}{\Delta t} = \frac{J}{a} = 2D\left[\frac{s - uP_{\mathrm{U}}}{a(a+b)}\right] \tag{2.26}$$

Finally we can combine reaction and diffusion together and solve the full dynamics of the system. To do so, we only need to add the diffusion parts into the Eqs. 2.17 to 2.23 where diffusion through oil phase is allowed. For example, there will not be any change of Eq. 2.18 as bromide ion cannot diffuse into oil phase, in other words, $P_{\mathrm{Y}} = 0$. For species that is non-polar or weakly polar, such as bromine, we have the reaction diffusion equation as:

$$\frac{du_n}{dt} = k_5 y_n p_n - k_6 u_n - k_7 u_n + 2D\left[\frac{s_{n-1} + s_n - 2P_{\mathrm{U}} u_n}{a(a+b)}\right] \tag{2.27}$$

$$\frac{ds_n}{dt} = 2D\left[\frac{P_{\mathrm{U}}(u_n + u_{n+1}) - 2s_n}{b(a+b)}\right] \tag{2.28}$$

where the subscript n is the drop index and s_n is the bromine concentration in the oil gap right to the BZ drop where u_n is defined. The partition coefficient of bromine, $P_{\mathrm{U}} = 2.5$, is a precisely measured value. However, bromine is not the only species can diffuse through oil. Bromous acid $HBrO_2$ and radical $BrO_2\cdot$ are also expected to diffuse into oil phase, with

estimated partition coefficients $P_{\mathrm{X}} = 0.05 \sim 0.1$ and $P_{\mathrm{W}} \approx 1$. There is even experimental evidence suggesting that malonic acid can also diffuse into oil, which is not accounted for in our current model. We will talk about more about this in the following chapter.

The actual ODE solver we use for the point model is "ode15s" in MATLAB® (version R2011a). ode15s is a variable-order solver for stiff problems with low to medium accuracy (best available). For solver error control, we set the relative tolerance $RelTol = 1e-8$ and the absolute tolerance $AbsTol = 1e-9$ for most cases. The time step is set to be 1 second for ode15s for most cases.

We also developed another version of point model without defining the oil segments between drops explicitly, which ignores the chemical accumulation in oil. Using the same Fick's law derivations we have the expression,

$$\frac{du_n}{dt} = k_5 y_n p_n - k_6 u_n - k_7 u_n + 2DP_{\mathrm{U}} \left[\frac{u_{n-1} + u_{n+1} - 2u_n}{ab} \right]. \tag{2.29}$$

This alternative expression of flux, with the addition of the Derjaguin approximation considering the actual curvature of the drops[15], is only used in the point model simulations in Chapter 4.

2.2.3 Finite Element Analysis

Although the point model works well for 1D system, the disadvantage of the uniform concentration approximation becomes more obvious in 2D system where droplets are close packed in a hexagonal lattice. Even in 1D, we need to examine how good the approximation is, not only comparing to experimental results, but also to more accurate numerical simulations. The diffusion part of our system, without approximation, should be in the form of Fick's

second law,

$$\begin{cases} \dfrac{\partial u}{\partial t} = D\dfrac{\partial^2 u}{\partial x^2} & \text{1D} \\ \dfrac{\partial u}{\partial t} = D\nabla^2 u & \text{2D or more} \end{cases} \tag{2.30}$$

We can see that the assumption of uniform concentration (treating each drop as one point) cannot give us a satisfactory solution to the second order PDE 2.30. We need to at least segment each cell to 3 pieces; and the more pieces we segment each cell, the more precise spatial concentration solution we can get. It is analogous to the idea that connecting many tiny straight lines can approximate a large circle, the shorter the straight lines are, the smoother the circle is. This leads to the finite element method (FEM). An example of FEM simulated result of two BZ droplets in a 2D oil box created in software COMSOL multiphysics® is shown in Fig. 2.6. The basic geometry is a 2D rectangle containing two circles, representing one oil box containing two BZ droplets ($a = 200\ \mu m, b = 20\ \mu m$). This geometry is meshed into many small triangles and at each node of the mesh the spatial derivatives from the PDE are eliminated (automatically in COMSOL), thus approximating the PDE locally with a set of ODEs for transient problems such as ours. The bromine profile for the whole geometry at this moment is shown in rainbow color, where red is high [Br_2] and blue is low [Br_2]. This is the same moment as in Fig. 2.4 and with COMSOL we can quantitatively visualize the bromine flux (black arrows) from one drop to the other. If we extract this profile through the two centers of BZ drops and plot the [Br_2] profile of the two drops and oil gap in between, as shown in solid blue curves in the lower half plot, we can see that our previous assumption of uniform or linear concentration is, as we expected, not very good. But the high accuracy spatial profile of FEM comes with a price, that is computational efforts. So most of our 1D simulation were studied in the point model, which allowed us efficiently increase the number of trials and the number of droplets for better

statistics.

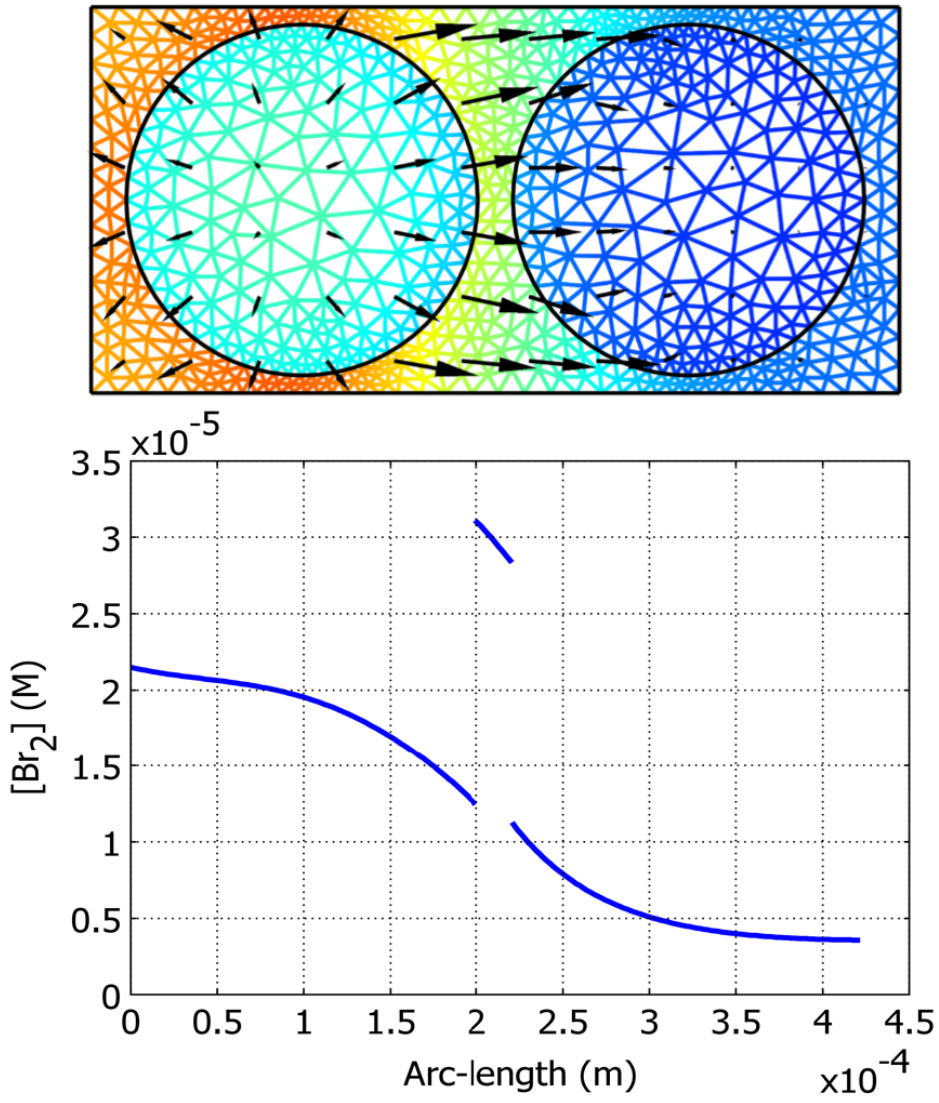

Figure 2.6: Example of FEM modeling

2.2.4 Phase Model

We would like to further simplify the seven-variable FKN mechanism. There has been simplifications such as Oregonator[32] and Vanag-Epstein model[34] that reduce the number of variable chemical species down to three or four. But can we reduce it down to only one

variable? To answer this question, let us first look at the reaction diffusion Eq. 2.31 for an unstirred beaker of BZ mixture solution.

$$\dot{\boldsymbol{X}} = \boldsymbol{F}(\boldsymbol{X}) + \boldsymbol{D}\nabla^2\boldsymbol{X}, \tag{2.31}$$

where $\boldsymbol{X}$ is a vector containing the seven variable chemical concentrations x, y, z, etc., $\boldsymbol{F}$ is a vector function describing the chemical kinetics of each species, and $\boldsymbol{D}$ is a matrix of diffusion constants. This equation can also be applied to one BZ microdroplet. If we have two BZ droplets diffusively coupled to each other, then reaction diffusion equation of the two drop system becomes Eq. 2.32.

$$\begin{cases} \dot{\boldsymbol{X}}_1 = \boldsymbol{F}(\boldsymbol{X}_1) + \boldsymbol{M}(\boldsymbol{X}_2 - \boldsymbol{X}_1) \\ \dot{\boldsymbol{X}}_2 = \boldsymbol{F}(\boldsymbol{X}_2) + \boldsymbol{M}(\boldsymbol{X}_1 - \boldsymbol{X}_2) \end{cases} \tag{2.32}$$

Here $\boldsymbol{M}$ is a diagonal matrix containing the constants of diffusive transport of each species from drop to drop, while the diffusion inside each drop is ignored due to the nL scale volume. It is assumed that the oscillators, if uncoupled, are the same in nature ($\boldsymbol{F}$). If the drops are weakly coupled, which requires the diffusion terms are small compared to the reaction terms in Eq. 2.32, we can then simplify the cycle in 7-dimensional chemical space to a 1D phase space.

Fig. 2.7 illustrates how is phase defined in our system. We pick the moment when z reaches maximum as the beginning of phase, $\theta = 0$. This is convenient because it is also the moment that the drop becomes oxidized and gives highest brightness in the space time plot. The concentration profiles of x, y, and z as a function of time in Fig. 2.7 start from $\theta = 0$; at this moment z reaches its maximum, x has just pasted its maximum and y is going to its maximum. After one period T, z reaches its maximum again, x and y also come back to the same status one period ago, and now $\theta = 1$. Similarly after another period, $\theta = 2$, and so on. In other words, phase is linearly defined in time. We use unit 1 for phase, which is

equivalent as using 2π.

To visualize the mapping between chemical space and phase space, we plotted the limit cycle (closed trajectory) in x-z plane in Fig. 2.8 (blue curve with circle marker). The circle markers are evenly spaced in time (i.e., phase) by 0.1 second. The markers are more closely spaced at low x than at high x, which means the BZ drop spends most of a period at low x. We can also see this in the time profile of x in Fig. 2.7, that only a small fraction in one period x is high, while during most of the period x is almost zero. The actual limit cycle for the 7-variable FKN model is a loop in 7-D chemical space, but we can only visualize two or three at best. By mapping this complicated oscillation trajectory in 7-D chemical space onto a simple 1D phase space, we have a great advantage of simplicity and more importantly, universality, which allows us to apply what we learnt from BZ oscillators to more complicated biological oscillators such as neurons.

Yoshiki Kuramoto proposed a mathematical model in the 70's to describe synchronization of coupled oscillators[35, 36]. The most popular form of the model is Eq. 2.33:

$$\frac{d\theta_i}{dt} = \omega_i + \frac{K}{N}\sum_{j=1}^{n}\sin(\theta_j - \theta_i) \tag{2.33}$$

where θ is the phase of each limit cycle oscillator, ω is the natural frequency of each oscillator, N is the number of oscillators, and K is the coupling constant. This model makes three assumptions about the oscillators and the coupling: 1) all-to-all, weak coupling; 2) nearly identical oscillators; 3) interactions that depend sinusoidally on the phase difference between two oscillators. There has been study[37] that modifies Kuramoto's model to local coupling, successfully explaining the qualitative behaviors of entrainment and synchronization in BZ droplets. However, if we want better quantitative understanding, a more specific coupling function is needed to replace the sinusoidal function in Kuramoto's phase model. We define our coupling function H as illustrated in Fig. 2.9.

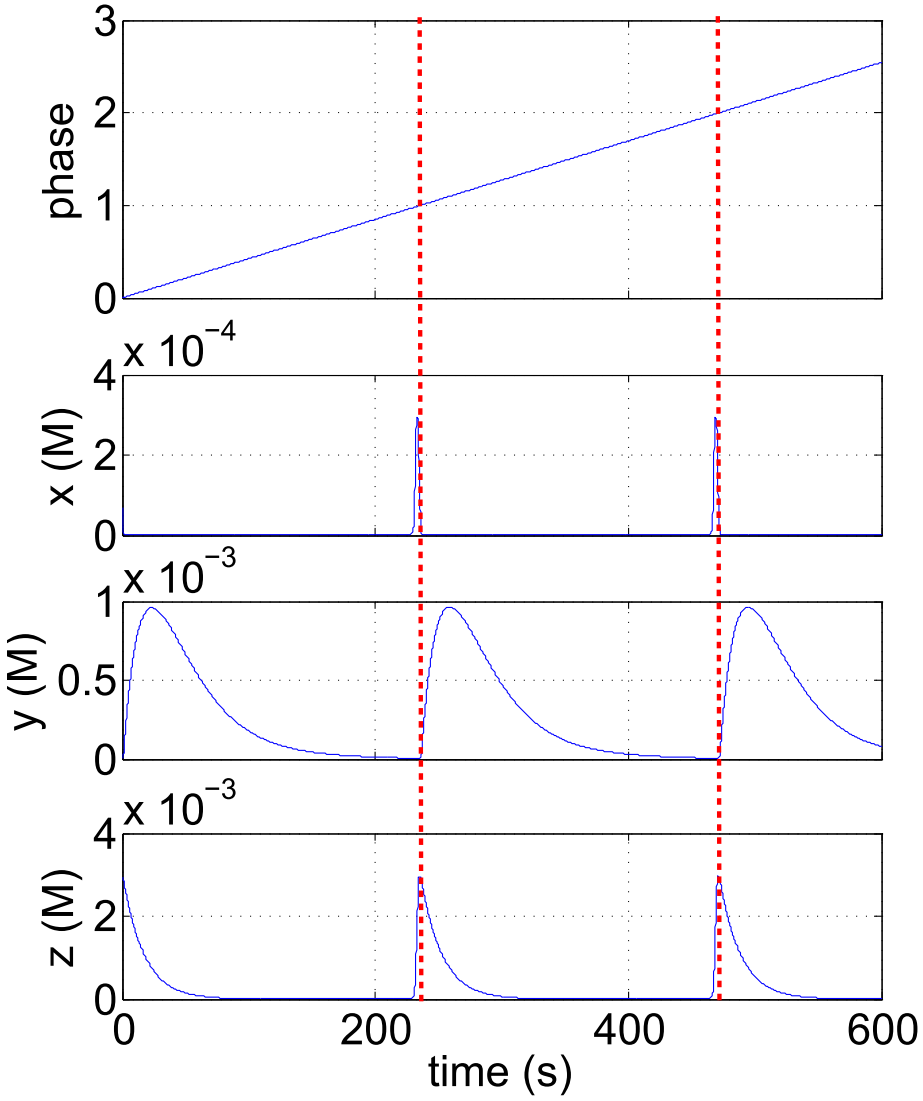

Figure 2.7: Definition of phase. Concentration profiles are from one of the two coupled BZ droplets simulated with 7-variable FKN model in point oscillator method, but only x, y, z are shown here.

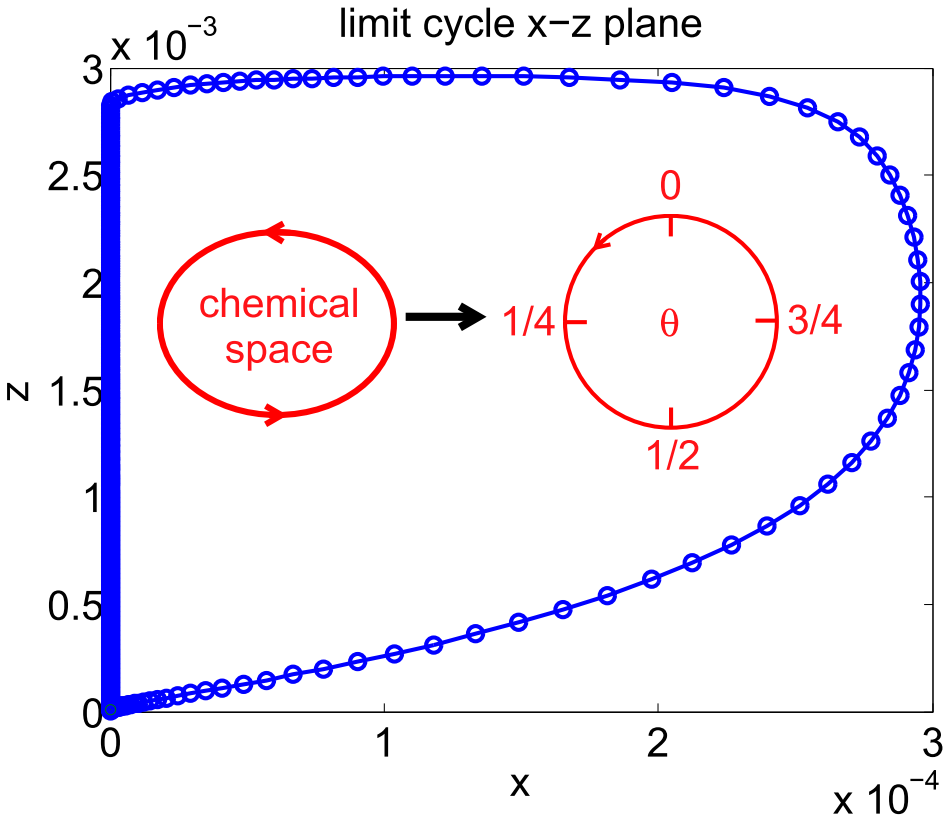

Figure 2.8: Limit cycle in x-z plane

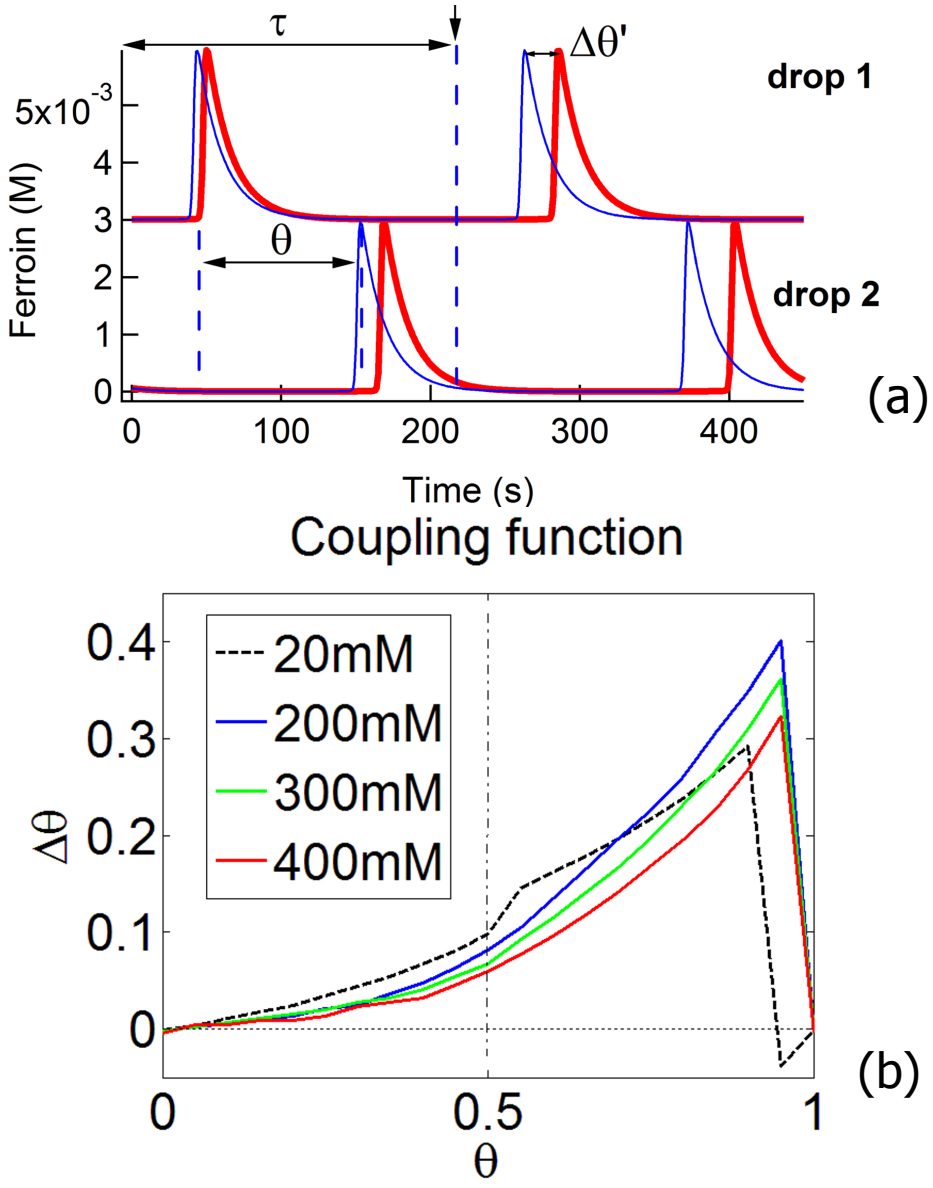

Figure 2.9: H coupling function

We will revisit this subject in section 3.2.2 of the next chapter and discuss in detail about phase response curve and H function.

Chapter 3

One-Dimensional Chemical Oscillators

The whole problem with the world is that fools and fanatics are always so certain of themselves, but wiser people so full of doubts.

Bertrand Russell

Active matter refers to materials composed of self-propelled agents which continuously consume energy to generate collective motion[38, 39, 40]. The field of active matter is young and dominated by theory; lack of model experimental systems that can easily be reproduced and studied by many groups has hampered progress. Developing robust experimental active matter systems is challenging because of the tendency for irreversible processes to degrade the active agents and prevent them from functioning. Biological active matter (e.g., flocks, cytoskeleton) works reliably in vivo because of extensive repair mechanisms, which have not been replicated in vitro. We present here the first steps towards development of a chemically based active matter experimental system, active emulsions. Collective motion requires two attributes from the active agents: communication and motion. Here we focus solely on the development of communication in active emulsions, leaving the challenge of self-propulsion

for the future.

Synchronization of a large number of elementary units plays a key role in the functioning of many complex biological and social systems. Examples include quorum sensing in bacteria[41], ciliary fields[42, 43], cardiac muscle contraction[44], neural activity and insect behavior[45]. Driven entrainment has often been used to induce and to modulate synchronization dynamics[46, 47, 48]. As an example of coupled non-linear chemical oscillators, the Belouzov-Zhabotinsky (BZ) reaction, the metal-ion-catalyzed oscillatory oxidation of an organic substrate, most commonly malonic acid (MA), by bromate, has become the prototype of nonlinear dynamics in chemistry and a preferred system for exploring the dynamics of coupled nonlinear oscillators[7]. Micron-sized beads have been employed as BZ reactors, and several strategies have been devised to achieve coupling between these oscillators[49, 50, 51]. In these examples, coupling among the oscillators occurs via all chemical species; here we restrict the subset of coupling species, in order to promote inhibitory coupling. A problem of particular interest is to determine the attractor(s), i.e., the stable dynamical state(s) to which a system of interacting oscillators spontaneously evolves.

Here we study a linear array of discrete, coupled, nonlinear chemical oscillators composed of emulsions of aqueous BZ droplets in oil stored in a capillary in order to form a one-dimensional (1D) array. As demonstrated previously[19, 9], a small subset of the BZ chemicals, an inhibitory component, bromine (Br_2), and an excitatory component, bromine dioxide radical ($BrO_2\cdot$), diffuse from drop to drop through the intervening oil, thereby producing a chemical coupling between drops. Bromine brominates malonic acid, generating bromide and thereby inhibiting the excitatory coupling and preventing the oxidation of the catalyst [52, 30, 31]. Since bromine is the principal chemical diffusing between BZ drops, inhibitory coupling dominates. Bromine is produced in a short interval of time during each cycle of the oxidation transition, so each BZ drop that has just undergone an oxidation transition emits a pulse of Br_2 that acts to delay the transition of its neighboring drops

resulting in the out-of-phase response. Since the system is closed, so that the BZ reactants are not replenished, after at most 100 oscillations enough of the reagents are consumed so that oscillations cease as the final equilibrium state is approached.

With the techniques introduced in chapter 2, we present the detailed results for 1D BZ oscillators in this chapter, consisting of three following sections: 1) the experimental results, compared with numerical simulations; 2) several methods we used to measure the coupling strength between BZ oscillators; 3) testing Turing mechanism with our BZ drops.

3.1 Experiments and Simulations

In most of our studies of BZ oscillators, we focus on the most important few parameters as the tunable experimental conditions. These parameters are drop size a, defined as the longitudinal distance between the two ends of the drop in the cylindrical capillary; oil gap size b, defined as the distance between the closest ends of two drops; and malonic acid concentration m, carefully chosen based on previous experience[19]. Tuning these parameters will change the strength of the diffusive coupling between drops: increasing m or increasing a or b will weaken the coupling strength. In previous studies [19], the anti-phase attractor was reported to be the most common pattern for emulsions of BZ droplets in oil in a 1D configuration under conditions ($m \geq 100$ mM) dominated by inhibitory coupling due to the diffusion of the inhibitory species Br_2 through the oil. This conclusion was based on the experimental observation that addition of a bromine scavenger eliminated coupling effects and the fact that the theoretical results were almost identical with and without inclusion of the diffusive coupling of the excitatory species $BrO_2\cdot$ and $HBrO_2$ for $m \geq 100$ mM. In contrast, at low m (< 100 mM), the results indicate the increasing importance of excitatory coupling. We will first present the results for weakly coupled ($m \geq 100$ mM) oscillators, then the stronger coupled ones ($m < 100$ mM).

3.1.1 Weakly Coupled BZ Droplets

Using the "default condition" recipe defined in Chapter 2, we obtain out-of-phase inhibitory patterns using monodispersed droplets with a ranging between 100 and 220 μm while the droplets are uniformly spaced, with b ranging from near-contact to 130 μm. In this section we present experiments on 1D arrays of droplets interacting along the axes of hydrophobized capillaries with a 100 μm inner diameter. In each array of droplets, approximately 100 droplets at most can be imaged simultaneously, and beyond the field of vision there are at least 15 more droplets on each side from the sealed end of the capillary. We will describe the typical behavior of these systems for several different m values. An example experimental result is shown in Fig. 3.1. The droplets in fields of view were suppressed and synchronized for $3 \sim 4$ minutes (approximately one oscillation period) with blue light from a projector as described in Chapter 2 and then allowed to oscillate freely without any light perturbation.

To emphasize the characteristics of this typical out of phase behavior of weakly coupled BZ droplets, a segment of a capillary with $m = 640$ mM droplets array is shown in Fig. 3.2a and the binarized, color-reversed space-time plot of this system shown in Fig. 3.2b. Light synchronization set all the drops in-phase in the reduced state of ferroin at the beginning of the experiment. Most drops' first transition from the reduced to the oxidized state were in phase, displayed as the first black line in Fig. 3.2b. Our numerical simulations reveal that during the short oxidized portion of the oscillation the Br_2 concentration in each drop is high. At this moment in the oscillation cycle the drop is less susceptible to having its phase shifted by the addition of Br_2 diffusively transferred from a neighboring drop than at a later time in the drop's cycle. With time, the Br_2 is removed through bromination of malonic acid after which the oxidation transition can reoccur. Notice in Fig. 3.2b that a few drops transition with a delay. Focus on the isolated delayed drop in the middle of the space-time plot in Fig. 3.2b, which emits Br_2 during the oxidation transition. If this transition is sufficiently delayed, then it occurs when $[Br_2]$ in the neighboring drops has

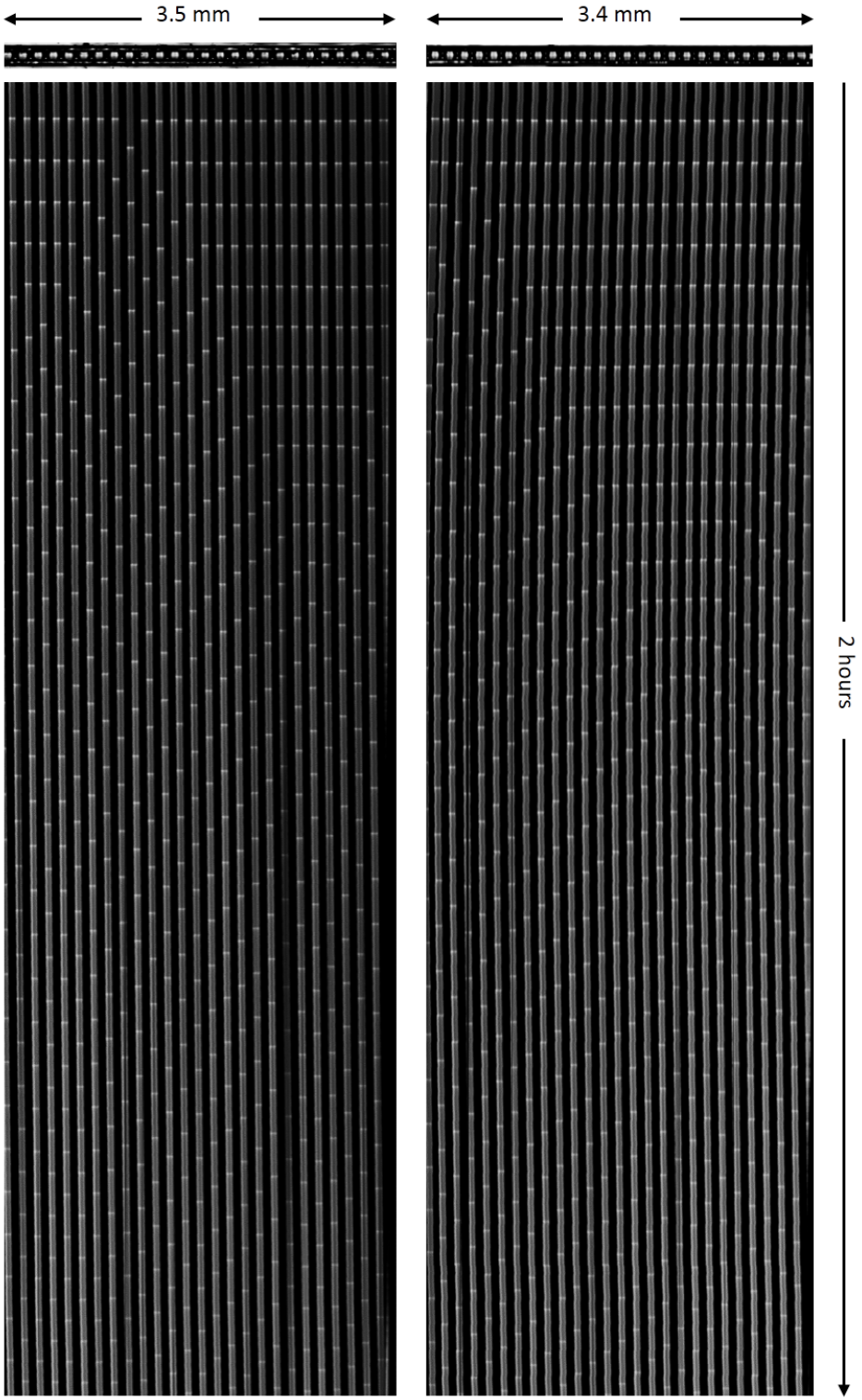

Figure 3.1: Typical 1D pattern without light boundary.

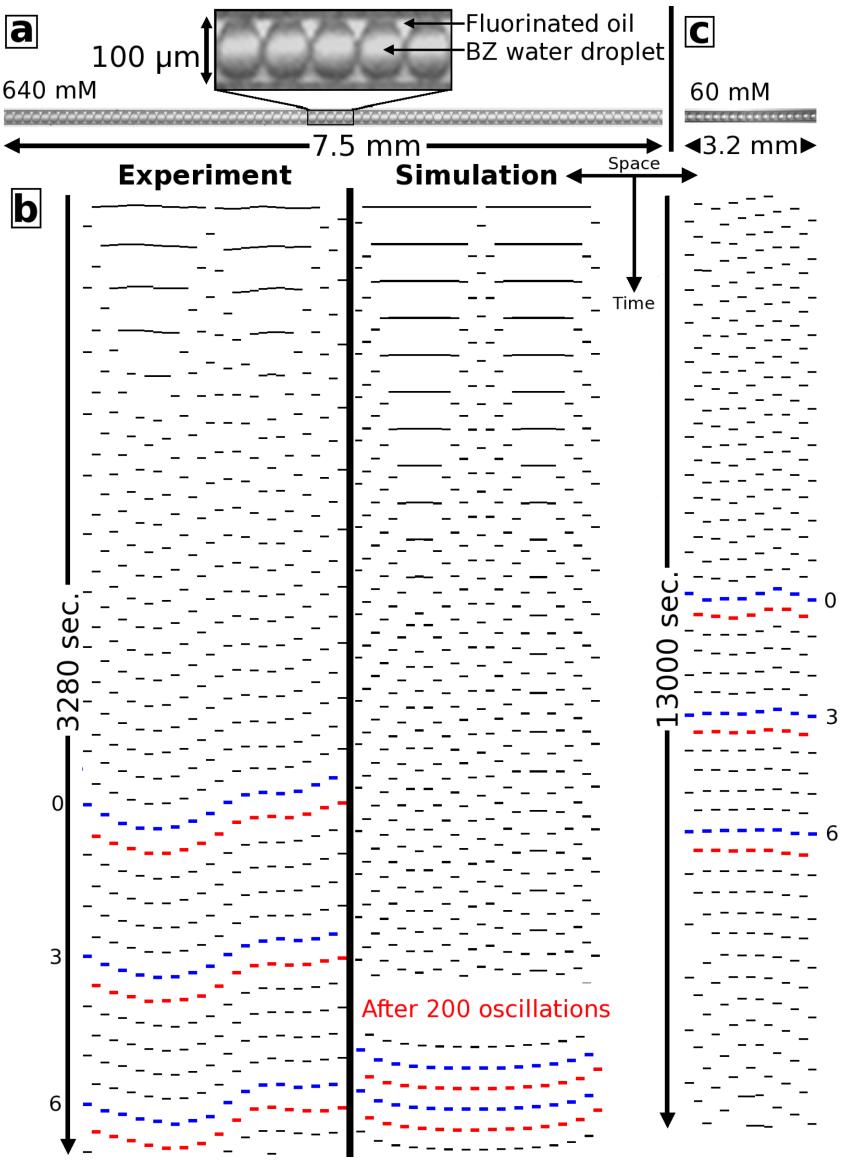

Figure 3.2: 1D pattern, experiment vs. simulation with binarized space-time plots. (a) Upper photograph shows detail of BZ droplets in a 100 μm diameter capillary. Lower photograph shows a section of a capillary containing 75 BZ droplets. (b) Experiment: binarized, intensity-inverted, spacetime plot of BZ oscillations of droplets at [MA] = 0.64 M. Space is horizontal; time flows vertically from top to bottom. Each black bar corresponds to the oxidized state of a single drop; white regions correspond to the reduced state. At t = 0 (not shown), all droplets are synchronized in the reduced state using external light forcing. An arbitrary reference oscillation is labeled "0" with every odd-indexed drop colored blue and every even-indexed drop colored red. Simulation: spacetime plot of a simulation of 30 BZ drops separated by oil. Initial conditions are the same as in experiment (c) Binarized, intensity-inverted, spacetime plot of BZ oscillations of 15 droplets at [MA] = 0.060 M in the middle of a large sample. Image of the capillary containing the droplets from which the spacetime plot is obtained is presented at the top. Adapted from previous work[10].

reached a relatively low value, and these drops will receive a sufficient dose of Br_2 from the emitter to delay their next oxidation transition, which leads to longer periods for droplets out of phase. In turn, these new delayed drops influence their in-phase neighbors, and the number of in-phase drops decreases monotonically.

In Fig. 3.2b the time of an arbitrary oxidation transition on the left side of the space-time plot is labeled "0". We pick the leftmost drop and color in blue the oxidation transition that occurs at time "0". Then we label in blue the oxidized state of its second nearest neighbor that is closest in time to its oxidation transition and in this manner continue painting transitions of every other drop blue until we reach the right hand side of the space-time plot. In this way we construct a "wave front" of the oxidized state. We color in red the transition of drop that is second from the left that is closest in time to the first blue drop and continue proceeding from left to right until each second nearest neighbor drop is labeled red. If the drops were in an attractor where every other drop had a phase difference of π (half a cycle) with its two nearest neighbors, then the blue and red wave fronts would be straight and separated in time by exactly half a period.

Fig. 3.2b also shows a simulation of a capillary containing 30 drops with $m = 640$ mM. In the simulation, calculated using a modified version of a previously used extension of the FKN model[33], with $a = 200$ μm with a vanishing oil gap ($b = 10^{-4}$ μm), to model the experimental case of drops in contact. The outermost drop at each end is modeled to be held at constant illumination, which prevents those drops from oscillating, effectively forming constant concentration boundary conditions. Only the remaining 28 drops, which are not illuminated and therefore can oscillate, are shown in the space-time plot. The simulations are done on "open" systems in which the principal chemical reagents that feed the BZ reaction are held constant (see appendix for details), so the reaction can oscillate forever. Initially, three drops, the nearest neighbor to each boundary drop and one drop in the middle of the system are set 180° out of phase with all the other drops. With each transition, the out-

of-phase drops cause neighboring in-phase drops to delay their oxidation transition, leading to the conversion of the initial in-phase to the out-of-phase pattern. It takes about 200 oscillations for the transients to die out and a final, stable oscillatory pattern to be reached. In an infinite system the final state would consist of neighboring drops oscillating 180° out-of-phase with each other, and in the space-time plot the oxidation transitions of the even (red) and odd (blue) indexed drops would form straight lines offset by half a period. In contrast, the final simulated steady state oscillatory pattern in Fig. 3.2b, is gently curved as a consequence of the influence of the boundaries propagating into the center of the sample. Later we will show that, for these conditions, samples must contain more than 40 drops in order for boundary conditions to be negligible. Since the coupling between drops is diffusive, the time for transients to decay grows as the square of the number of drops. The experimental system is over three times larger than the simulated one so we predict that it will take well over 1000 oscillations for transients to decay in an experimental system of 100 drops. Since the closed experimental system oscillates at most 100 times before the reaction goes to completion, samples of 100 drops that are started in-phase will never reach the steady oscillatory pattern.

Fig. 3.2c shows an experimental space-time plot of a 1D BZ droplets array with $m = 60$ mM. In contrast to the case of higher malonic acid, the conversion from the initial in-phase to final out-of-phase pattern is rapid. Simulations also reflect this trend.

3.1.1.1 Boundary Condition and Initial Condition

In order to make quantitative comparison with theory, we use photosensitive BZ ($Ru(bipy)_3^{2+}$ catalyzed) droplets and set both boundary and initial conditions of arrays of small numbers of oscillating BZ droplets with a programmable illumination source. In these small collections of droplets, transient patterns decay rapidly and we observe several more complex attractors, including ones in which some adjacent droplets are in-phase. As described in more detail

below, droplets held by constant illumination in the reduced state of the catalyst can act to establish constant chemical "boundary" conditions in a 1D array, so with the use of a programmable computer projector we are able to control both the boundary and initial conditions of a set of coupled nonlinear chemical oscillators. Our current set-up allows the simultaneous spatial and temporal illumination of up to 30 droplets individually in a 100 μm capillary. We can image up to 100 droplets with a different lower magnification set-up, but are no longer able to independently illuminate individual droplets. When we study capillaries with 100 droplets we illuminate the entire capillary with uniform, bright light in order to set all the drops in-phase.

We controlled the light intensity on the boundary drops to be just enough to suppress the oscillation, but not too bright so that their neighboring drops' period get elongated. For example, in Fig. 3.3 we demonstrate that if we use too much light on boundary drops (above drop #1 and below drop #9), not only themselves would be stopped from oscillating, the drops near them (drops 1, 2, 7, 8, 9) would also have longer periods compared to drops 3-6. This is caused by the overdose of light in the boundary drops and hence extra Br^- as shown in Eq. 2.15, and therefore extra Br_2 diffused into the neighbors.

Even with minimum amount of light, boundaries still affect the drops in between as shown in Fig. 3.4. We study 40 drops and start the drops with 180° out-of-phase initial conditions. The space-time pattern evolves without producing phase defects and the system evolves to a steady-state oscillatory pattern after about 100 cycles. If the number of drops is large enough, then for adjacent drops far enough away from the boundaries, $\Delta\phi = 0.5$ as shown in Fig. 3.4. The range of influence of the boundaries is a function of m. At low m, the effect of the boundaries is less than at higher m. We obtained the same results with two different boundary conditions; one corresponding to drops exposed to just enough light to suppress oscillations (constant chemical boundary, Dirichlet) and one corresponding to sealed walls at each end of the array (no flux boundary, Neumann). The interpretation of

these results is that in the limit of large 1D arrays of BZ emulsions the attractor consists of nearest neighbors oscillating precisely half a period out of phase.

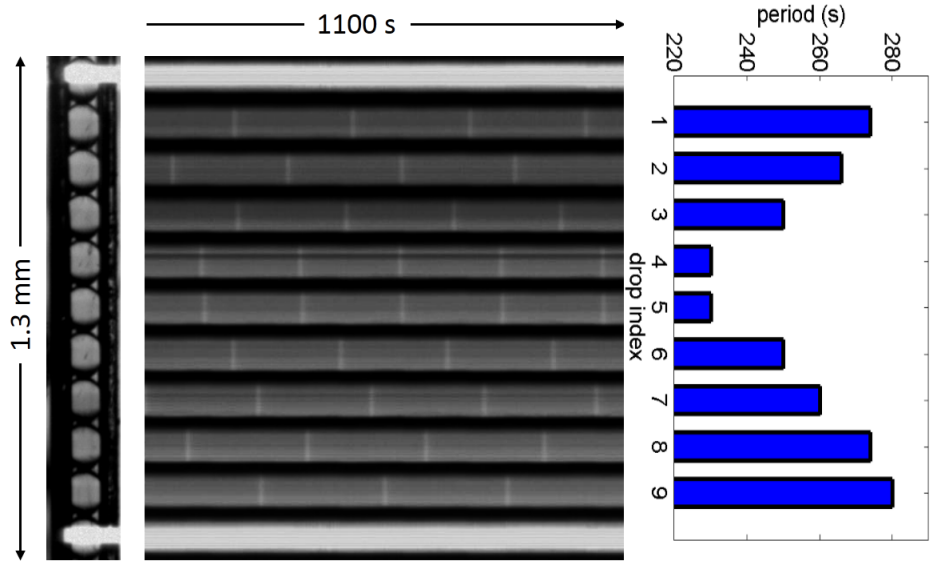

Figure 3.3: The effect of light on boundary droplets.

3.1.1.2 Results for Small Number of Droplets

We are interested in establishing whether the system of coupled oscillators has well-defined attractors and, if so, we would like to enumerate them and characterize their basins of attraction. However, as seen in the previous section, there are several experimental problems in dealing with arrays containing a large number of drops. First, the results presented above suggest that for large droplet arrays at higher m, transients in the phase difference between oscillators persist beyond the time for the BZ reaction to cease oscillation. Second, at high m the coupling is weak and the system has a tendency to drift, making it difficult to set initial conditions of the oscillators with a brief perturbation. Third, near $m = 60$ mM, where the coupling appears strongest, the anti-phase attractor is very stable and the basins of attraction of other patterns may be quite small. Finally, the approximation that m remains constant breaks down at low m. For $m < 30$ mM, the BZ drops cease to oscillate after only a few

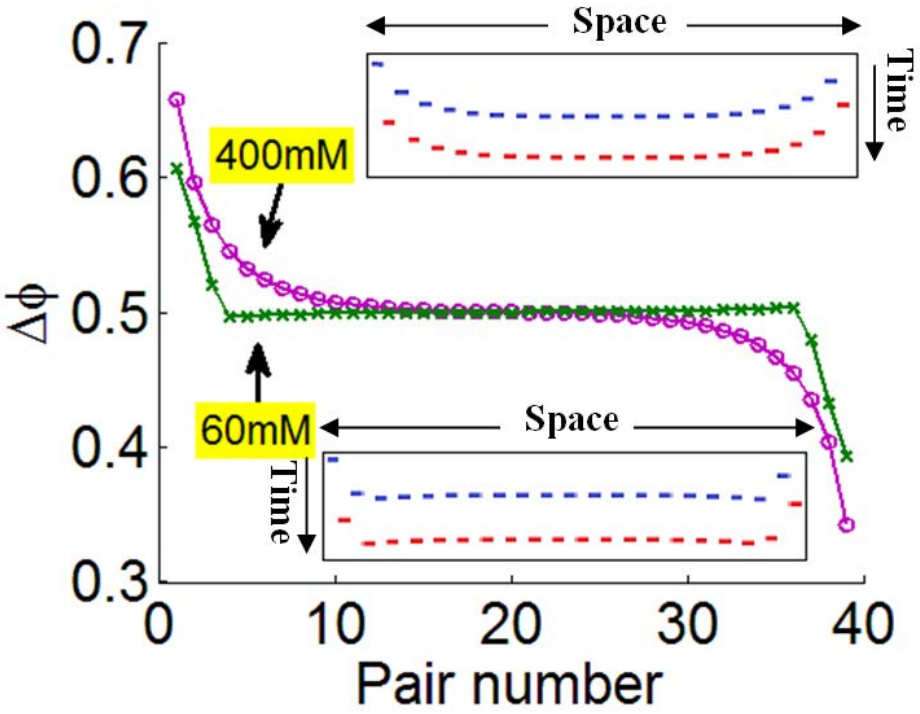

Figure 3.4: Simulation: the effect of silent boundary droplets. Simulation of the phase difference between 40 BZ drops of 200 μm diameter separated by gaps of 50 μm of oil for high (400 mM) and low (60 mM) concentrations of malonic acid. The drops on the boundary are given sufficient light to prevent oscillation; $k(I) = 10^{-4}[s^{-1}]$ for high [MA] and 10^{-3} for low [MA]. The insets contain spacetime plots from which the phase differences were derived. Blue represents odd numbered drops and red even numbered drops. One oxidation transition is shown for each of the drops. Adapted from previous work[10].

periods and the drops enter a Turing state in which some are permanently in the oxidized state and others in the reduced state, and often pairs of in-phase oscillators are observed. The solution to this set of problems is to study small groups of drops at intermediate m with well established initial and boundary conditions.

We first focus on groups of 3 - 5 droplets for m between 200 mM and 400 mM, where the phase of the droplets can easily be shifted using external light perturbation. Typically, the capillaries are filled with more than 100 droplets, but the droplets of interest are isolated from the rest of the capillary by two non-oscillatory droplets, which are fixed in the reduced state by the applied illumination, which provides symmetric boundary conditions. Additionally, by illuminating the droplets in the group of interest with a selected spatiotemporal pattern, we can place the system in a desired initial state, as illustrated in Fig. 2.2. We also attempt to reproduce our experimental results with computer simulations. All simulations in this section are done with the length of the BZ droplet, $a = 200$ μm, length of the oil gap, $b = 50$ μm, and $m = 400$ mM. In this section we adopt a particular notation to describe the phase relationship between adjacent drops, whereby the phase of a drop is indicated by a lower case letter. For example, if we have four drops with every other drop having the same phase, we refer to this situation as an "a-b-a-b" array. One important point is that, since the system is closed, it necessarily drifts away from the attractor that would exist in an open system. Thus in the experiments described below we employ simulations of open systems to identify the underlying attractor observed in experiment.

3 drops The only pattern we found with 3 droplets is the "a-b-a" attractor, in which the phase difference of the two outer droplets with the drop in the center is $\phi_{\mathrm{a}} - \phi_{\mathrm{b}} = \Delta\phi \sim 0.6$, with simplification of $\pi = 1$. This measurement is clearly distinguishable from the case when the drops are 180° out-of-phase with $\Delta\phi = 0.5$. This pattern is reached independent of the initial phases of the drops. As an example, Fig. 3.5a shows that an initial "a-a-b"

pattern is unstable and eventually evolves to the stable "a-b-a" pattern. We also explored a variety of other initial conditions, including the symmetric "a-a-a" state. Fig. 3.5b shows the experimental phase difference $\Delta\phi$ between each drop and a reference drop as a function of time extracted from the space-time data in Fig. 3.5a. Note that the first 5×10^3 s of the experiment are shown in the space-time plot of Fig. 3.5a, while 11×10^3 s of the experiment are analyzed in Fig. 3.5b. The phase difference is calculated between drops that have oscillated the same number of times. For example, even though at late times in the space-time plot of Fig. 3.5a the first and third drop undergo nearly simultaneous oxidation transitions (vertical white bars), drop 1 has undergone approximately one more oscillation than drop 3 so their phase difference is nearly 1, not 0. In Figs. 3.5b, 3.5c, and 3.5f each symbol (marker) corresponds to the occurrence of an oxidation transition, so we see that it takes 10 oscillations for drops 1 and 3 to become synchronized. This symbol convention is employed in Figs. 3.6 to 3.10 as well. Numbering the three droplets of interest from top to bottom, we observe that drop 1 initially has a shorter period than drops 2 and 3 (Fig. 3.5d), enabling it to drift out of phase with drop 2 and in phase with drop 3. Once the stable "a-b-a" pattern is established, the initially disparate periods of the drops become identical, though period τ drifts monotonically in time as previously described at high m (Fig. 3.5d). Figs. 3.5c and 3.5e show simulations corresponding to Figs. 3.5b and 3.5d, respectively. Note that, in both the experiment and the simulation, after the initial transient has died out the observed out-of-phase attractor of the center drop has $\Delta\phi \sim 0.6$ which differs from the ideal anti-phase behavior ($\Delta\phi = 0.5$) as a result of interactions with the boundary. The simulations shown in Fig. 3.4 suggest that boundary effects extend about 10 drops into the array for high m.

Since the simulations do not take into account the consumption of the reactants, once synchrony is obtained, the oscillation period in Fig. 3.5e remains constant rather than slowly increasing as in Fig. 3.5d. We suggest that the collective drift in the experimental period,

beginning at $t = 5000$ s in Fig. 3.5d, is a consequence of the system being closed. Another inadequacy in the model is that the calculated periods of oscillation do not quantitatively match the experimental periods. The inability of the FKN model to accurately calculate the period of the BZ oscillation has been discussed previously[53]. However, Fig. 3.5f shows that experiment and simulation agree when we plot the phase difference as a function of the non-dimensional period (i.e., the number of oscillations). Note in Fig. 3.5f that $\phi = 0$ is equivalent to $\phi = 1$.

4 drops For four droplets, we are able to obtain two attractors by light manipulation: "a-b-a′-b′" as shown in Figs. 3.6, 3.7 and 3.9 and "a-b-b-a" as shown in Fig. 3.8. In Fig. 3.6, an initially synchronized in-phase system ("a-a-a-a") drifts out-of-phase, but the ideal out-of-phase "a-b-a-b" attractor seen in theory to occur in the center of a large sample (Fig. 3.4), with a = 0 and b = 0.5, does not develop in the four drop case because of the influence of the boundary conditions (constant production of Br^-) created by the constant illumination of drops 0 and 5. The resulting stable attractor, shown in the simulation of Fig. 3.6c, is composed of four drops whose phases measured with respect to drop 1 are given by $(\phi_1, \phi_2, \phi_3, \phi_4) = (0.0, 0.6, 0.1, 0.5)$, which is subtly different from the ideal out-of-phase attractor of $(\phi_1, \phi_2, \phi_3, \phi_4) = (0.0, 0.5, 0.0, 0.5)$. In the experiment, Fig. 3.6b, we observe $(\phi_1, \phi_2, \phi_3, \phi_4) = (0.0, 0.55, 0.0, 0.4)$. Experiment and simulation differ by drops 2, 3 and 4 having phase differences of ~ 0.1 with respect to drop 1.

We can reach the attractor observed in Fig. 3.6 more quickly by changing the initial condition using patterned illumination, as seen in Fig. 3.7, where the initial conditions are $(\phi_1, \phi_2, \phi_3, \phi_4) = (0.0, 0.55, 0.1, 0.53)$. The simulation very rapidly reaches a steady state attractor corresponding to $(\phi_1, \phi_2, \phi_3, \phi_4) = (0.0, 0.6, 0.1, 0.5)$, and the experimental phases are quite close: $(\phi_1, \phi_2, \phi_3, \phi_4) = (0.0, 0.62, 0.12, 0.52)$.

To obtain the "a-b-b-a" attractor, we use light to phase-shift the two middle droplets

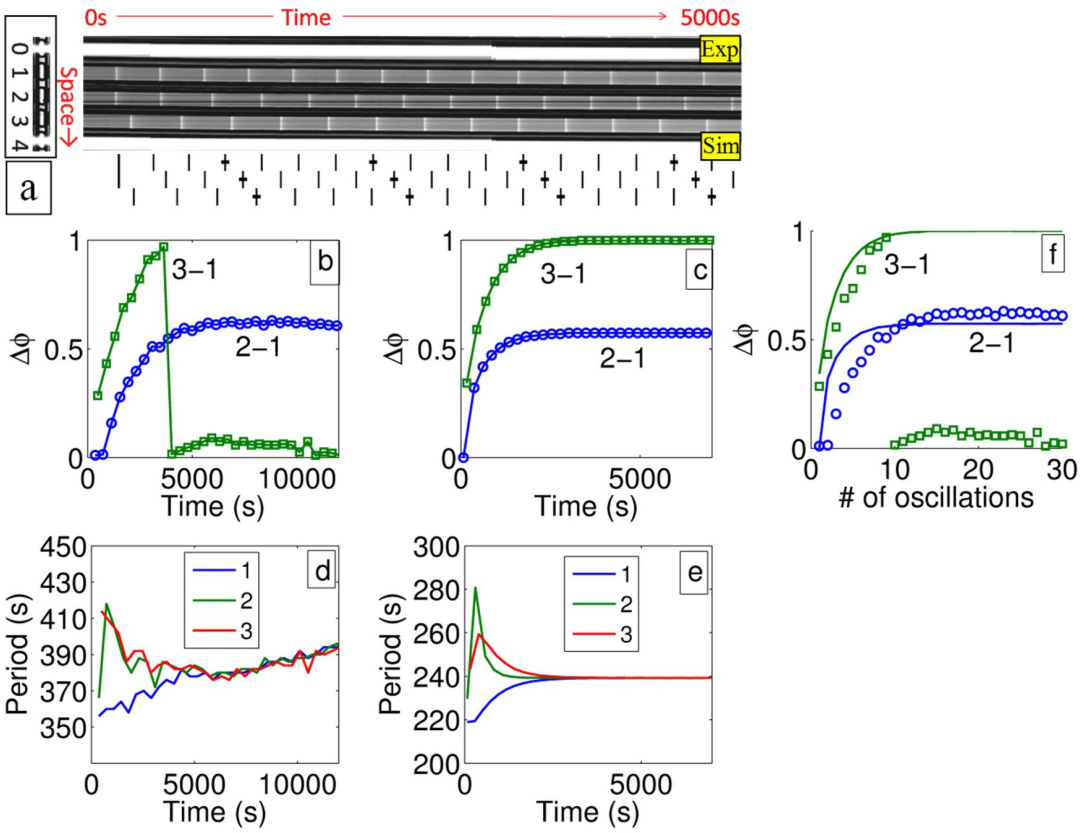

Figure 3.5: "aba" pattern for 3 drops. Temporal evolution of three BZ drops isolated by constant illumination from the rest of the capillary; symmetric attractor. (a) Exp: spacetime plot of 5 drops in the center of a 100 μm diameter capillary entirely filled with BZ drops. [MA] = 320 mM. Average BZ drop diameter, $a = 219$ μm ($\pm 1\%$); sizes of oil gaps between the oscillating BZ drops are 62 μm and 36 μm. Inset: photograph of the 5 BZ drops. Drops 0 and 4 are illuminated with constant light in order to isolate drops 1, 2 and 3 from the rest of the capillary. Initially drops 1 and 2 oscillate in phase while drop 3 is delayed. Sim: simulation of the 5 drops with same chemical and initial conditions as the experiment. The "+" symbol indicates oxidation transitions for every fourth oscillation of each drop. (b) Experimental phase difference (modulo 1) between pairs of drops, i.e. 2-1 (blue curve) means the phase difference between drop 2 and 1. Note that phase differences of 1 and 0 are equivalent. (c) Corresponding simulated phase difference. (d) Experimental and (e) simulated periods of oscillation for each droplet. (f) Experimental and calculated phase difference as a function of the number of oscillations. Adapted from previous work[10].

with respect to the outer droplets to obtain the following initial conditions; $(\phi_1, \phi_2, \phi_3, \phi_4) = (0.0, 0.4, 0.4, 0.0)$, as shown in Fig. 3.8. The two middle droplets start to oscillate after the light is removed, and they remain in-phase. The experimental $\Delta\phi$ drifts slowly. For the simulation, shown in Fig. 3.8c, the phase difference between inner and outer drops is 0.5 yielding the symmetric attractor, $(\phi_1, \phi_2, \phi_3, \phi_4) = (0.0, 0.5, 0.5, 0.0)$, which, to within slow temporal drifts, is consistent with experiment.

If we again initialize a 4-drop system by phase shifting the inner two drops with respect to the outer two drops, as in Fig. 3.8, but this time impose a slight phase difference between the two interior drops to have initial conditions $(\phi_1, \phi_2, \phi_3, \phi_4) = (0.0, 0.55, 0.53, 0.0)$, we see in Fig. 3.9 that initially the system reaches the "a-b-b-a" attractor, but then jumps to the same "a-b-a′-b′" attractor shown in Figs. 3.6 and 3.7 with $(\phi_1, \phi_2, \phi_3, \phi_4) = (0.0, 0.6, 0.1, 0.5)$. Again, within some slight temporal drift, experiment and simulation agree. Apparently, the "a-b-a′-b′" attractor has a larger basin of attraction than the "a-b-b-a" attractor.

For the system consisting of four drops, we study the temporal evolution for four different initial conditions. In each case we model the time dependence using the FKN model described in Chapter 2. The agreement between simulation and experiment of the temporal evolution of the transient initial state towards the stable attractor shown in the space-time plots and phase-difference plots is excellent. We note that there are no adjustable parameters. The only changes from case to case are the initial conditions, which are chosen to match the experiment. The agreement between theory and experiment is almost quantitative; the one discrepancy is in the period of oscillation for which the experimental period is between 1.25 and 1.5 times longer than the simulated period. The shortcomings of the FKN model with respect to period have been discussed in the literature[53]. We find two attractors for the four drop system. The one with phase pattern (0.0, 0.6, 0.1, 0.5) seen in Figs. 3.6, 3.7, and 3.9 approaches the "ideal" anti-phase pattern, where each drop is half cycle out of phase with its neighbors, as the number of drops becomes large. Interestingly, we also observe a

symmetric attractor, $(\phi_1, \phi_2, \phi_3, \phi_4) = (0.0, 0.5, 0.5, 0.0)$, shown in Fig. 3.8, whose equivalent we did not observe in experiments with larger numbers of drops.

5 drops For five droplets, the only stable attractor we find, as shown in Fig. 3.10, $(\phi_1, \phi_2, \phi_3, \phi_4, \phi_5) = (0.0, 0.6, 0.1, 0.6, 0.0)$. It is close to, but significantly different from the ideal out-of-phase pattern expected for an infinite array, where adjacent drops have a phase difference of 0.5.

In general, the experimental attractors are less stable than the corresponding simulated attractors. The consumption of chemical species during the experiment causes changes in the period of oscillation, but the drops largely remain synchronized and this only produces a small steady drift in $\Delta\phi$ compared to the simulations. In all cases, the simulated periods of the drops in the systems composed of 4 or 5 drops are systematically greater than the experimental periods by up to 50%, as noted previously[53]. Nonetheless, the simulated patterns of phase differences, including transient responses to initial conditions, agree qualitatively with the experimental ones. The consumption of chemical species (malonic acid in particular) in closed systems will be further discussed in the following section.

3.1.2 Not So Weakly Coupled BZ Droplets

Our experiments and models[34] suggest that the inhibitory coupling strength increases as m decreases. In addition, excitatory coupling *via* excitatory species $HBrO_2$ and $BrO_2\cdot$ can no longer be neglected at low m, giving new patterns that we will discuss in details in this section.

In all cases we compare experiments on closed systems with theory for open systems in which the concentrations of malonic acid, sulfuric acid and bromate ion are assumed to remain constant. This enables us to identify stable attractors and to avoid modeling the poorly understood details of malonic acid consumption. As long as the fractional change in

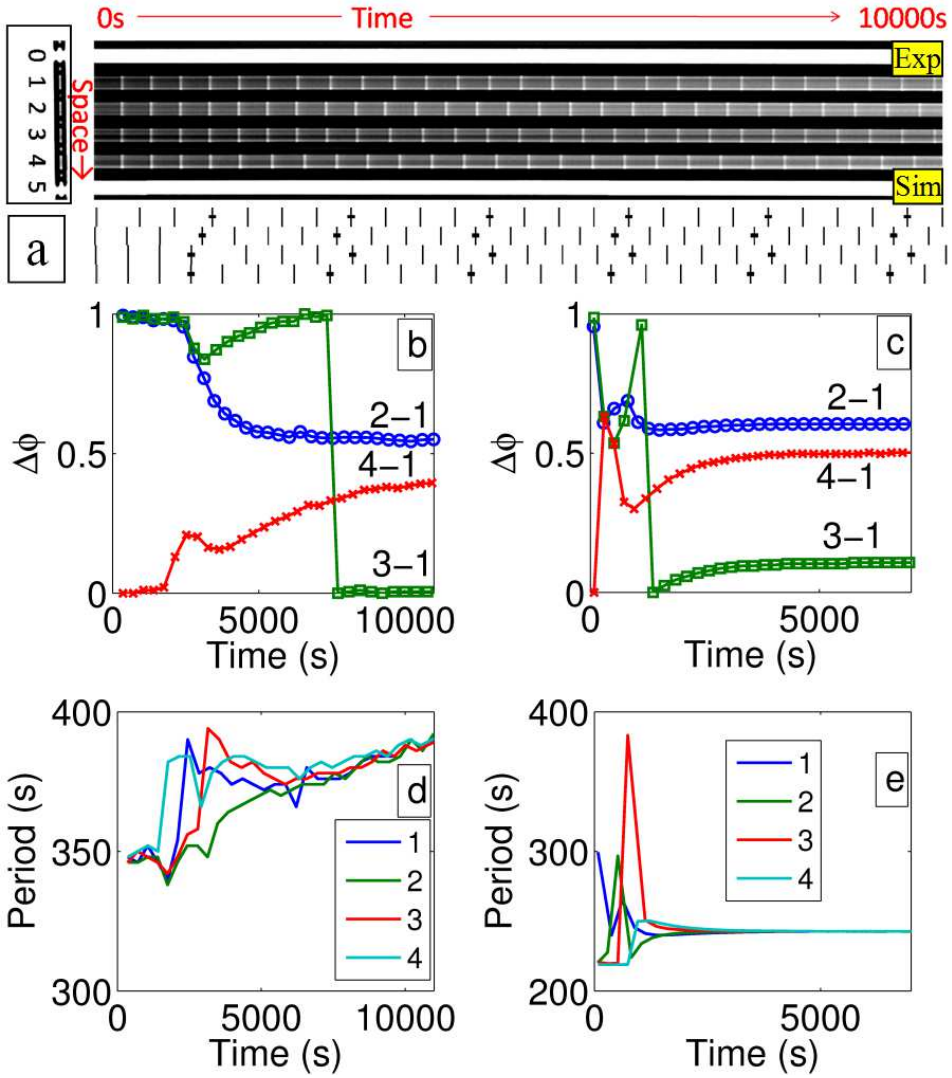

Figure 3.6: "abab" pattern for 4 drops. Temporal evolution of four BZ drops; asymmetric attractor. (a) Exp: spacetime plot of 6 drops. [MA] = 320 mM. BZ drop size, $a = 218$ μm ($\pm 1\%$), oil gap, $b = 46$ μm ($\pm 7\%$). Inset: photograph of the 6 BZ drops. Drops 0 and 5 are illuminated with constant light in order to isolate drops 1 to 4, which are initially synchronized by light and evolve to an out-of-phase pattern. Sim: simulation of the 6 drops. Every fourth oscillation is marked by a "+". (b) Experimental and (c) corresponding simulated phase difference. (d) Experimental and (e) simulated periods of oscillation for each droplet. Adapted from previous work[10].

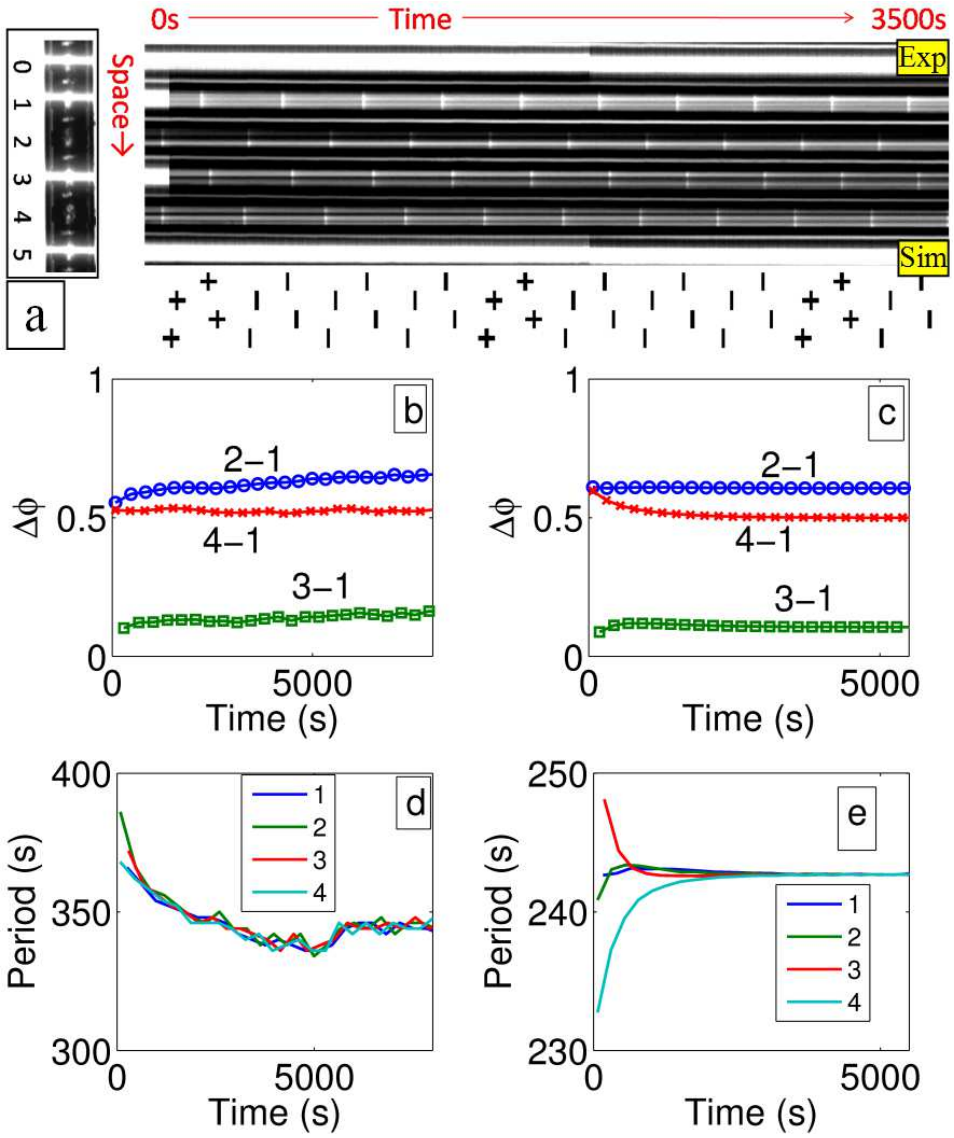

Figure 3.7: "abab" pattern for 4 drops with light perturbation. Temporal evolution of four BZ drops; asymmetric attractor. (a) Exp: spacetime plot of 6 drops. [MA]= 380 mM. $a = 116$ μm ($\pm 3\%$), $b = 17$ μm ($\pm 11\%$). Inset: photograph of the 6 BZ drops. Drops 0 and 5 are illuminated with constant light. Drops 1 and 3 are illuminated for about 300 seconds. With light perturbation, the 4 drops start with an out-of-phase pattern and reach a similar out-of-phase pattern as Fig. 3.6, but much faster. Sim: simulation of the 6 drops. Every fourth oscillation is marked by a "+". (b) Experimental and (c) simulated phase difference. (d) Experimental and (e) simulated periods of oscillation for each droplet. Adapted from previous work[10].

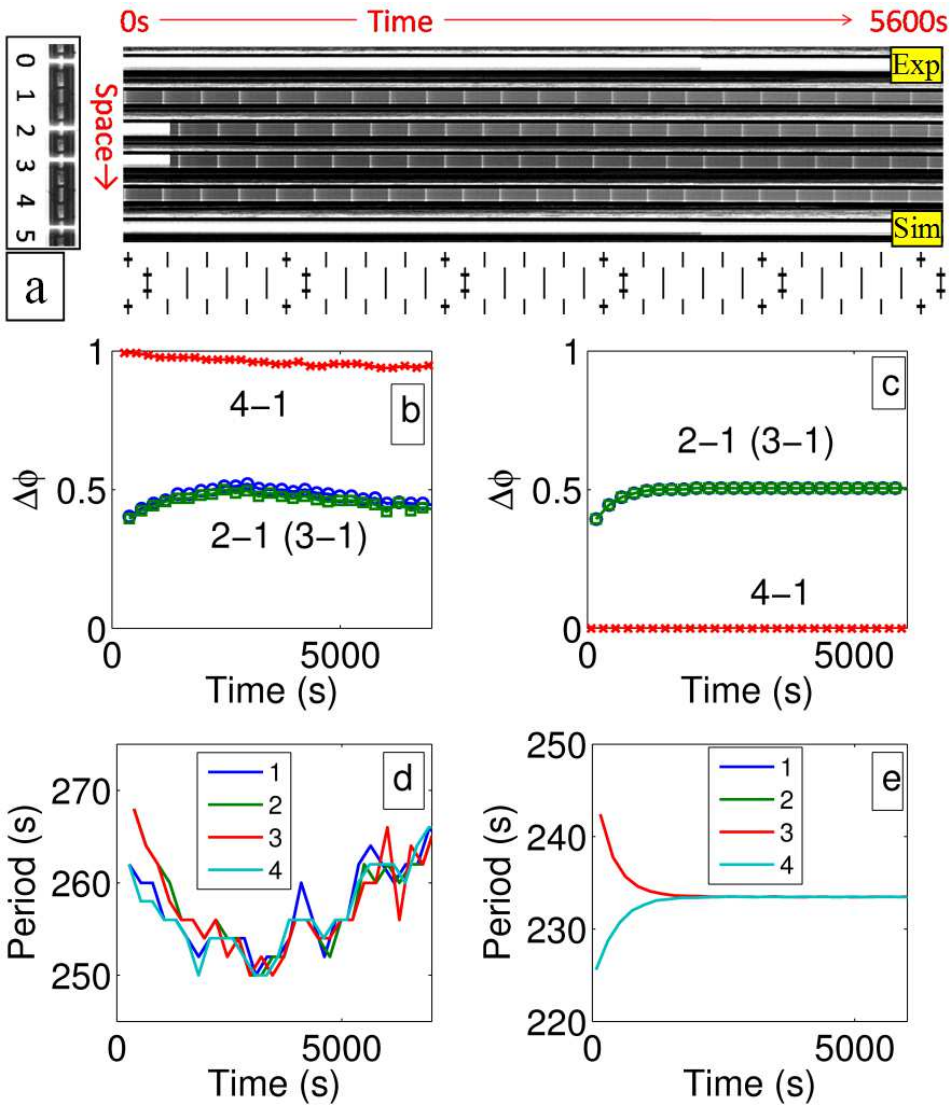

Figure 3.8: "abba" pattern for 4 drops with light perturbation. Temporal evolution of four BZ drops; symmetric attractor. (a) Exp: spacetime plot of 6 drops. [MA] = 380 mM. $a = 194$ μm ($\pm 2\%$), $b = 129$ μm ($\pm 6\%$). Inset: photograph of the 6 BZ drops. Drops 0 and 5 are illuminated with constant light. Drops 2 and 3 are illuminated for about 300 s. Sim: simulation of the 6 drops. Every fourth oscillation is marked by a "+". (b) Experimental phase difference. (c) Simulated phase difference. (d) Experimental and (e) simulated periods of oscillation for each droplet. Adapted from previous work[10].

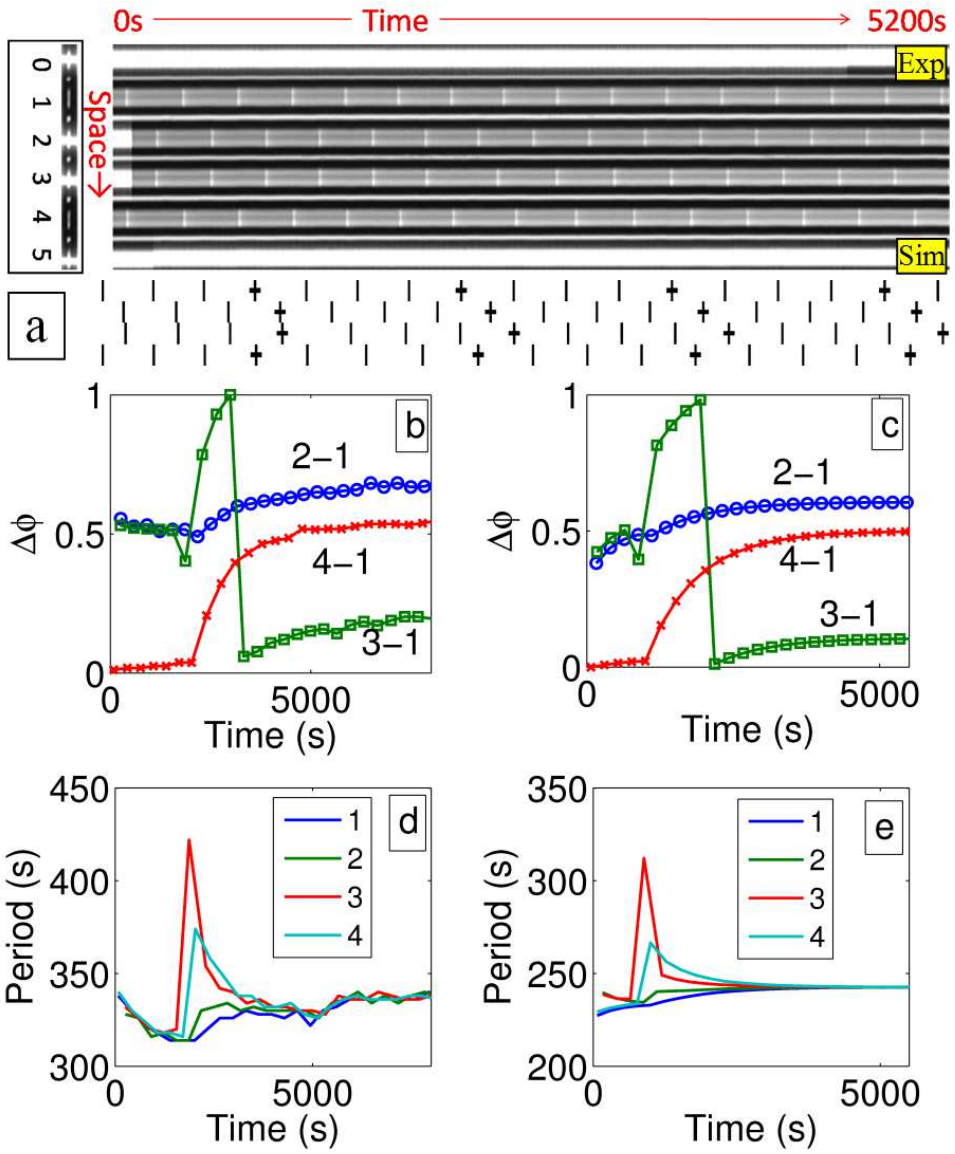

Figure 3.9: "abba" to "abab" pattern for 4 drops with light perturbation. Temporal evolution of four BZ drops; asymmetric attractor. (a) Exp: spacetime plot of 6 drops. [MA] = 380 mM. $a = 109$ μm ($\pm 3\%$), $b = 15$ μm ($\pm 12\%$). Inset: photograph of the 6 BZ drops. Drops 0 and 5 are illuminated with constant light. Drops 2 and 3 are illuminated for about 300 s. The four drops start with a symmetric attractor, as in Fig. 3.8, but evolve to the same out-of-phase attractor as in Figs. 3.6 and 3.7 after a few oscillations. Sim: simulation of the 6 drops. Every fourth oscillation is marked by a "+". (b) Experimental and (c) simulated phase difference. (d) Experimental and (e) simulated periods of oscillation for each droplet. Adapted from previous work[10].

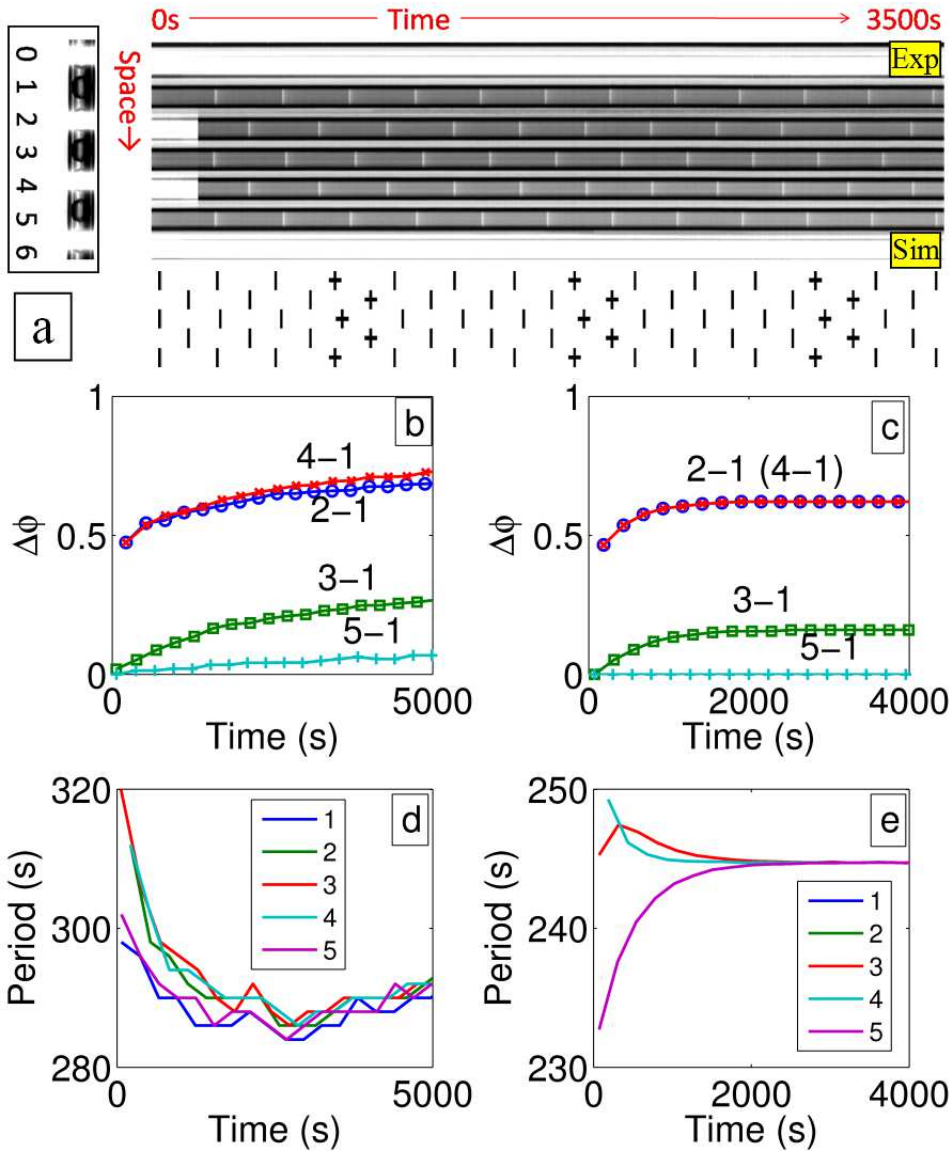

Figure 3.10: "ababa" pattern for 5 drops with light perturbation. Temporal evolution of five BZ drops; symmetric attractor. (a) Exp: spacetime plot of 7 drops. [MA] = 210 mM. a = 135 μm ($\pm$1%), b = 48 μm ($\pm$15%). Inset: photograph of the 7 BZ drops. Drops 0 and 6 are illuminated with constant light. Drops 2 and 4 are illuminated for about 300 s so that the 5 drops start with an out-of-phase pattern. Sim: simulation of the 7 drops. Every fourth oscillation is marked by a "+". (b) Experimental phase difference. (c) Simulated phase difference. (d) Experimental and (e) simulated periods of oscillation for each droplet. Simulated drops 1 and 5 have equal periods, as do drops 2 and 4. Adapted from previous work[10].

the concentrations of these three chemicals is small, the experiments on the closed systems and our simulations of of the open systems agree well.

Here we consider systems in which the m is smaller than the sulfuric acid and bromate ion concentrations, so the consumption of malonic acid represents the greatest difference between the open and closed systems. To compare theory and experiment, we prepare a series of BZ emulsions as a function of m and compare the initial behavior of each of these emulsions, which are closed systems, with the corresponding theoretical open systems. Pursuing the same logic, we reason that the time dependence of a single closed system can be qualitatively mapped onto a series of open systems with decreasing m.

In our numerical investigations of open systems, steady state dynamical patterns are identified as attractors. Technically, no attractors exist in the closed system, because the only steady state is equilibrium. However, as we previously demonstrated, our closed system gives rise to "pseudo-attractors" that maintain an oscillatory pattern for many periods and have the same dynamic behavior as the true attractors found in simulations of the corresponding open system[10].

3.1.2.1 Consumption of Malonic Acid in Closed System

In Fig. 3.11 we present an experiment that is representative of many of the phenomena observed for BZ drops at low malonic acid. Consider the complex behavior illustrated in the space-time plot of Fig. 3.11c. In the beginning, drops are synchronized to begin oscillating in-phase, but with time drift out-of-phase. At the end, some drops (e.g., #4, #5 and #6) switch back to in-phase, while some others (e.g., #2) stop oscillating.The oscillation period is longer for drops that are out-of-phase with their neighbors than for in-phase drops. The period increases with time, and the oscillation waveform of the oxidation/reduction of ferroin changes with time. All of these phenomena will be explained as a consequence of the consumption of malonic acid, leading to increased inter-drop coupling.

Proceeding in detail, Fig. 3.11a is a photograph of a 100 μm inner diameter hydrophobized capillary filled with BZ drops that are in contact with each other. The oil wets the capillary, and surface tension causes the drops to adopt a cylindrical shape with hemispheres on the end. Fig. 3.11b shows 120 μm long BZ drops (red arrows) separated by 40 μm oil gaps (green arrows) in a non-hydrophobized capillary. Fig. 3.11c shows a space-time plot of the BZ drops in Fig. 3.11b with initial $m = 40$ mM. With these initial conditions, the drops spontaneously oscillate. All the drops are initially synchronized to have the same phase by first suppressing the oscillations via strong illumination for several minutes and then removing the light from all the drops simultaneously. During the first two oscillations, drops #1 through #6 oscillate in-phase while drop #7 is out of phase. With time, the remaining drops sequentially fall out of phase starting with drop #6, then #5, etc. By the 12th oscillation, all seven drops are out of phase with each other. However, at the 14th oscillation, drops #5 and #6 synchronize in-phase and at the 15th oscillation, drops #4, #5, and #6 are synchronized in-phase. At this time, drops #1, #2, and #3 stop oscillating altogether. During the out-of-phase regime of the first 15 oscillations, the phase-shift between adjacent droplets is never π (180°). For instance, the phase-shift between droplets #6 and #7 is less than 0.7π during most of the experiment. As previously reported, such a condition during the out-of-phase regime can be considered as a mark of weak inhibitory coupling[10]. Our explanation for the evolution over time from in-phase to out-of-phase behavior for the first 15 oscillations is that the initial in-phase condition, set by the imposition of light, is unstable, and the systems evolves towards the stable anti-phase attractor. However, over time m decreases as it is consumed in the closed system. Our numerical studies of a pair of interacting drops in an open system reveal that at low m the diffusive coupling of Br_2, $HBrO_2$, and $BrO_2\cdot$ leads to bistability between in-phase and out-of-phase attractors, which explains why after 15 oscillations some of the drops adopt an in-phase attractor[34]. Finally, at lower m some drops stop oscillating. We identify those drops with stationary Turing states, triggered by

strong inhibitory coupling, which are predicted to be bistable with in-phase attractors at very low m[34].

Fig. 3.11d shows the period as a function of time for each of the seven droplets as numbered on the space-time plot. The periods for the droplets that oscillate in-phase and for the droplets oscillating out-of-phase with adjacent neighbors evolve along two different lines. At the beginning of the experiment, only one droplet (#7) is out of phase with the other drops and lies on the out-of-phase line, which has a longer period than the in-phase drops at the corresponding time. Once a droplet moves from the initially unstable in-phase behavior to the more stable out-of-phase attractor, the period increases and the drop switches to the upper line. This process occurs more gradually in droplet #1, which does not go back to in-phase interaction. At a later stage some droplets, e.g. #5 and #6, return to their earlier in-phase behavior and consequently, their period decreases. Fig. 3.11e shows the temporal behavior of a single drop that is extracted from an array of interacting drops with initial conditions $m = 60$ mM, $A = 600$ mM and $h = 320$ mM (double the default condition). The intensity of transmitted light, which is proportional to the ferroin concentration, is also plotted as a function of time. There is a noticeable lengthening of the period and change of duty cycle, defined as the fraction of each cycle spent in the oxidized state, with time. Oscillations with a long duty cycle of the oxidation state are observed in low m solutions, while the oscillations have a short duty cycle at high m[34, 54]. Fig. 3.11f shows how the ferroin concentration, calculated in the point oscillator model for a pair of coupled drops in steady state, varies as a function of time for different values of m. Matching the waveform from the calculation with the observed waveforms in Fig. 3.11e allows us to estimate how m varies as a function of time. For this range of conditions we find $m(t) = 60[\text{mM}] - 0.03[\text{mMs}^{-1}]t[\text{s}]$. Fig. 3.11g shows the numerically calculated period (based on the FKN model) of a single BZ droplet as a function of malonic acid concentration. The period increases as m decreases; thus all the observations in Fig. 3.11 are consistent

with a decreasing concentration of malonic acid in the drops with time.

3.1.2.2 Excitatory coupling and in-phase behaviors

trigger waves Using $m = 40$ mM and droplets in contact, or using $m = 20$ mM and more closely spaced droplets than in Fig. 3.11, we were able to obtain a stable in-phase behavior of large arrays of 1D droplets as observed in Fig. 3.12 (a-d). We were unable to observe such patterns for 40 mM $< m <$ 2 M. In contrast with previously reported unstable in-phase patterns3, the stable patterns found here often (but not always) initially begin with zero phase shift between adjacent drops and subsequently develop a small, but constant phase shift between adjacent droplets, creating a propagating BZ wave, analogous to the behavior observed in a continuous aqueous BZ solution.

We simulated the observed wave pattern using COMSOL to model a chain of 2D disks in oil. We postulated that the waves observed experimentally in Fig. 3.12 b, d were trigger waves. To numerically explore this possibility we set one drop on the edge of the simulation box to have a higher concentration of sulfuric acid than the other drops, causing that drop to oscillate faster than the other drops and thus act as a trigger (Fig. 3.12 g, h). We compared experiments showing traveling waves in drops in cylindrical capillaries with simulation and found similar behavior. To validate the simulations, we modeled a continuous BZ solution confined in the same capillary and compared with experiment. Again the simulation and experiment were similar, as illustrated in Fig. 3.12 (e-h). The one discrepancy was that the frequency of the oscillation in the simulation was about twice that found in the experiment. This is a shortcoming of the FKN model, and not a consequence of the finite element aspect of the calculation. This discrepancy in oscillation frequency led to the wave speed in simulation being twice as fast as in experiment; however, the calculated wavelength agreed with experiment. In both simulation and experiment, the speed of the trigger wave in the continuous BZ fluid was twice the speed of the wave in the chain of drops. The oil gap

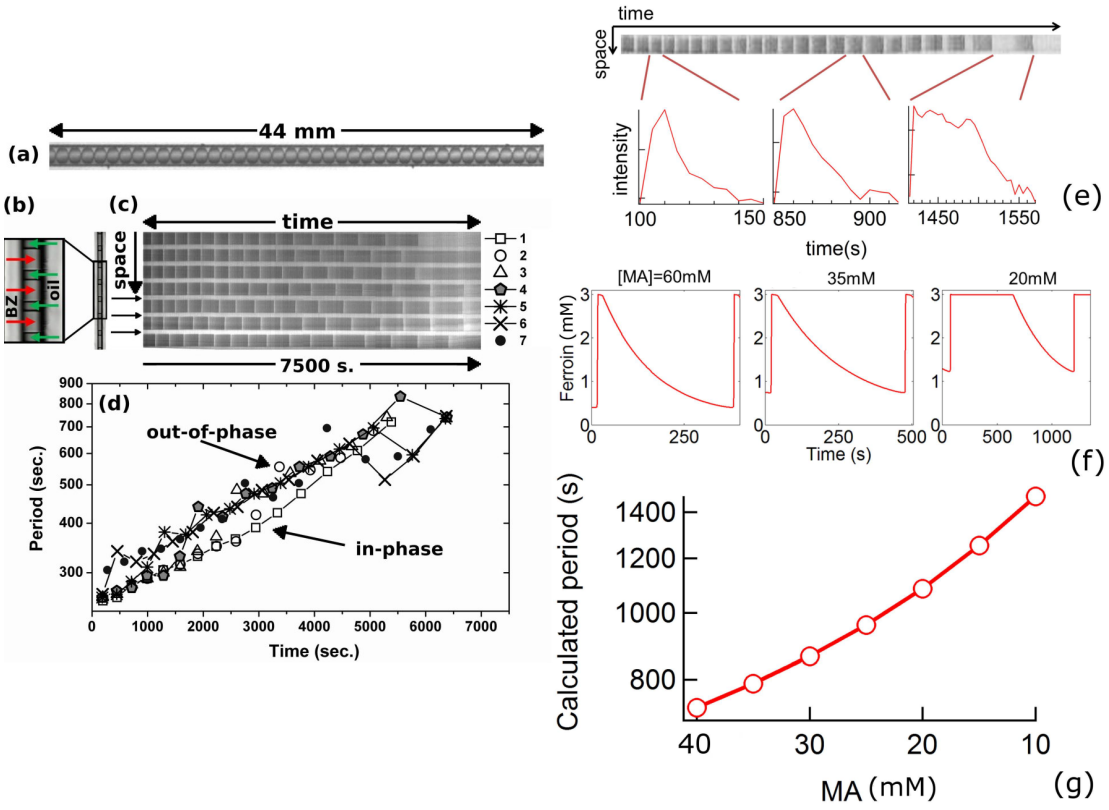

Figure 3.11: Low malonic acid concentration BZ oscillations in a 1D array of drops. (a) Photograph of section of a hydrophobized cylindrical capillary of 100mm inner diameter filled with drops containing the BelousovZhabotinsky reaction. The drops are separated by fluorinated oil. (b) Magnified section of an unhydrophobized capillary containing BZ drops (red arrows) separated by oil (green arrows). Droplet diameter, $a = 120$ μm. Oil gap, $b = 40$ μm. (c) Space-time plot of seven drops shown in (b). Three arrows indicate the oil gaps between drops, which appear as bright lines running parallel to the time axis, because the light transmitted through the oil gap is constant in time. Bright lines parallel to the space axis correspond to the oxidized state of the BZ reaction. (d) Period vs.time for the seven drops shown in the space-time plot of (c). Initially, [MA] = 40 mM. (e) Transmitted light intensity through one drop as a function of time. The intensity profile as a function of time for the 2nd, 15th, and 22nd oscillations. (f) Calculated ferroin concentration vs. time for different concentrations of malonic acid, with $[BrO_3] = 600$ mM and $[H_2SO_4] = 80$ mM, $a = b = 150$ μm. (g) Calculated oscillation period vs. malonic acid concentration for a single BZ droplet, using default chemical conditions: $[BrO_3] = 300$ mM and $[H_2SO_4] = 80$ mM. Adapted from previous work[17].

diminishes the diffusive flux in comparison to the continuous BZ solution, offering a possible explanation for the slower propagation speed in the drops.

To explore the origin of the temporal evolution of the phase between adjacent drops from initially zero phase to a constant phase as shown in Fig. 3.12, we repeated the trigger-wave simulations of Fig. 3.12 g, h as a function of inter-drop coupling strength. In Fig. 3.13a we simulate a line of identical drops, except for one drop on the end, which has a higher frequency. The drop spacing is 60 microns, large enough that the fast drop does not launch a trigger wave, but the drops are still sufficiently coupled to oscillate in phase. Simulated light was shone on the middle drop with sufficient intensity to suppress oscillation in that drop. One observes that drops immediately adjacent are slightly influenced by the increased bromine produced by the illuminated drop. In Fig. 3.13b the inter-drop separation is reduced to 20 μm. Now a trigger wave is formed, but does not propagate across the light-induced gap. From these simulations we conclude that trigger waves require a stronger coupling between drops than do in-phase attractors with zero phase shift between neighbors. Fig. 3.13c shows an equivalent experiment. The drop in the center of the capillary is illuminated, suppressing its oscillation. The drops initially oscillate with zero phase shift between neighbors, but with time, a traveling wave emerges as the malonic acid concentration decreases and the coupling strength consequently increases.

cluster patterns In Fig. 3.14a, we present a space-time plot highlighting three pairs of in-phase droplets numbered 1 - 6. The pattern consists of a row of drops in which at a particular instant in time all drops form pairs where drops in a pair have the same phase, but each pair is 180° out-of-phase with its neighboring pairs, i.e. drops #1 and #2 have 0° phase, drops #3 and #4 have 180° phase and drops #5 and #6 have 0° phase. We refer to this pattern as a "local in-phase, global out-of-phase" attractor. In Fig. 3.14b we observe defects in this synchronization pattern that occur when there is an additional drop

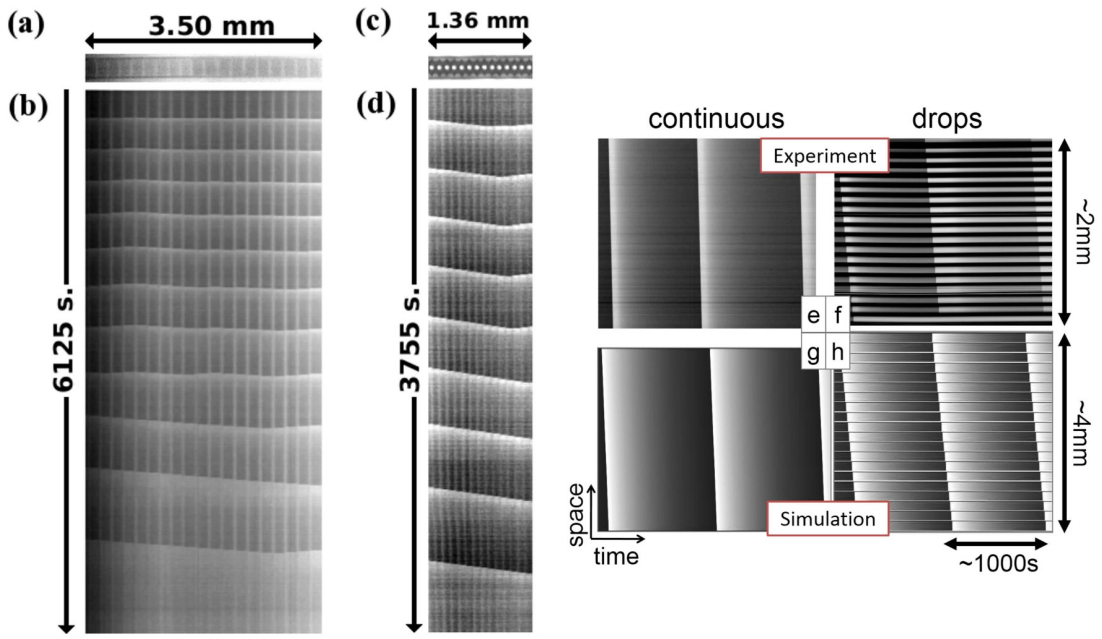

Figure 3.12: In-phase patterns: Trigger wave experiments vs. simulations. (a, c) photographs of drops in capillary. (b, d) Space-time plots. (a, b) [MA] = 20 mM, (c, d) [MA] = 40 mM. Droplet diameter is (a, b) 150 μm and (c, d) 97 μm; distance between droplets is (a, b) 36 μm and (c, d) touching droplets. (e) Experiment: single phase BZ solution ([MA] = 20 mM). Trigger wave speed 2 mm min^{-1}. (f) Experiment: BZ droplets (100 μm), trigger wave speed 1 mm min^{-1}. (g) Simulated in COMSOL, single phase using [MA] = 20 mM. Trigger wave speed, 4 mm min^{-1}. (h) Simulated in COMSOL, BZ droplets (200 μm), trigger wave speed 2 mm min^{-1}. The topmost droplet has slightly higher [H$^+$] = 0.2 M than the rest of the droplets (0.16 M) to act as an intrinsically faster "trigger". $P_{\mathrm{HBrO_2}} = 0$, $P_{\mathrm{Br_2}} = 2.5$, $P_{\mathrm{BrO_2\cdot}} = 5$. Identical results are obtained with $P_{\mathrm{Br_2}} = 2.5$, $P_{\mathrm{HBrO_2}} \approx 0.01$ and $P_{\mathrm{BrO_2\cdot}} = 1$. Adapted from previous work[17].

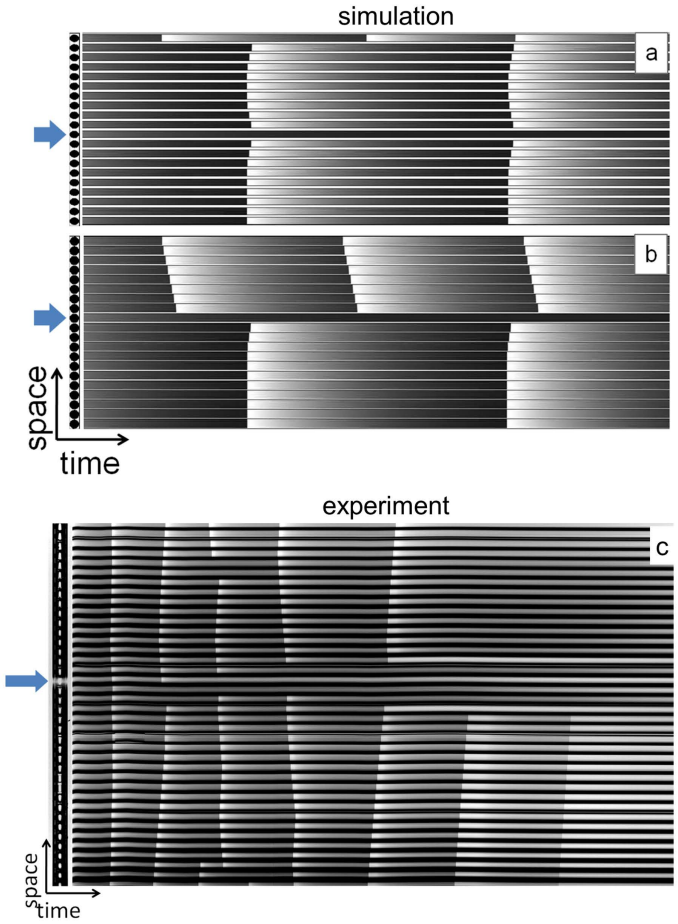

Figure 3.13: Traveling waves and coupling strength. Blue arrows indicate light suppressed BZ drops. (a, b) COMSOL simulations ([MA] = 20 mM, $P_{\mathrm{HBrO_2}} = 0$, $P_{\mathrm{Br_2}} = 2.5$, $P_{\mathrm{BrO_2}} = 5$): (a) drop size $a = 160$ μm, oil gap $b = 60\mu$m. (b) $a = 200$ μm, $b = 20$ μm, light intensity 0.01 s^{-1} (pseudo concentration in the model). In both (a) and (b) the first drop (top, $[\mathrm{H}^+] = 0.22$ M) is made to oscillate faster than the other drops ($[\mathrm{H}^+] = 0.16$ M). The light-suppressed drop in the middle separates the drop array into two parts in each case. Trigger wave behavior is observed only in (b), where the inter-drop coupling is stronger, but in-phase attractors are observed for both (a) and (b). (c) Experiment ([MA] = 20 mM, $a = 100$ μm, $b = 10$ μm). Although the a/b ratio in this experiment is the same as in (b), the result resembles (a). The experiment started with an in-phase attractor with zero phase shift between drops and evolved into a trigger wave. Adapted from previous work[17].

separating two pairs, i.e. drops #1 and #2 have 0° phase, drops #4 and #5 have 180° phase and drop #3 is the defect. In this case, the droplet separating the two pairs (drop #3) alternately synchronizes in-phase with the neighboring pairs to each side; a feat that is only possible when the middle droplet oscillates with twice the frequency of its neighbors. As in the case of the stable in-phase patterns in Fig. 3.12, the patterns observed in Fig. 3.14 require low m and/or droplets with small separation. We observed these local in-phase - global out-of-phase modes for m up to 60 mM, as observed in Fig. 3.14c. At higher m, even touching droplets yield only out-of-phase patterns[10]. Typically, as the BZ reaction proceeds towards equilibrium, oscillations eventually give way to a stationary Turing pattern with some drops locked in the oxidized state and others in the reduced state.

Often, the local in-phase - global out-of-phase pattern is mixed with "pure" out-of-phase behavior or with stationary droplets. In Fig. 3.14a, on either side of the pairs of highlighted arrowed regions, we observe drops where nearest neighbors are out-of-phase, while in Fig. 3.14b the right side of the space-time plot shows stationary droplets while the left side remains oscillatory. When the pattern includes stationary droplets, as observed in Fig. 3.14b and c, the stationary droplets produce a variety of complex, often symmetric, patterns. In Fig. 3.14c we observe periodic stationary Turing patterns with wavelengths of 4 drops; in Fig. 3.14b the Turing wavelength is 3 drops. The most commonly observed in-phase clusters consist of a pair of droplets, and the number of droplet clusters drops off sharply with the size of the cluster.

3.2 Measurement of Coupling Strength

Theoretical models of coupled BZ oscillators are necessarily simplified, not only because of the complexity of the chemical kinetics of the reaction, but also because the degree to which the chemicals partition into the oil and their reactivity within the oil is poorly known.

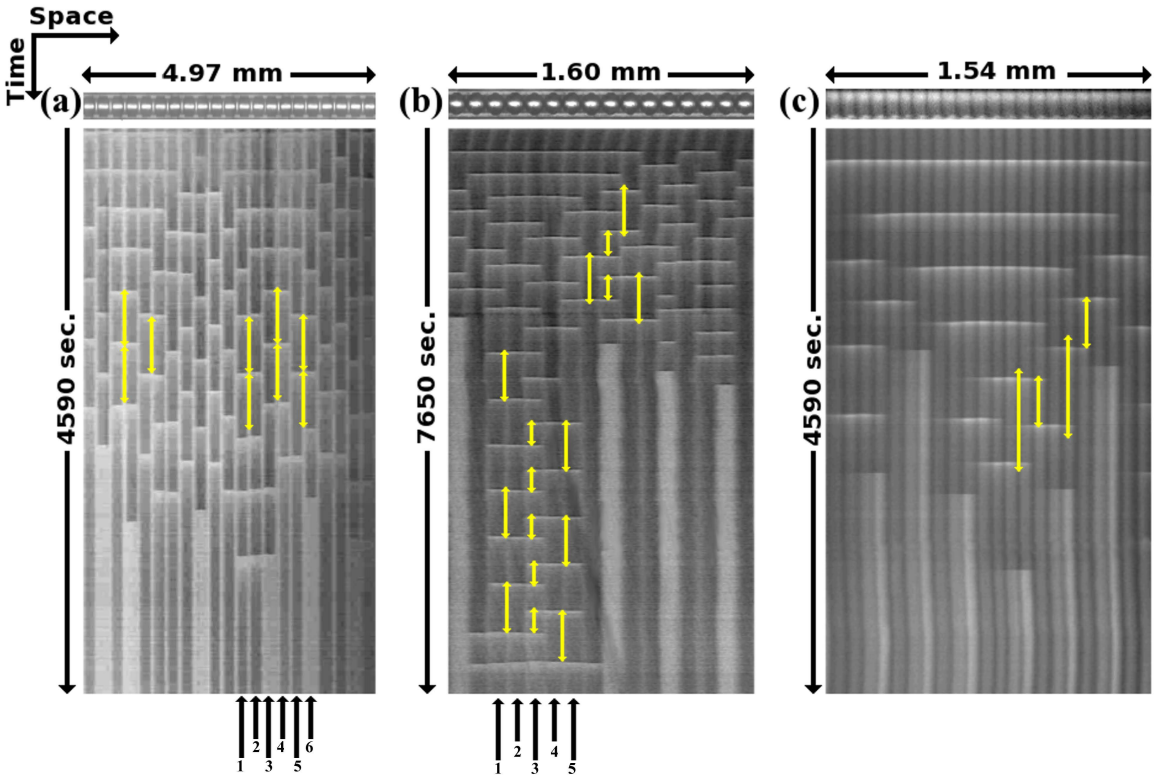

Figure 3.14: Space-time plots of mixed mode patterns. (a) Droplets are 170 μm in diameter separated by 70 μm oil gap, [MA] = 20 mM. (b) Droplets of 100 μm diameter are in contact, [MA] = 40 mM. (c) Droplets of 70 μm diameter are in contact, [MA] = 60 mM. Before starting each experiment, the droplets were synchronized in-phase by illuminating the capillary with intense 450 nm light for about 10 min. In the space-time plots, long double arrows mark periods of at least two in-phase neighbor droplets; short arrows, half the size of the long arrows, mark the period of a single droplet Adapted from previous work[17].

However, because the kinetics within the microdroplets are the same as in the macroscopic BZ reaction, one can make use of well-established detailed models[30, 31] as a starting point.

We model the coupled BZ drops at three levels of approximation. The most realistic consists of a finite element model (COMSOL) of the reaction-diffusion equation in 1D, 2D and 3D, where each drop is modeled as a point, disk or sphere, respectively. Only minor differences are observed between 1D, 2D and 3D drops arranged periodically in a straight line. The capillary walls are treated as a no-flux boundary condition. The reaction term is modeled using the 7-variable FKN model as detailed in Chapter 2. Chemicals are allowed to diffuse within the drop and the oil and to exchange between the two phases governed by a partition coefficient, P, defined as the ratio of equilibrated concentrations of a particular species in the oil and water phases ($P = c_{\text{oil}}/c_{\text{water}}$). This boundary conditions at the oil-water interface are enforced in COMSOL using the stiff-spring method (as demonstrated in the "dialysis" model in COMSOL's built in examples) to have the right partition coefficients. Each chemical species has the same diffusion constant in the oil and the water. No chemical reactions are allowed to occur in the oil, which we find experimentally is not the case[17]. However, we argue that this simplification is justified for most of the cases studied here. Models of intermediate complexity approximate each spatially extended drop as a 7-variable FKN oscillator confined to a single point. The BZ drops are diffusively coupled to their nearest neighbors. This class of models, consisting of a ring of diffusively coupled point-like chemical reactors, was first introduced by Turing[1]. We numerically solve the point model using MATLAB. The diffusion across a 100 μm sized droplet takes very little time comparing to the oscillation period, so the droplets are oscillating homogeneously. Thus the point model is justified. The point model and finite-element model give similar results for 1D systems. Finally, at the most abstract level, we construct a single variable phase oscillator model as introduced in Chapter 2, in which the phase coupling function is derived from the point oscillator model.

3.2.1 Inhibitory Coupling Strength: Finite Element Analysis

Previous experimental studies[19, 9, 10] of a large number of equal spaced droplets inside a cylindrical capillary found anti-phase attractors, in which adjacent drops oscillated 180° out of phase with each other. This occurred for a wide range of droplet diameters a, length of oil gap between droplets b and intermediate malonic acid concentration m. This anti-phase behavior was explained to be a result of inhibitory coupling of the drops, which arises from the diffusion of bromine (Br_2) between droplets. For clarification, in the aqueous BZ reaction, inhibition is carried out by bromide ion (Br^-), but this charged species does not partition into the oil. However, Br_2, which is nonpolar, partitions readily into the oil and diffuses from drop to drop. Once inside the aqueous phase, Br_2 brominates MA, generating Br^-; thus Br_2 acts as the carrier of inhibition, and not as the inhibitor itself (Eq. 2.4). Our results suggest that this bromination can be characterized by an effective rate constant $k_{\text{eff}} = 10[\text{s}^{-1}] + 29[\text{M}^{-1}\text{s}^{-1}]m$.

3.2.1.1 Origin of Coupling: Diffusive Flux

In Fig. 3.15a, we present the results of solving a reaction-diffusion finite element model of the FKN equations. The model accounts for the permeation of the activators bromine dioxide and bromous acid, as well as bromine, which couples to the inhibitory reaction, into the oil separating the BZ drops. We modeled the drops as spheres contained in a cylindrical capillary whose inner diameter matches the sphere diameter. We also modeled the spheres as lines in 1D and disks in 2D and found only minor quantitative differences between the 1D, 2D and 3D solutions. To investigate how two drops interact, we ran simulations on three configurations: two drops of diameter "D" separated by "0.1D" to represent conditions of strong coupling, two drops of diameter "D" separated by "10D" to represent conditions of weak coupling, and a single drop as a reference for comparison. In Fig. 3.15 the drops are 200 μm in diameter filled with BZ solution with $m = 20$ mM in a two-dimensional, rectangular,

impermeable container filled with oil.

The observation that the period of a pair of 180° out-of-phase droplets is longer than that of a pair of drops with 0° phase shift[9], which was described in Fig. 3.11d, can be explained by examining Fig. 3.15b, in which the concentration of Br_2 in the center of the left drop and in the oil gap separating the two drops is plotted as a function of time. Bromide (Br^-) inhibits the BZ oscillation. Injection of a pulse of Br^- into a homogeneous stirred BZ solution lengthens the period of oscillation, because additional time is required for removing it, which is required in order to start the autocatalytic BZ step[55, 56]. However, it is Br_2 and not Br^- that is transmitted between drops. Br_2 is rapidly produced in a drop when it undergoes the oxidation transition. If two drops are out-of-phase, then the pulse of Br_2 produced in one drop (the transmitter) diffuses to its neighbor (the receiver), where it is converted to Br^-, thereby delaying the oscillation of the receiving drop.

The dashed blue curve ("10D drop") in Fig. 3.15b shows the temporal variation of $[Br_2]$ in the center of drop 1 in a closed container with drop 2 located 10 diameters away. In a second calculation involving a container with a single drop, the temporal variation of $[Br_2]$ is shown as the dashed green curve ("one drop"). The location of drop 1 and the size of the container were the same as in the "10D drop" calculation, but drop 2 was removed and replaced with oil. The temporal variation of $[Br_2]$ for two drops separated by 10 diameters ("10D drop") is indistinguishable from the case of one drop in a sealed container of the same size ("one drop"), which indicates that when drops are 10 diameters apart they are decoupled.

When the drops are brought close to each other (a gap of 0.1 drop diameter) the Br_2 concentrations are significantly distorted, as shown in Fig. 3.15b "0.1D drop". Compared to the case of drops far apart, during half the cycle the level of Br_2 inside drop 1 is depressed and in the other half of the cycle the Br_2 level in the same drop is elevated. The explanation is that as the drops are out of phase with each other, when drop 1 undergoes the oxidation

transition at $t = 1778$ s, it emits a large amount of Br_2 at the moment when the Br_2 level in its neighbor, drop 2, is low. Thus drop 2 acts as a sink of Br_2 leading to a reduction in $[Br_2]$ in drop 1 compared to the case when the drops are greatly separated. Likewise, when drop 2 oxidizes at $t = 2400$ s, it emits a pulse of Br_2, raising the Br_2 level of drop 1 above its value when the drops are far apart and causing the period of oscillation to lengthen. Note that the diffusive coupling is fast when the drops are separated by an oil gap of 20 μm; thus drop 1 receives the pulse of Br_2 less than 1 s after it is emitted by drop 2 at 2400 s.

Fig. 3.15a shows the flux and concentration of Br_2 and Fig. 3.15b plots the concentration as a function of time. We also measured the total flux in and out of a drop as a function of partition coefficient in steady state conditions (not shown). Under these conditions the total flux is zero. We found that the flux out of a drop increased monotonically with partition coefficient in steady state, however it is not clear how to quantitatively relate the chemical flux to the degree of dynamical coupling between drops.

3.2.1.2 Dimensional Analysis and *S* Parameter

One heuristic measure of the coupling strength is the dimensionless number $S = P_{Br_2}D/(a(a+b)k_{\text{eff}}) = \mu/k_{\text{eff}}$, which is the ratio of two rates: $\mu = P_{Br_2}D/(a(a+b))$, the rate of diffusive transport between BZ drops of the inhibitor bromine separated by an oil gap, and k_{eff}, the effective rate constant characterizing the consumption of Br_2, which as described previously, occurs *via* bromination of malonic acid. Here P_{Br_2} is the partition coefficient, D is the diffusion coefficient of bromine, a is the BZ droplet size, b is the oil gap size. The derivation of μ (assuming the drop-oil interface is flat) is presented in Chapter 2; an alternative expression for μ using the Derjaguin approximation considering the actual curvature of the drops was derived in previous work[15].

In order to estimate k_{eff}, we plot the concentration of Br_2 as a function of distance in Fig. 3.15c at $t = 1778$ s, just after the drop on the left is oxidized, as depicted in Fig. 3.15a.

If the time for bromine to diffuse across a drop is short compared to the oscillation period, then $\partial c(x,t)/\partial t$ can be neglected. For $D = 10^{-5}[\mathrm{cm^2 s^{-1}}]$ and $a = 10^{-2}[\mathrm{cm}]$ the time for Br_2 to diffuse across the drop, $\tau_D = 10$ s, is much shorter than the oscillation period, which is greater than 300 s. The solution to the time-independent reaction-diffusion equation is an exponential with a characteristic decay length $\lambda = \sqrt{D/k_{\mathrm{eff}}}$. We define λ as the distance from the water/oil interface to the point that the Br_2 concentration is reduced halfway to its minimum. We find λ is constant in time, supporting the contention that $\partial c(x,t)/\partial t$ is negligible. In Fig. 3.15c we plot λ^{-2} *vs.* m and numerically find that k_{eff} is linear in m; $k_{\mathrm{eff}} = 70[\mathrm{M^{-1}s^{-1}}]m$. This result is roughly consistent with the 7-variable mechanism, which suggests that k_{eff} should be equal to $k_6 + k_7 = 10[\mathrm{s^{-1}}] + 29[\mathrm{M^{-1}s^{-1}}]m$.

Two factors, one chemical and one geometrical, control how strongly the bromine emitted from one drop influences the oscillation of the receiving drop. In the limit of $S \ll 1$, the drops are weakly coupled. Chemically, S decreases when k_{eff} is increased. This is accomplished by increasing MA, which increases Br_2 consumption inside a drop, leaving less Br_2 to diffuse between drops. Furthermore, at high m, the Br_2 that is emitted from one drop and transported through the oil is rapidly consumed in the receiving drop upon arrival and therefore only slightly increases the Br_2 concentration in the receiving drop. Geometrically, increasing the separation of the drops weakens coupling. As transport is diffusive, this both increases the transport time and broadens the transmitted pulse, thereby reducing the diffusive transport between drops. In the limit of $S \gg 1$ the drops are strongly coupled. Decreasing MA strengthens coupling because the reaction rate k_{eff} decreases. When k_{eff} is small and S is large, bromine diffuses from the emitting drop to the receiving drop faster than the receiving drop can consume the transmitted bromine. Consequently, the concentration of bromine in the receiving drop will be significantly increased, resulting in either a phase shift in the limit cycle, or, for very strong coupling, distorting the shape of the limit cycle. Alternatively, the coupling strength can be increased by decreasing the drop

separation, which increases the inter-drop diffusive transport. We previously observed that as either MA or drop size decreases, more drops stop oscillating out of phase and enter a non-oscillatory Turing state, in which drops are maintained far from equilibrium in either the reduced or oxidized state1. This observation is consistent with theoretical work on coupled BZ oscillators, which predicts that a stationary Turing state is reached as the inhibitory coupling is increased[19, 8].

3.2.2 Phase Model for Weakly Coupled Oscillators

We now consider a second measure of the coupling strength. Drops that beat in synchrony are coupled. Experimentally and numerically we have found that for a pair of drops there are three limiting synchronous behaviors: in-phase, in which the oscillators have the same phase, anti-phase, in which the oscillators beat 180° out of phase[36] and multistable, in which multiple attractors are possible, depending on initial conditions. A natural measure of the strength of the coupling is the degree to which one drop affects the phase of its neighbor, characterized by the phase coupling function[36, 57, 58], H. The phase model is

$$\dot{\theta}_1 = \omega_0 + H(\theta_2 - \theta_1) \tag{3.1}$$

$$\dot{\theta}_2 = \omega_0 + H(\theta_1 - \theta_2) \tag{3.2}$$

as mentioned in Chapter 2 with θ_i the phase of the oscillator i, ω_0 the frequency of each oscillator when uncoupled, and H the phase coupling function. If H does not change sign, then there is only one attractor, either in-phase or anti-phase, set by the sign of the derivative of H. The number of zero crossings of H sets the number of multistable attractors (see Kuramoto[36], Eq. 5.2.18).

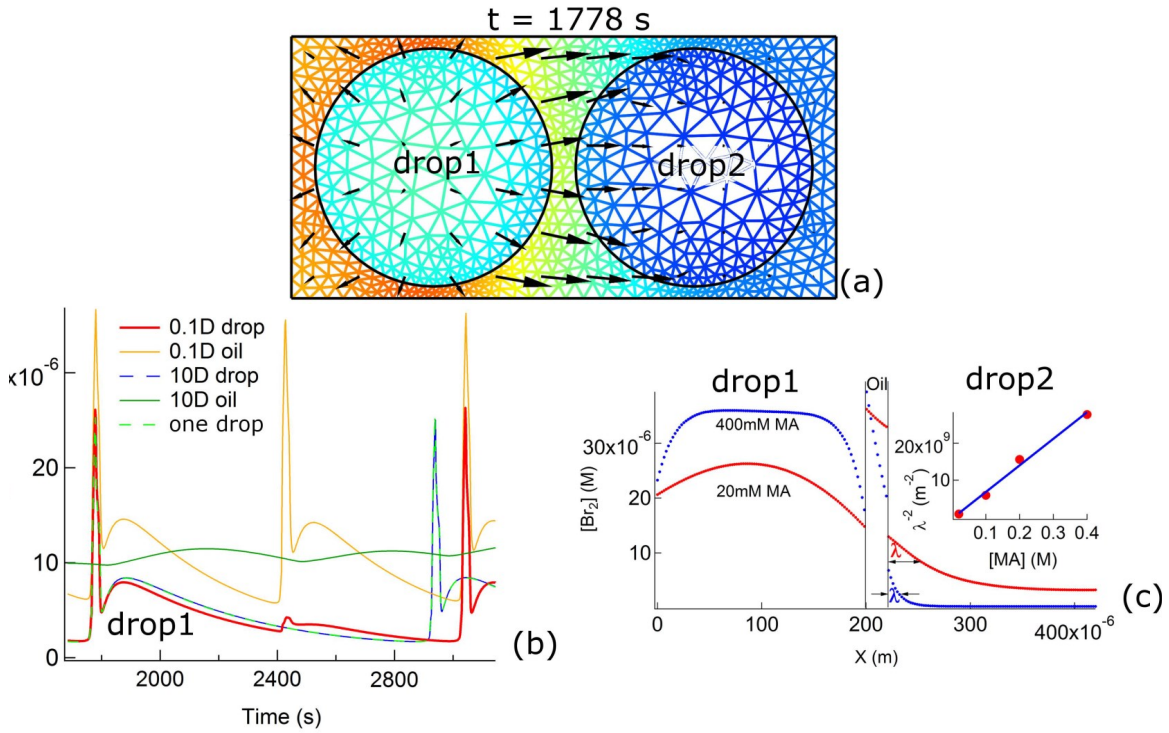

Figure 3.15: Bromine coupling. (a) Mesh used in a finite element calculation in 2D of two 200 μm drops of BZ fluid immersed in oil. The full FKN model was solved on each vertex with the following conditions: [MA] = 20 mM, 20 μm oil gap. The boundary condition at the oil/BZ interface was set by the partition coefficient, $P_{\mathrm{Br_2}} = [\mathrm{Br_2}]_{\mathrm{oil}}/[\mathrm{Br_2}]_{\mathrm{BZ}} = 2.5$, $P_{\mathrm{BrO_2\cdot}} = [\mathrm{BrO_2\cdot}]_{\mathrm{oil}}/[\mathrm{BrO_2\cdot}]_{\mathrm{BZ}} = 3$, $P_{\mathrm{HBrO_2}} = [\mathrm{HBrO_2}]_{\mathrm{oil}}/[\mathrm{HBrO_2}]_{\mathrm{BZ}} = 0$. Here the partition coefficient for $\mathrm{BrO_2\cdot}$ was set to an unphysical value 3 to test the effect of excitatory coupling in simulation. The same coupling strength can be obtained by lowering this value to 1 and using $P_{\mathrm{HBrO_2}} \approx 0.01$. A no-flux boundary condition was set at the exterior boundary. The time corresponds to 1778 s in (b). Arrows show flux of $\mathrm{Br_2}$ and color shows $[\mathrm{Br_2}]$, with orange high and blue low. (b) $[\mathrm{Br_2}]$ as a function of time in the oil between the drops at the midpoint on the symmetry axis and in the center of the leftmost drop. Two separations of drops are calculated; 2000 μm ("10D"; 10 times drop diameter) and 20 μm ("0.1D"; 0.1 of drop diameter). A single drop (one drop) in the larger geometry is also calculated. (c) $[\mathrm{Br_2}]$ as a function of distance across the simulation box of (a) for two different [MA]. Concentrations are plotted at 1778 s, just after the left drop undergoes an oxidation transition. The range (λ) that the $[\mathrm{Br_2}]$ penetrates into the neighboring drop is a measure of the coupling strength. λ is defined as the distance it takes for $[\mathrm{Br_2}]$ to drop halfway to its minimum. Decreasing [MA] increases las shown in the inset. Adapted from previous work[17].

3.2.2.1 Single Species Effect on Coupling

Before we calculate the phase coupling function, we first numerically explore the qualitative effect transmitted chemicals have on the synchronization of coupled drops. We do this by allowing only one species at a time to diffuse between drops and numerically solve our point oscillator and finite element models. The naïve expectation is that coupling through inhibitory species would lead to out-of-phase synchronization and excitatory coupling leads to in-phase synchrony. If a pair of oscillators are inhibitory coupled, then each delays the other, and their phase difference will grow to the largest possible value, 180°. Such a coupling is called "phase repulsive"[36]. By the same logic, coupling of excitatory species would lead to in-phase coupling, because each oscillator stimulates the other, shortening their phase difference, referred to as "phase attractive" coupling[36].

We consider, one at a time, transport of the inhibitory species, Br_2 and Br^-, and the excitatory species, $HBrO_2$ and $BrO_2\cdot$, in the point oscillator and finite element models. In the point oscillator model, if we allow only Br_2 to transport between drops and limit the partition coefficient $P_{Br_2} < 400$, the drops synchronize out-of-phase. While the measured value is $P_{Br_2} = 2.5$, for the sake of completeness we consider $P_{Br_2} > 400$, in which case a Turing/in-phase (depending on initial condition) mixed state is found. For the finite element model, the result is qualitatively the same, however the partition constant at which the behavior switches from out-of-phase to in-phase occurs at an 8-fold lower value, $P_{Br_2} = 50$, than in the point oscillator model. The ion Br^- is charged and therefore not expected to partition into the oil. However, again for the sake of completeness, we consider how inter-drop transport of Br^- influences synchronization. We find that in the point oscillator model, for a partition coefficient $P_{Br^-} < 0.1$, the drops synchronize out-of-phase. For larger partition coefficients the behavior first becomes bistable between out-of-phase and in-phase and then solely in-phase. The same qualitative behavior is observed for the finite element model. These two examples demonstrate that purely inhibitory coupling can lead to in-phase

synchronization, contrary to our naïve expectation, but only when the partition coefficients are unphysically high. When in-phase synchrony occurs, the drops are resetting, by which we mean that the oxidation transition of one drop induces an immediate oxidation transition in its neighbor. We note that it is possible in principle for in-phase synchrony in coupled nonlinear oscillators to occur without resetting, but we never find this in our experiments or simulations. The intuitive description is that at high inhibitory coupling strength, two drops behave as one. With only excitatory coupling (restricting transport between drops to either of the two activators, $HBrO_2$ or $BrO_2\cdot$), only in-phase synchronization is observed.

In other words, weak inhibitory coupling is phase repulsive and excitatory coupling is phase attractive. Strong coupling, whether inhibitory or excitatory, produces in-phase synchrony. The dynamical behavior of coupled drops is summarized in Fig. 3.16a. For pure Br_2 coupling, we identify the boundary between weak and strong coupling with the phase transition between out-of-phase and in-phase coupling. Using the values for the point oscillator model at the transition, $a = b = 150$ μm, $m = 200$ mM, $P_{Br_2} = 400$ and $k_{\text{eff}} = 70m[\text{s}^{-1}]$, the coupling strength $S = 0.63$; thus for this case the transition for weak to strong coupling occurs at $S \approx 0.6$.

3.2.2.2 Dynamical Phase Boundary and *S* Contour

To test further the conjecture that S is a measure of coupling strength, we calculated the phase behavior using COMSOL for two drops that are coupled solely by the diffusion of bromine through the oil. The result is plotted as a function of m and drop size for the case of oil gap equal to drop diameter and $P_{Br_2} = 2.5$, is shown in Fig. 3.16b. Superimposed are green contour lines of constant coupling strength, S. If S is a measure of coupling strength, then the boundary between the anti-phase (AP) oscillatory and stationary Turing states should occur for a constant value of S. Fig. 3.16b shows that the boundary corresponds roughly to $S \approx 0.1$, which supports the contention that the dimensionless parameter S,

governs the dynamical behavior of the coupled BZ drops.

Additionally, for the case of bromine-only coupling, we calculated the dynamical phase boundary between anti-phase and stationary Turing states as a function of drop size a and oil gap size b using COMSOL and superimposed S contours as shown in Fig. 3.16c. While the construction of the point model requires that the phase boundary is a function of $a(a+b)$, the functional form is not specified. In particular, there is no reason to suppose that the phase behavior scales as inversely proportional to $a(a+b)$, as is demonstrated in Fig. 3.16c. Furthermore, there is no such constraint on the phase boundary in the finite element models, as those equations do not have a unique form of non-dimensionalization. We interpret the results of Fig. 3.16c to mean that small drops are strongly coupled and that drop-drop coupling is relatively insensitive to drop separation. Experimental study of the dynamical behavior of drops as a function of size and separation will the subject of future work.

3.2.2.3 Phase Coupling Function *H*

Next we calculate H, the phase coupling function. Using the point oscillator model, we numerically calculate the phase coupling function (see Eqn. 5.2.17b of Kuramoto[36], or Eqn. 10.15 of Izhikevich[57]) for two identical coupled BZ drops as a function of drop diameter, drop separation, and m. We consider that the following 3 components of the Turing point oscillator model have non-zero partition coefficients; $P_{\mathrm{Br_2}} = 2.5$, $P_{\mathrm{BrO_2}} = 1$, and $P_{\mathrm{HBrO_2}} = 0.1$. The first two were estimated from experiment; the last was obtained by varying $P_{\mathrm{HBrO_2}}$ until the best fit between experimental and calculated dynamical phase diagrams was obtained. Thus $P_{\mathrm{HBrO_2}} = 0.1$ is a prediction of our point oscillator model. Using the finite element model we obtained $P_{\mathrm{HBrO_2}} = 0.01$. While there were quantitative differences between the two models, their qualitative behavior was similar.

There are two ways to calculate H. One is indirectly, as done by Kuramoto[36][57], using the phase response curve of a single drop, which in principle could be calculated from

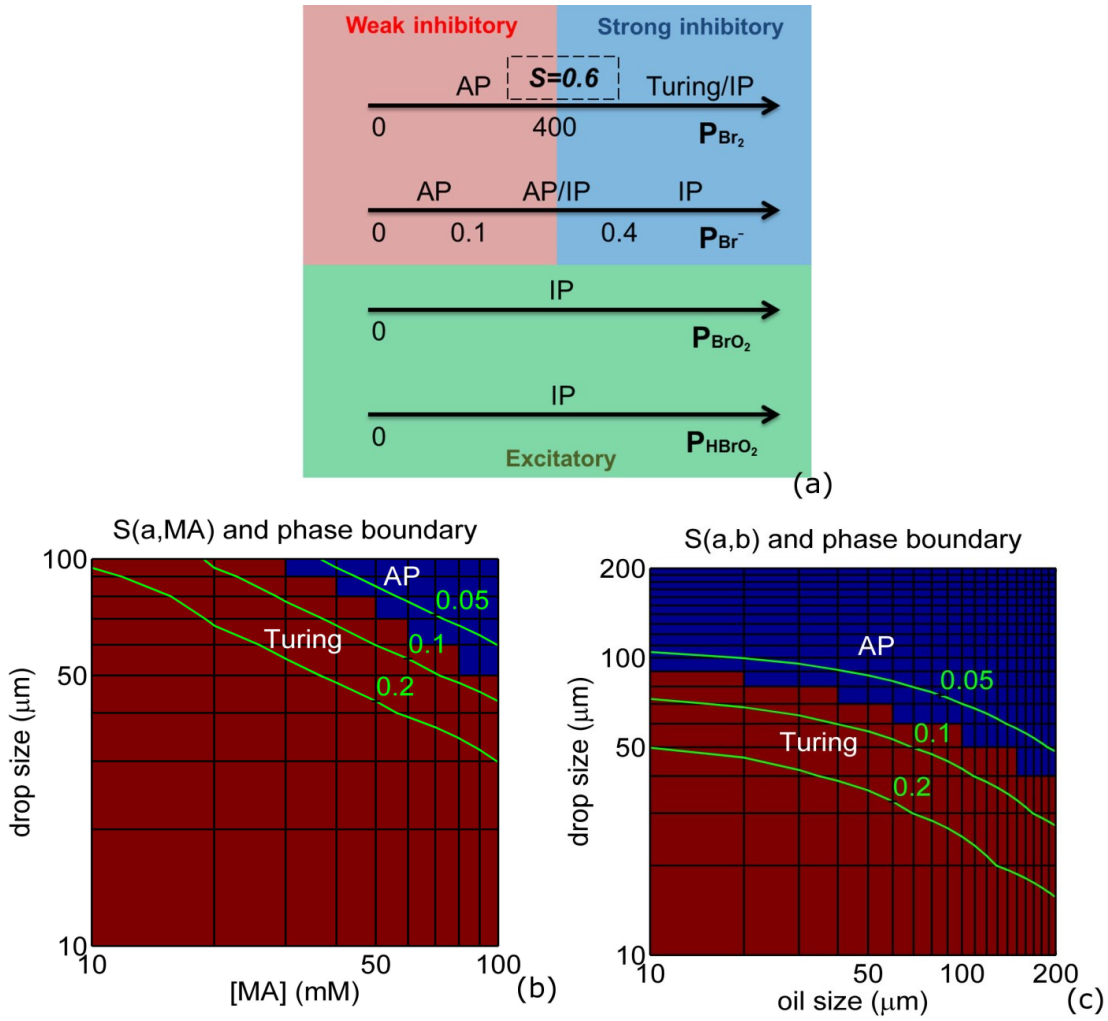

Figure 3.16: Dynamical phase boundary and coupling strength S. (a) Calculated in the point oscillator model with $a = b = 150$ μm, and [MA] = 200 mM. Only one chemical species at a time is allowed to diffuse between two drops. Four species are considered; two inhibitory and two excitatory. Phase behavior; AP; anti-phase oscillation. Turing (stationary); non-steady state. IP; in-phase oscillation. "AP/IP" indicates a multi-stable state. The results are qualitatively the same as those obtained from the finite element analysis (not shown). The partition coefficient at the phase transition is indicated for the point oscillator model. For Br_2 in the point oscillator model, the coupling strength $S = 0.6$ at the phase transition point. (b) Phase diagram as a function of drop size and malonic acid concentration (log scale) calculated using COMSOL (1D) for two BZ drops coupled through only bromine with partition coefficient 2.5 and $a = b$. The dark red region is in a stationary Turing state, while the blue region is anti-phase oscillatory. Super imposed green lines are contour lines of coupling strength S; the numbers are the values of S. (c) Similar to (b), phase diagram as a function of drop size and oil separation with [MA] = 60 mM. Adapted from previous work[17].

the point oscillator model. Instead we obtain H directly by numerically calculating the phase shift that one drop imposes on its neighbor[59] after one period. Consider two point oscillators that are uncoupled ($H = 0$) and have a constant phase shift θ. Since they are uncoupled $\dot{\theta}_i = \omega_0$. The ferroin concentration of these drops is plotted as a function of time in Fig. 3.17a (blue curves). At an arbitrary time, labeled $t = 0$ in Fig. 3.17a, we couple the two drops via the oil and plot the ferroin concentration for the coupled drops as a function of time (red curves). After one period of the uncoupled drop (τ), the phase shift of drop 1 ($\Delta\theta$), relative to its phase when uncoupled is calculated and in Fig. 3.17b is plotted as a function of θ for four different values of m. $\Delta\theta/\tau$ is equal to the phase coupling function called Γ by Kuramoto[36] in Eq. 5.2.1711 and H by Izhikevich[57] in Eq. 10.1626. We use units of phase that vary between 0 and 1. The phase shift is unambiguous, because the coupled and uncoupled drops move on the same limit cycle, $x(t)$, where x represents the 7 chemical variables in the FKN model. We numerically verified that $\Delta\theta$ is independent of the time when the two drops are coupled; for example, if the drops in Fig. 3.17a are coupled beginning at $t = 50$ s or $t = -50$ s, $\Delta\theta$ is the same as calculated for $t = 0$. In Fig. 3.17a, the time when $\Delta\theta$ is calculated is indicated as a dashed line. The value of $\Delta\theta$ is slightly less than $\Delta\theta'$, the phase difference between the expected oxidation transition for an uncoupled drop and for the same drop after it is coupled. However, $\Delta\theta'$ is notable because it is readily measurable[59]. As shown in Fig. 3.11, we measure the ferroin concentration during the entire cycle, from which it is possible in principle to extract $\Delta\theta'$. However, in practice, while numerically calculating $\Delta\theta$ is easy, experimentally it is subject to a large uncertainty. The sign of the phase shift tells whether or not the coupling is phase attractive (negative) or phase repulsive (positive). As a measure of the coupling strength, we consider the value of $\Delta\theta$ when $\theta = 0.5$, that is the phase shift, $\Delta\theta$, induced by coupling two drops whose initial phase difference is $\theta = 0.5$ or 180°. This particular choice for θ is somewhat arbitrary. Using this definition, we find that the repulsive coupling strength increases as the

drop size decreases, as the drop separation decreases, and as the malonic acid concentration decreases, consistent with our previous measure of coupling strength, S. We find that the coupling is purely repulsive for a wide range of conditions: 200mM $< m <$ 2M and drop size $a > 100$ μm, consistent with our previous observations with such drops[10]. For smaller drops or low m, bistable attractors, in-phase attractors and stationary Turing states appear. In Fig. 3.17b, for the case $m = 20$ mM, the coupling function crosses zero, rendering it bistable, with an in-phase attractor above $\theta > 0.9$ and anti-phase otherwise. The dynamical phase behavior is summarized in Fig. 3.17c.

3.2.2.4 Validity of Phase Model

We also studied the dynamics of phase coupling for a pair of droplets using the point oscillator model (Fig. 3.17d). Similar to Eqs. (10.13) to (10.17) in Izhikevich[57] and section 5.2.2 in Kuramoto[36], we define $\theta_i(t) = t/\tau + \phi_i(t)$, $i = 1, 2$ for phases of the two droplets, with the first term the phase of free-running oscillation (τ is the free-running period) and the second term the slow phase deviation induced by coupling these two droplets. In Fig. 3.17d we plot $\Delta\phi(t) = \phi_1(t) - \phi_2(t)$ as calculated from the point oscillator model and the phase model (Eqs. 3.1 and 3.2) for various initial conditions, $\Delta\phi_{t=0} = 0.1, 0.3, 0.5$. For both models the phase difference evolves from the initial condition to a steady phase deviation, $\Delta\phi_{t\to\infty} = 0.5$, corresponding to anti-phase coupling. The results for the point oscillator model give the instantaneous phase difference (dotted lines), while the phase oscillator model (solid lines) represents only the slow dynamics, as the coupling function H was obtained by averaging the coupling between drops over one period. The fact that $\Delta\phi$ corresponds for the point and phase models establishes the validity of the phase model for BZ droplets in the weak coupling limit.

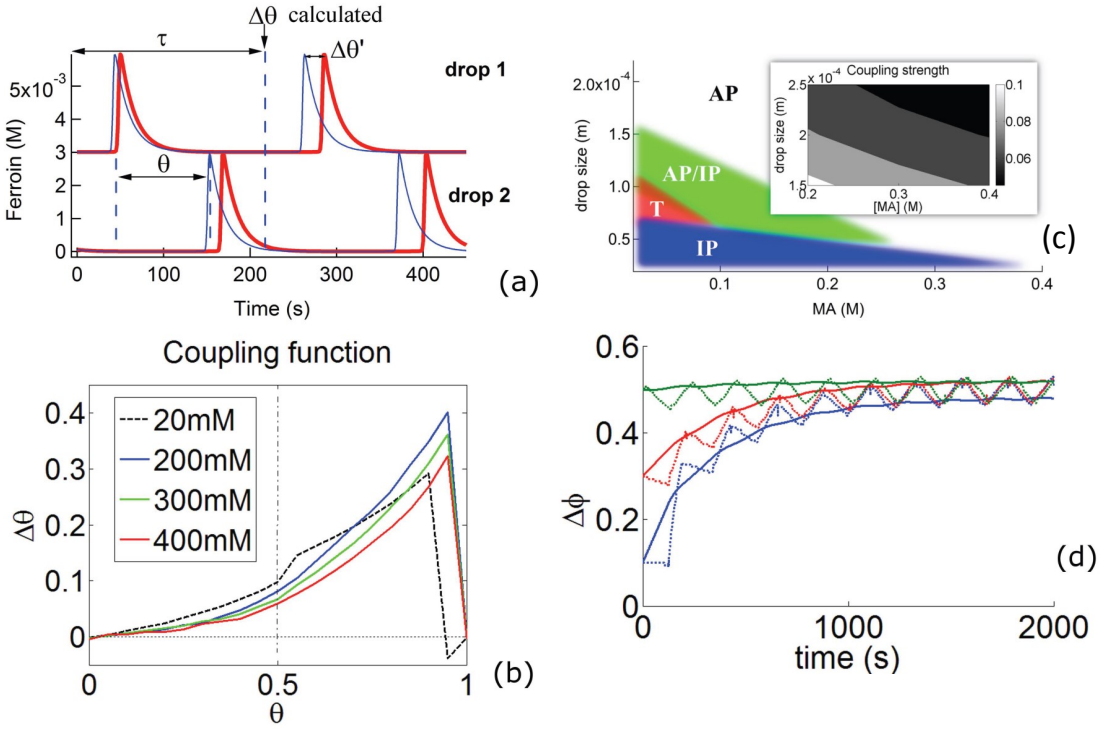

Figure 3.17: Calculated Coupling Strength. (a) Ferroin concentration vs. time calculated using the FKN point oscillator model for two drops in the out-of-phase condition. Thin blue lines: decoupled drops. Thick red lines: coupled drops. Drops are coupled at $t = 0$ and the phase shift ($\Delta\theta$) between the coupled and decoupled drops is calculated after one period (τ) of the uncoupled system as a function of the initial phase shift (θ) between the decoupled drops. Phase is normalized to 1. (b) Phase shift after one period of coupling ($\Delta\theta$) vs. initial phase shift (θ) for different values of [MA] using the point oscillator model, with $P_{\mathrm{HBrO_2}} = 0.1$, $P_{\mathrm{Br_2}} = 2.5$, $P_{\mathrm{BrO_2\cdot}} = 1$, $a = b = 150$ μm. $\Delta\theta$ increases with θ and increases as [MA] decreases. (c) Phase diagram of attractor behavior as function of drop size and [MA] with the same partition coefficients as in (b). The inset contour plot shows how the magnitude of $\Delta\theta$ for $\theta = \pi$ varies as a function of [MA] and drop size. IP: in-phase synchronization. AP/IP: bistability. T: stationary Turing state, in which some drops stop oscillating. (d) Dynamics of the phase difference between two oscillators ($\Delta\phi$) calculated with the point oscillator (dotted curves) and phase (solid curves) models using [MA] = 600 mM and the same geometry and partition coefficients as in (b). $\Delta\phi_{t=0} = 0.1, 0.3, 0.5$ for the blue, red, and green curves, respectively. Phase varies between 0 and 1. Adapted from previous work[17].

Chapter 4

Turing Morphogenesis and more

Too little liberty brings stagnation and too much brings chaos.

Bertrand Russell

The *Chemical Basis of Morphogenesis*, written in 1952 by Alan Turing[1], described how in circular arrays of identical biological cells and continuous rings of tissue diffusion can interact with chemical reactions to generate up to six spatial-temporal periodic chemical structures. After 60 years the Turing mechanism remains controversial in biology because of uncertainty in both the reaction kinetics[60, 18] and transport mechanisms[61]. In chemistry, all six Turing patterns have been established in continuous systems on the centimeter scale[7, 8], but not for diffusively coupled cells on the micron scale. Here we report an experimental reaction-diffusion system ideally suited for testing Turing's ideas in synthetic "cells" consisting of microfluidically produced surfactant-stabilized emulsions[9, 10] in which droplets containing the Belousov-Zhabotinsky oscillatory chemical reactants[11] are dispersed in oil. In contrast to biology, here the chemistry is understood, rate constants are measured and interdrop coupling is purely diffusive. We explore a large set of parameters through control of rate constants, drop size, spacing, and spatial arrangement of the drops in lines

and rings in one-dimension and hexagonal arrays in two-dimensions. In 1D we observe five distinct spatial-temporal patterns that emerge as a result of intercell coupling and establish all arise as predicted by Turing, although altered by nonlinearity. In 2D an additional pattern is observed, which is incompatible with Turing's analysis, for which we develop a non-linear dynamics theory. The Turing model is regarded as a metaphor for morphogenesis in biology; useful for a conceptual framework and to guide modeling, but not for prediction[62]. Here, we develop a quantitative and falsifiable reaction-diffusion model that we experimentally test with synthetic cells. We quantitatively establish the extent to which the Turing model in 1D describes both stationary pattern formation and temporal synchronization of chemical oscillators via reaction-diffusion and in 2D demonstrate that chemical morphogenesis drives physical differentiation in synthetic cells.

4.1 Establishing the Turing mechanism using BZ drops

Turing's linear stability analysis (LSA) for morphogenesis predicts that in an isolated ring of cells, as few as two morphogens, are sufficient for stationary pattern formation[1, 63] and synchronization of oscillating cells, while at least three are needed for traveling waves. Turing characterized this system as "mathematically convenient, though biologically unusual[1]". Although no examples of rings of living cells have been found, it is hard to overemphasize the impact Turing's model has had on developmental biology[40, 64, 65, 18, 62, 66].

4.1.1 Testing Turing Mechanism

To construct a tractable model Turing treated cells as geometric points and considered the membranes separating cells as chemically specific barriers to diffusion, ignoring any chemical reaction or accumulation of chemicals in the membrane. Turing's resulting reaction-diffusion model consists of rings of point cells diffusively connected directly to nearest neighbors,

expressed as a set of equations each of the form[1]

$$\frac{d\boldsymbol{c}_i}{dt} = \boldsymbol{F_c}(\boldsymbol{c}_i) + \boldsymbol{M_c}\left(\boldsymbol{c}_{i-1} + \boldsymbol{c}_{i+1} - 2\boldsymbol{c}_i\right) \tag{4.1}$$

where $\boldsymbol{c}_i$ is a vector containing the concentrations of the chemical species in the i^{th} cell, $\boldsymbol{F_c}$ is a vector function describing the chemical kinetics of the c-species, and $\boldsymbol{M_c}$ is a diagonal matrix containing the coefficients of diffusive transport (μ_c) of the c-species from drop to drop. To describe the BZ chemistry we use a model developed by Vanag and Epstein[33, 34] (VE model) that considers four chemical concentrations to vary in time: the inhibitory components bromine (Br_2) and bromide (Br^-), the oxidized form of the catalyst (ferriin), and the activator bromous acid ($HBrO_2$). Turing did not specify how the coupling strength μ_c varies with the physical-chemical parameters and different results arise depending on the assumptions used to produce a geometric point model [67, 34]; we extend the Turing model by explicitly calculating the coupling strength

$$\mu_c = f\frac{2D_cP_c\left(b+d\right)}{d^2\left(a+b\right)}\left(\ln\left(\frac{b+d}{b}\right) + \frac{a-d}{b+d}\ln\left(\frac{a-d}{a}\right)\right) \tag{4.2}$$

(see Supporting Information in previous work[15] for derivation), where D_c and P_c are the diffusion and partition coefficients of the c-species in the oil, a is the length of the BZ drop, b is the oil gap separating drops, d is the diameter of the capillary, and f is a fitting parameter, used to minimize the difference between experiment and theory. The only unknown parameter in Eqn. (4.2) is the partition coefficient of $HBrO_2$, P_x. The four VE reaction equations, F_c, contain the aforementioned 4 variable chemical species, 4 more chemicals, whose concentrations are set initially and are approximated as constants in the model, and 9 known rate constants.

To elucidate this model, Turing[1] used linear stability analysis (LSA) and identified six possible chemical structures in rings of diffusively coupled identical cells. In LSA, one

characterizes how the steady state concentrations, i.e. those for which $dc_i/dt = 0$, respond to small perturbations. If all perturbations decay, then the system is in a stable steady state. However, if some perturbations grow with time, the steady state is unstable, and the fastest growing perturbation is labeled a Turing instability. For a ring of N cells Turing proved that the requirement of periodicity restricts dimensionless wavevectors of the perturbations to take on one of three possible values; $q_{\min} = 0$, $q_{\max} = 2\pi s_{\max}/N$, where for even numbered rings $s_{\max} = N/2$ and for odd rings $s_{\max} = (N-1)/2$ and $q = 2\pi s/N$ where the integer s ranges from $1 < s < s_{\max}$. For each possible q, the perturbation growth can be either oscillatory ($\omega > 0$), or non-oscillatory ($\omega = 0$), giving a total of six possible instabilities. Following Turing's nomenclature, the six instabilities (*a*-*f*) are each characterized by a wavevector and frequency, (q,ω), as follows: Turing case (*a*), ($q_{\min}$, 0); (*b*), ($q_{\min}$, ω); (*c*), ($q_{\max}$, 0); (*d*), (q, 0); (*e*), (q, ω); and (*f*), ($q_{\max}$, ω). See Supporting Information in previous work[15] for more mathematical details.

The Turing model incorporates three significant and untested theoretical approximations; considering each cell as a point, simplification of chemical transport by elimination of explicit consideration of the oil, and linearization of the BZ chemistry. To what degree does this highly idealized model describe experiments on synthetic cells? Specific questions we answer with experiment include: (*i*) How well does the simplified coupling term agree with experiment? (*ii*) Are there more or less than the six predicted Turing states? (*iii*) How are the linear states modified by non-linearities? (*iv*) Does the Turing model provide quantitative and predictive understanding of experiment? (*v*) How do states depend on dimensionality? (*vi*) Do cells undergo physical morphogenesis?

To test the Turing model in discrete cells we produced 1D linear and 2D hexagonal arrays of drops by filling cylindrical and rectangular capillaries, respectively. Circular rings of drops were created by adding the photosensitive catalyst ruthenium-*tris*(2,2'-bipyridyl) (Rubpy) to the BZ mix, which has the effect that, as long as blue light is shone on the drops, they are

held in the reduced steady state. Therefore, light can be used to create constant chemical boundary conditions for networks of non-illuminated drops. We use a computer projector coupled to a light microscope to generate patterned illumination[10] and isolate either pairs of drops, or a ring of active drops from a 2D array as shown in Figures 4.1. A second light source at the ferroin absorbance wavelength is used to observe, but not affect, the BZ reaction. Space-time plots are generated by plotting the intensity of a single line of pixels connecting the centers of adjacent drops as a function of time. Viewed in transmission, the oxidized state appears bright, while the reduced state appears dark.

We prepared a series of 1D arrays of drops in rings and lines and determined the long term emergent chemical states as a function of the two variables that most strongly control interdrop behavior; malonic acid concentration and coupling strength. Coupling strength, μ_c, is conveniently tuned experimentally by varying the drop size a and oil gap b using microfluidics. In Figures 4.1 we illustrate examples of six distinct states and identify five of them as coupling-induced emergent Turing states, Figures 4.1(b-f). The sixth state, found for malonic acid concentrations below 1 mM, Figures 4.1(a), has the same pattern as Turing state (a), however, theory predicts that this is a stationary, non-emergent stable state, underscoring the point that observation of a chemical state with the same pattern as a Turing state is not sufficient evidence that the state arises from a Turing mechanism[64, 60, 18]. Only the pattern with the symmetry of Turing case (b) is observed in a region of parameter space not predicted by theory.

The behavior of finite rings depends the number of drops, N, in the ring as seen in Figures 4.1g, h for two rings with identical chemical composition, drop size and spacing, but with 5 and 6 drops, respectively. For these particular chemical conditions, LSA predicts a Turing state (f) characterized by the wavevector-frequency pair $(q_{\max}, \omega)$, as defined previously. Turing's prediction is that for N odd no two drops will oscillate at the same time; there will be N beats per measure, while for N even there will be two beats per measure. For a

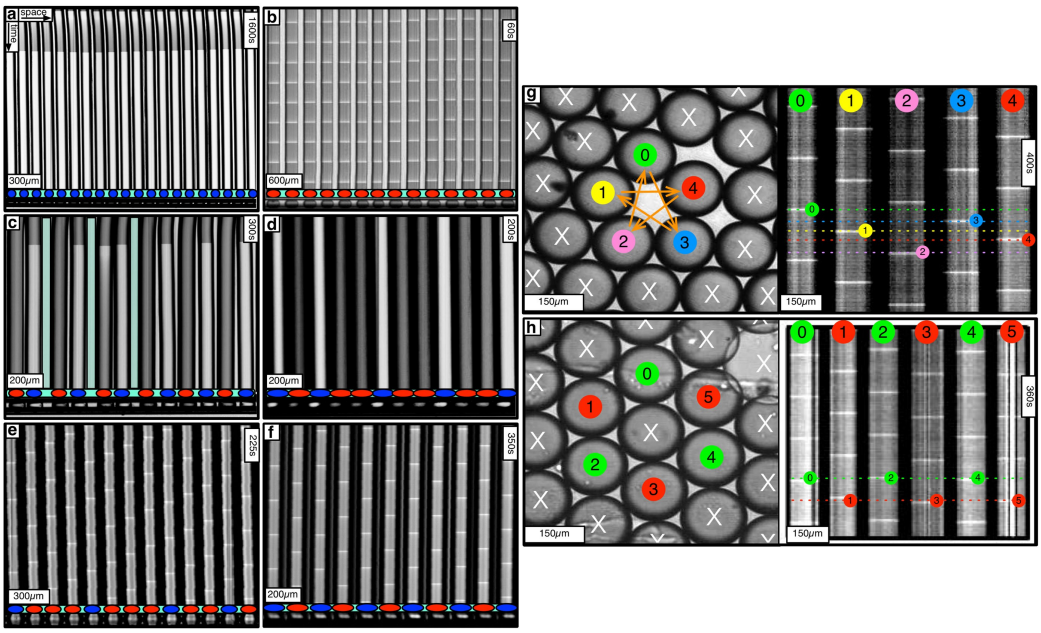

Figure 4.1: Chemical states of linear and circular arrays of BZ drops. (a-f) 1D linear arrays. Top: space-time plot demonstrating Turing state, Bottom: corresponding cartoon. Cartoon colors: Blue, BZ drops in reduced state; Red, oxidized state; Cyan, oil. Five of the six Turing solutions *b*-*f* are observed and labeled as in Turing's paper[1]. (a) Stationary stable oxidized state after initial transient; 10 mM MA, no NaBr, drop size 130 μm, and oil gap 20 μm. (b) Turing case *b*, (long-wavelength, oscillatory), ($q_{\min}$, ω); 2.4 M MA, 10 mM NaBr, drop size $\sim$230 μm, and oil gap $\sim$100 μm. (c) Turing case *c*, (short-wavelength, stationary), ($q_{\max}$, 0); 20 mM MA, no NaBr, drop size $\sim$98 μm, and variable oil gap between 0 μm and 47 μm. (d) Turing case *d*, (intermediate-wavelength, stationary), (q, 0); 40 mM MA, no NaBr, drop size 95 μm, and oil gap $\sim$0 μm (touching drops). (e) Turing case *e*, (intermediate-wavelength, oscillatory), (q, ω); 640 mM MA, 10 mM NaBr, drop size 117μm, and oil gap 3μm. (f) Turing case *f*, (short-wavelength, oscillatory), ($q_{\max}$, ω); 380 mM MA, 10 mM NaBr, drop size 106μm, and oil gap 25μm. (g-h) Odd and even circular arrays. Turing case *f*. Left: oscillatory drops are labelled; all other drops are illuminated with light (cross) and held non-oscillatory in the reduced state, Right: space-time plot. 640 mM MA, and drop size is $\sim$150 μm. (g) Five membered ring. Drops oscillate in a pentagramal pattern. (h) Six membered ring. Neighboring drops are π radians out-of-phase. Adapted from previous work[15].

ring of five drops, LSA predicts a waveform $C_5(r,t) \propto \exp(i(4\pi r/5 - \omega t))$, with $0 \leq r \leq 4$ the drop number. In this expression, the phase is chosen such that a drop is oxidized when $4\pi r/5 - \omega t$ is equal to an even multiple of 2π. As time advances in increments of one fifth of a period, the oxidized state in Figures 4.1g moves along the ring in a pentagramal sequence from drops $0 \to 3 \to 1 \to 4 \to 2$. For the ring of 6 drops, $C_6(r,t) \propto \exp(i(\pi r - \omega t))$, with $0 \leq r \leq 5$. As shown in Figures 4.1h, all even numbered drops oxidize simultaneously at the beginning of a period and half a period later all odd numbered drops oxidize.

Using published chemical rate constants of the VE model[33] we calculate two state diagrams, one using Turing's linear stability analysis (LSA) and the other the full non-linear simulation (NLS) of Eqn 4.1 in one-dimension; these two theories are compared with experiment in Figure 4.2. In order to assign coupling strengths to experiment, we again treat f in Eqn. 4.2 as a fitting parameter, but now also fit the partition coefficient of the activator, P_x. The best agreement between the NLS and experiment was obtained for $P_x = 0.05$ and $f = 0.14$. With respect to the experimental state diagram, the NLS overestimates coupling strength 8-fold. Both state diagrams predict that as coupling strength increases above zero the same five Turing instabilities (*b-f*) appear with three oscillatory (green hues) and two non-oscillatory (red hues). For 1D arrays of drops in capillaries, the linear and non-linear theories predict the same basic features, with two notable distinctions. First, non-linearity strongly suppresses the stationary states. Second, "cluster" states, distinctive oscillating patterns consistent with Turing case (*e*) were experimentally sought and observed only after calculations of the state diagram indicated their existence; thus the Turing model is predictive. Below 1 mM malonic acid both theories predict the system is in a stationary and uniform oxidized state, independent of coupling strength, shown as a thin, grey vertical bar. Were this to arise as an instability, it would correspond to the sixth Turing state (*a*). At low malonic acid and moderate coupling strength, both theories predict temporally stationary, spatially non-uniform Turing states *c,d*, however, the non-linear stationary states

vanish for low coupling strength and the realm of non-linear stationary states is reduced to lower malonic acid values compared with the linear analysis. Evidently, nonlinearity favors oscillatory over stationary Turing states. Both theories predict a sharp transition between oscillatory and stationary states with experiment closely following the boundary predicted by the non-linear model. Both the LSA and NLS models predict a broad range of wavelengths for both oscillatory and stationary states, which again is borne out by experiment. The temporally oscillatory, 4-drop wavelength Turing state (e) consisting of a pattern of four drops with the following sequential pattern; oscillatory with phase 0, stationary, oscillatory with phase π, stationary, referred to as 0sπs is consistent with LSA, but a 4-drop "cluster" state with a sequential pattern of two drops oscillating in phase followed by two drops oscillating 180 degrees out of phase, $00\pi\pi$ is inconsistent with LSA. In the NLS model both the $00\pi\pi$ and 0sπs states occur only at high coupling strength. These states were experimentally sought and observed only after calculations of the state diagram indicated their existence. Prior to the non-linear solution of equation 4.1 there were no experimental indications that such patterns occurred; thus the Turing model is predictive.

To investigate the effect of dimensionality on Turing states, we performed experiments on closed packed hexagonal arrays of drops, reported as squares in Figure 4.2. We observed a state involving units of 3 drops arranged in a triangle that is not predicted by LSA or NLS models, shown in Figure 4.3, in which one drop is stationary and the other two oscillate with a phase difference of π, referred to as the $s0\pi$ state[9, 15]. Linear stability analysis requires all drops to share the same temporal behavior, i.e. all stationary, or all oscillatory, thus the $s0\pi$ state cannot arise as a linear instability. However, it could be a nonlinear effect, but extensive numerical exploration of the full nonlinear chemistry using both the Turing and finite element models on ordered hexagonal arrays failed to produce the $s0\pi$ state with homogeneous drops. The qualitative discrepancy between theory and experiment suggests that a critical element is missing from the Turing model. Therefore, we developed a hy-

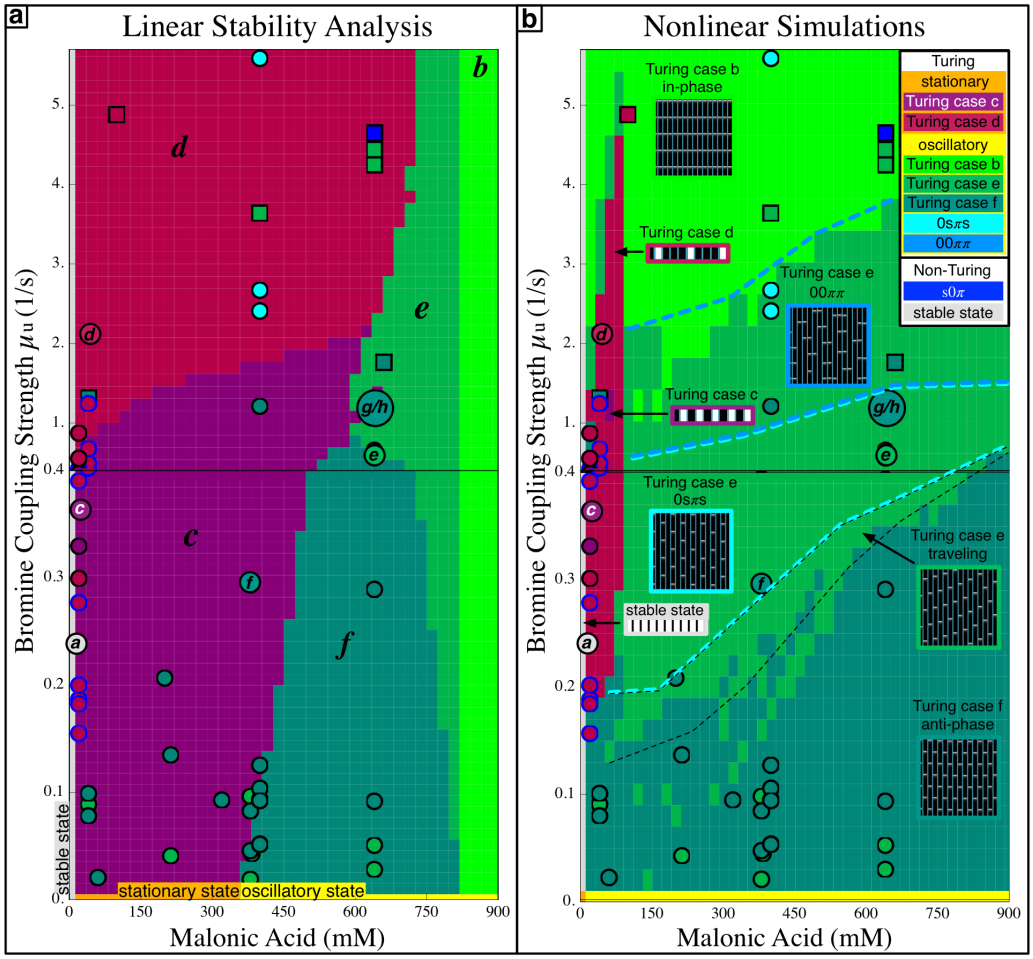

Figure 4.2: Linear Stability Analysis (LSA) and Non-Linear Simulations (NLS) of the Vanag-Epstein model of BZ, as a function of coupling strength and malonic acid concentration. Note the scale change on the vertical axis at $\mu_u = 0.4$. In all figures the colors are as indicated in the key. The data is plotted with circles for 1D experiments and squares for 2D experiments. The data points with a letter in the center are included in Figure 4.1. Space-time plots of oscillatory states are inset in square areas; stationary states are inset in rectangular areas. The dashed boundaries within the region of Turing state e of the NLN diagram indicates location of traveling waves, the 0sπs state, and the 00$\pi\pi$ clusters. Drops do not synchronize below the dash-dot line. All experimental data points are plotted according to the definitions of μ given in the text with $f = 0.14$ and $\mu_u = 50\mu_x$. Adapted from previous work[15].

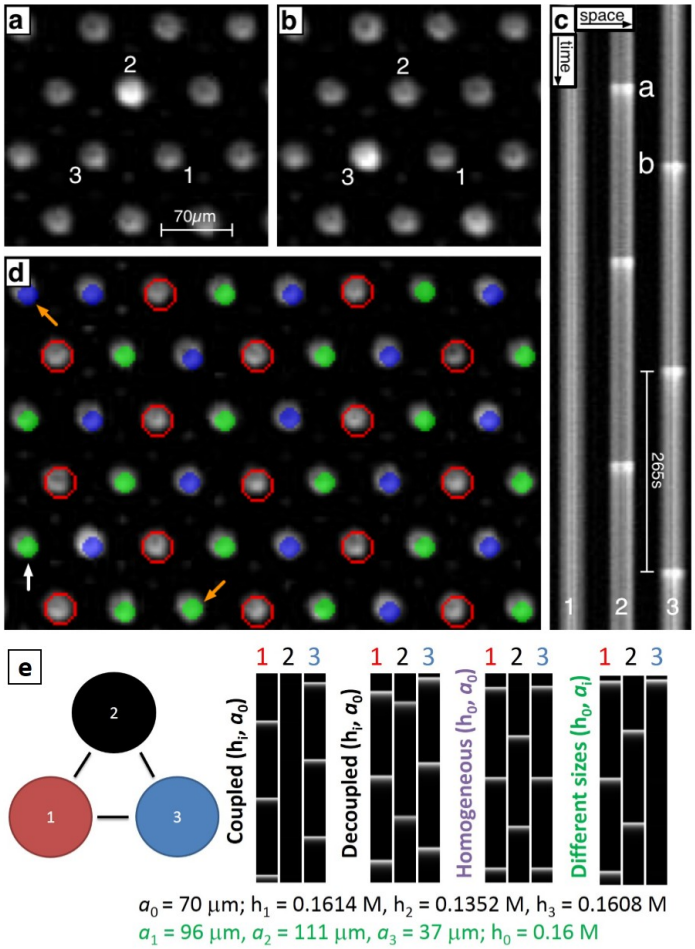

Figure 4.3: Observations of 2D arrays of $s0\pi$ states. a-b) Single frames demonstrating the $s0\pi$ state. The frames correspond to the first two oxidation transitions, labeled a and b in c). c) Space-time plot of drops 1-2-3 shown in a) and b). Drop 1 is stationary while drops 2-3 remain oscillatory with a phase difference of π. d) A combined image where the stationary drops are outlined in red and the oscillatory drops are color coded by their phase difference, $\phi_i = \theta_i - \theta_{\text{ref}}$, where $0 \leq \phi \leq \pi$ and θ_{ref} is the phase of the drop indicated with the white vertical arrow. Drops where $\phi_i < \pi/2$ are green and $\phi_i > \pi/2$ are blue. Notice that every third drop is stationary and every oscillatory drop is out of phase with its immediate neighbors, two exceptions noted with orange arrows. Chemical conditions: 300 mM bromate, 3 mM ferroin, 0.4 mM Rubpy, 80 mM acid, 640 mM MA, and 10 mM NaBr. Drop size is $\sim 70\mu$m. e) Point model simulation of three drops with various heterogeneity. Adapted from previous work[15].

pothesis for the $s0\pi$ state that requires additional conditions to the Turing model; the drops must be physically or chemically heterogeneous with two drops being "stronger" oscillators that synchronize out-of-phase when isolated. In Figure 4.3e we demonstrate numerically that the $s0\pi$ state appears once the heterogeneity between drops is large enough. Experimentally, we do not have evidence of drop heterogenity of the magnitude required by our simplified theory; therefore the $s0\pi$ state bears more scrutiny and will be further discussed in section 4.2.3.3. In general, the experimental state diagram for two-dimensional arrays of drops deviated significantly from the one-dimensional non-linear calculation, indicating that dimensionality plays a significant role in pattern selection.

4.2 Two-Dimensional patterns

4.2.1 Introduction

In this section we examine 2D arrays of drops in more detail through experiments and finite element simulations. We describe the transition from oscillatory to stationary chemical states with increasing coupling strength, as well as the trend that the ratio of stationary oxidized to stationary reduced drops increases with coupling strength. We also provide simulation results to address a previously unresolved question[15], quantifying the degree of chemical heterogeneity of BZ drops sufficient to generate mixed oscillatory and stationary patterns.

4.2.2 Methods

Rectangle glass capillaries (VitroTubes^{TM}) were directly used for 2D emulsion storage without further treatment. The capillaries were either 50, 100 or 200 μm in height, chosen to be somewhat smaller than the droplet diameter such that the emulsion would spontaneously form a monolayer. The capillary widths were either 10 or 20 times the height and the capillary

lengths ranged between 2 to 4 cm. Such a capillary filled with BZ emulsion can be effectively treated as a 2D system whose height is much smaller than the other two dimensions. Inside the capillary, monodispersed micro-droplets stabilized by the surfactant spontaneously form a close-packed hexagonal lattice so that the system is at the highest packing density. The aqueous drops have a much lower mass density that does the fluorinated oil and float to the top of the chamber. The capillaries were positioned so that the normal of the plane defined by the capillary height and length was oriented parallel to gravity.

Detailed descriptions of chemical preparation and our home-made optical system for illumination and data recording can be found in Chapter 2. Our BZ mixture in droplets consisted of the following: $[H_2SO_4]$ = 80 mM, [NaBr] = 10 mM, $[NaBrO_3]$ = 300 mM, [Ferroin] = 3 mM, $[Ru(bipy)_3]$ = 0.4 mM, both metal catalysts were in reduced form. This recipe was used in our experiments with various malonic acid concentrations, [MA], or m for short, which was the only tunable parameter in our BZ chemistry.

The theoretical model used in this paper for the BZ reaction chemistry is identical to the one in previous works[17, 10], which is the well established 7-variable FKN model[30, 31] with minor modifications[33, 34]. Coupling from one drop to another through the intervening oil was realized in the model by allowing up to three chemical species to partition into the oil with an appropriate permeation constant. No chemical reactions were considered to occur in the oil phase and the chemical species in the oil moved according to Fick's laws of diffusion. The 2D reaction-diffusion equation was solved using the finite element solver COMSOL multiphysics®. Periodic boundary conditions were used with different numbers of drops in the unit cell. The three species which were allowed to partition into the oil phase were the nonpolar species bromine (Br_2), which acts as the sole inhibitor, and the radical $BrO_2\cdot$ and weakly polar bromous acid $HBrO_2$, both of which act as activators. The fluorinated HFE oil we used is almost apolar, thus an apolar molecule partitions preferably into the oil phase rather than the aqueous phase. The partition coefficients, the ratio of concentration in the

oil phase to the aqueous phase at the oil/water interface, used in the simulation are: $P_{\mathrm{B}} = 2.5$ for bromine, $P_{\mathrm{R}} = 1$ for the radical, and $P_{\mathrm{H}} = 0.01$ for bromous acid.

In order to explore which of the species is most important for coupling, simulations with various combinations of coupling species including bromine only coupling ($P_{\mathrm{B}} = 2.5$, $P_{\mathrm{R}} = P_{\mathrm{H}} = 0$), bromine and radical coupling ($P_{\mathrm{B}} = 2.5$, $P_{\mathrm{R}} = 1$, $P_{\mathrm{H}} = 0$), as well as coupling with all three species were performed for a wide range of values of two parameters which controlled coupling strength; malonic acid concentration (m) and drop diameter (a).

The purpose of introducing the concept of coupling strength between BZ droplets is to develop a qualitative and quantitative understanding of the physical and chemical factors that control synchronization of BZ drops. For example, one experiment that can be used to define coupling strength is to consider two drops which initially begin to oscillate with a phase difference that is different than their steady state phase difference and measure the time it takes to reach steady state[15]. The inverse of this time is the synchronization rate, which is considered to be a measure of coupling strength. For BZ emulsions the synchronization rate increases as either the drop size or separation is decreased leading to the conclusion that coupling strength increases as drop size or separation decreases. A second measure of coupling strength is the transition between two chemical dynamic states. For example, for one set of chemical conditions an array of drops separated by a great interdrop distance may all be oscillating, but as the separation between the drops is decreased, the array of drops turn stationary. Since the diffusive interdrop transport of chemicals increases with decreasing separation, we consider that the transition from an oscillatory to stationary chemical state serves as a measure of the transition from weak to strong coupling.

Previous studies identified bromine as the dominant chemical species which diffuses between drops[19]. Bromine itself functions as a communicator of inhibition and not the inhibitor itself in the following fashion. Bromine, being apolar, readily partitions from the BZ solution into the oil phase. Once inside a neighboring drop, bromine reacts with malonic acid

to form bromo-malonic acid and bromide, the latter of which acts as an inhibitor in the BZ reaction, serving to hold the system in the reduced state. Because bromide is charged, it is insoluble in the oil. If the malonic acid concentration is high, then adding bromine has little effect on the chemical dynamics for two reasons. First, high malonic acid concentration leads to high Br_2 consumption inside a drop, leaving less Br_2 to diffuse between drops. Second, at high malonic acid concentration, the Br_2 that is emitted from one drop and transported through the oil is rapidly consumed in the receiving drop upon arrival and therefore only slightly increases the Br_2 concentration in the receiving drop[17].

One heuristic measure of the coupling strength between drops in contact is the dimensionless number $S = \alpha P_{\mathrm{B}} D/(a^2 k_{\mathrm{eff}}) = \mu/k_{\mathrm{eff}}$, which is the ratio of two rates: $\mu = \alpha P_{\mathrm{B}} D/a^2$, the rate of diffusive transport between BZ drops of the inhibitor bromine in the limit of a small oil gap[15], and k_{eff}, the effective rate constant characterizing the consumption of Br_2, which occurs *via* bromination of malonic acid[17]. Our previous numerical studies suggest that $k_{\mathrm{eff}} \propto m$[17]. Here P_{B} is the partition coefficient of bromine, D is the diffusion coefficient of bromine, a is the BZ droplet size and α is a numeric factor of order 10 for drops whose surfaces are separated by a surfactant layer of thickness $10^{-4}a$. The derivation of μ is presented elsewhere[15]. The dimensionless ratio of reaction rate to diffusive rate is known as the Damköhler number (Da), used in chemical engineering to assess the degree of conversion in a continuous stirred-tank reactor, while S is the inverse. Large coupling strength corresponds to $S \gg 1$ and occurs when the drops are small and/or the malonic acid concentration is low. When the coupling strength is large, more bromine is transferred between drops than can be consumed and therefore the chemical concentration of each drop is influenced by the other. On the other hand, when the coupling is weak, the amount of bromine transferred is small enough to be rapidly consumed and thus the drops are insensitive to each other's presence[17].

4.2.3 Results

4.2.3.1 Tunable diffusive lateral inhibition

We borrow the term "lateral inhibition" from biology to describe the effect of interdrop diffusion of bromine on the oscillation of BZ droplets. In the BZ reaction, the oxidized state is the result of an autocatalytic process and can be considered the "active" state, while the reduced state can be considered "inhibited". In the stationary state, a pair of initially identical drops spontaneously differentiates chemically to a state in which one is oxidized and produces the inhibitor bromine and the other is reduced and absorbs the bromine.

Drop diameter a and malonic concentration m are the two parameters we tune to change coupling strength. Fig. 4.4a is an experimental state diagram of oscillation patterns for a monolayer of monodispersed BZ droplets closed packed in a hexagonal array, as a function of drop diameters at a constant malonic acid concentration of 640 mM. The unit cell of the hexagonal array consists of three drops. The diagram shows the fraction of droplets in one of three states; the oscillating state shown in green (Osc) or one of two possible stationary states as a function of droplet diameter. Stationary states are either in the oxidized stationary Turing state, shown in blue (OST) or the reduced stationary Turing state, shown in red (RST). Each vertical bar shown in Fig. 4.4a as proportionally colored bars in green (Osc), blue (OST) and red (RST) represents one experiment with several hundreds of identically sized droplets. For a given experiment, only the drops with six nearest neighbors were counted, hence those drops at system boundaries or at lattice defects were omitted. The fraction of drops in each stationary state was normalized by the total number of drops counted in each experiment.

Region III of Fig. 4.4a represents experiments with large drop diameters where the interdrop diffusive coupling is weakest. A series of monodisperse drop arrays were studied in the range 100$\sim$450 μm, although only those with diameter less than 150 μm are shown

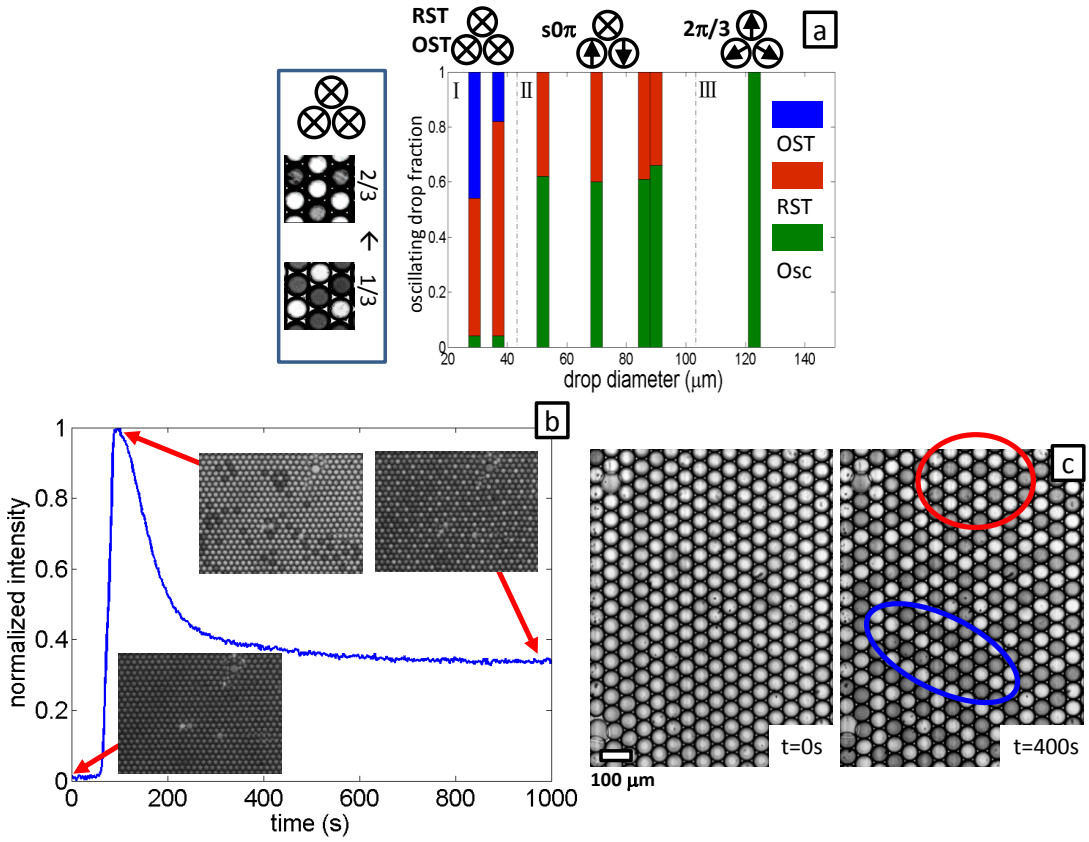

Figure 4.4: Observed chemical states in 2D hexagonal lattices of BZ drops as a function of drop diameter and malonic acid concentration. a) Patterns as a function of droplet diameter a, with $m = 640$ mM. The unit cell has three drops. Arrows denote oscillating drops. The angle between arrows is equal to the phase shift between oscillating drops. The "x" denotes a stationary drop. *Inset*: Stationary pattern with 2/3 drops oxidized, in comparison to a stationary pattern with 1/3 drops oxidized. b) Stationary Turing pattern with $m = 600$ mM and $a = 50$ μm. The normalized intensity of the drops was plotted as a function of time. c) Stationary Turing pattern with $m = 200$ mM and $a = 50$ μm. The pattern at the moment when all drops first oxidize simultaneously (arbitrarily labeled as $t = 0$) and the stable pattern, 400 seconds later, are shown side by side.

in Fig. 4.4a. In region III, all of the drops are oscillating, exhibiting the $2\pi/3$ pattern[9] where each of the three drops in a unit cell oscillate 120 degrees out of phase with each other. This pattern is represented by an icon of 3 circles in a triangle with the arrows' directions indicating the evenly separated phase of the oscillating drops. In region II, corresponding to drops of 50$\sim$100 μm diameter, approximately 2/3 of the drops are oscillating and 1/3 are in the reduced stationary Turing state, in a pattern denoted $s0\pi$[15] where the nomenclature describes the state of the three drops; one of the three drops in a unit cell is stationary (s), and the other two are oscillating π radians with respect to each other (0π). Parenthetically, we note that in another instance we referred to this same pattern as the π-s state[9]. In several figures this pattern is represented by a triangle of three circles with two arrows in opposite directions representing the 180 degree phase shift between oscillating drops and one with an X representing the one stationary drop.

Next we report a new phenomenon shown in region I, which is that for even smaller drops, corresponding to stronger coupling strength, almost all the drops enter stationary Turing states and that the fraction of stationary oxidized drops increases as the drop size is decreased. In region I of Fig. 4.4a, corresponding to drops of high malonic concentration ($m = 640$ mM) and less than 50 μm diameter, most of the drops do not oscillate. Data with two drop sizes were shown in this range. At 40 μm about 20% were in the oxidized stationary state and about 80% of the drops were in the reduced stationary state. At 30 μm almost 50% of the drops were oxidized stationary and 50% were reduced stationary. As the diffusive bromine inhibition strength between drops increases with decreasing droplet diameter, we hypothesize that stronger inhibitory coupling leads to a larger fraction of stationary oxidized drops.

Figs. 4.4b and 4.4c lend further credence to our hypothesis that bromine coupling strength controls the fraction of oxidized to reduced stationary drops. Here we compare arrays of drops with similar droplet diameter ($\sim$50 μm) and very different malonic concen-

trations (600 mM for Fig. 4.4b and 200 mM for Fig. 4.4c). The vast majority of drops in both Figs. 4.4b and 4.4c were in the stationary Turing state and resembled the samples shown in region I of Fig. 4.4a.

Fig. 4.4b shows the normalized intensity of more than a thousand droplets as a function of time. Photographs of a small portion of the full field of view were taken at different times. At the very beginning of the experiment, t = 0, all drops were near the reduced state (i.e. process A in the FKN mechanism, see Chapter 2) and hence the intensity of the full field of view was the darkest in the whole experiment. This is a consequence of how the samples were prepared. The drops were created with 10 mM bromide to elongate the induction time before the first oscillation. This is convenient to allow us ample time to form the emulsion, seal the sample cells, and adjust the microscope before oscillations start. The intensity of the image during the induction period was set to 0 for normalization. Shortly after the beginning of oscillations, when t = 94 s, almost all the drops suddenly transitioned to the oxidized state and the total intensity reached maximum. This intensity was set to 1 for normalization. This initial simultaneous transition to the oxidized state for almost all drops was not a result of synchronization by interdrop communication. Rather it occurred because all the drops were produced with the same composition and at nearly the same time. With time, a fraction of oxidized drops relaxed back to the reduced stationary state and eventually only $\sim$1/3 drops remained at the oxidized stationary Turing state. The pattern became stable after t $\simeq$ 400 s. The stable pattern over a large domain of drops consisted of each oxidized stationary drop surrounded by 6 reduced stationary drops, giving on average 2 reduced (dark) drops for each oxidized (bright) drops, leading to a steady state intensity of 1/3 the maximum value. This pattern is similar to that observed with the 40 μm diameter drops at 640 mM malonic acid shown in Fig. 4.4a, with a similar fraction of oxidized stationary droplets. Defects in the pattern of oxidized and reduced drops are seen in Fig. 4.4b. Whether or not the defects are due to random fluctuations or arise as effects of packing imperfections and boundary

conditions is unknown.

Fig. 4.4c shows photographs of the initial and the stable state of an array of 50 μm diameter drops with a lower malonic acid concentration (m = 200 mM) than in Fig. 4.4b. At the beginning of recording, almost all drops were in an oxidized state and appeared similar to the photo in Fig. 4.4b at t = 94 s. Additionally, in a similar fashion to Fig. 4.4b, after 400 seconds, a stable pattern was reached. However, in contrast to Fig. 4.4b, approximately half (53% to be precise) of the drops remained oxidized. We note that the stable state was mainly composed of small domains of drops arranged in two different patterns. The first pattern had three-fold symmetry and is highlighted with a red circle in Fig. 4.4c. The pattern is the complement of Fig. 4.4b, i.e., each reduced stationary drop was surrounded by six oxidized stationary drops and on average there were two oxidized drops for each reduced drop. The second pattern, with two-fold symmetry, was more of a labyrinth, highlighted with a blue circle in Fig. 4.4c. The pattern consists of a line of reduced drops parallel to a line of oxidized drops, resulting in a 50-50 mix of oxidized and reduced drops. The two-fold symmetric labyrinth pattern was present in a much higher proportion than the three-fold symmetric pattern.

Taken together, the data in Fig. 4.4 demonstrated a clear trend of increasing fraction of drops in the oxidized stationary Turing state with increasing coupling strength accomplished by either reducing the drop diameter at constant malonic acid concentration, or reducing malonic acid concentration at constant drop diameter. We examine this phenomenon further with numerical simulations in the next section.

4.2.3.2 Finite element simulation of 2D patterns

To better understand the relationship between the various Turing patterns in 2D hexagonal lattices as a function of the inhibitory coupling strength, we performed finite element modeling using COMSOL multiphysics software.

In previous work[9], a simplified point model was used for simulating 2D lattices of BZ droplets. Each drop was considered to be a single point and the oil separating drops was treated implicitly by considering a specific coupling of chemicals directly between nearest neighbors. Here we employ finite element modeling which allows for explicitly considering both the size of the drop and the amount of oil separating drops[17]. To speed up the calculation, we restricted the model to two dimensions as shown in Fig. 4.5, which compares experiment and simulation. The same FKN theory was used in these simulations as in previous works for the equations governing chemical reactions and are included in the appendix for completeness[17, 10]. We allowed only bromine to diffuse between droplets through oil gaps in these simulations with a partition coefficient of 2.5. Bromine concentration is shown in color with bromine flux shown in black arrows. An oxidized stationary droplet has a higher bromine concentration and hence is redder than the reduced stationary drops. The color scale in oil gap is different (2.5 times higher) from that in the aqueous droplet for better appearance. The initial chemical conditions used in the simulation were chosen to be similar to the experimental initial chemical conditions. Note that these conditions are different than the steady state solutions of the reaction-diffusion equations. Random initial bromide ion concentrations were used for the drops in the unit cell so that every drop would start differently from the others. The randomness was limited to 20% of the average value of initial bromide ion concentration, 5e-5 M. The initial chemical conditions for other species in simulation were chosen to be similar to experimental initial chemical conditions, i.e. all catalysts were in the reduced state and the concentrations for the other species were nearly zero. Periodic boundary conditions were applied to the parallel pairs of the polygons.

In a 2D system, the monolayer of BZ drops is arranged in hexagonal lattice, thus a hexagon unit cell was a natural choice for simulation (Fig. 4.5b and 4.5d). The hexagon unit cell involves 7 drops, with 6 drops partly inside the cell and the center one fully inside, resulting a total of 3 full drops in the unit cell. Parallel boundaries in the hexagon cell

were set to be periodic, thus the unit cell extends to an infinite 2D plane. In the first four images, Fig. 4.5a-d, the malonic acid concentration is held constant and the drop size is varied; large drops in Fig. 4.5a-b and small drops in Fig. 4.5c-d. The simulation results using the hexagon unit cell with large drops in Fig. 4.5b resembled the experimental pattern in Fig. 4.5a in which 1/3 of the drops were oxidized. Likewise, the simulation results using the hexagon unit cell with small drops in Fig. 4.5d resembled the experimental pattern in Fig. 4.5c in which 2/3 of the drops were oxidized.

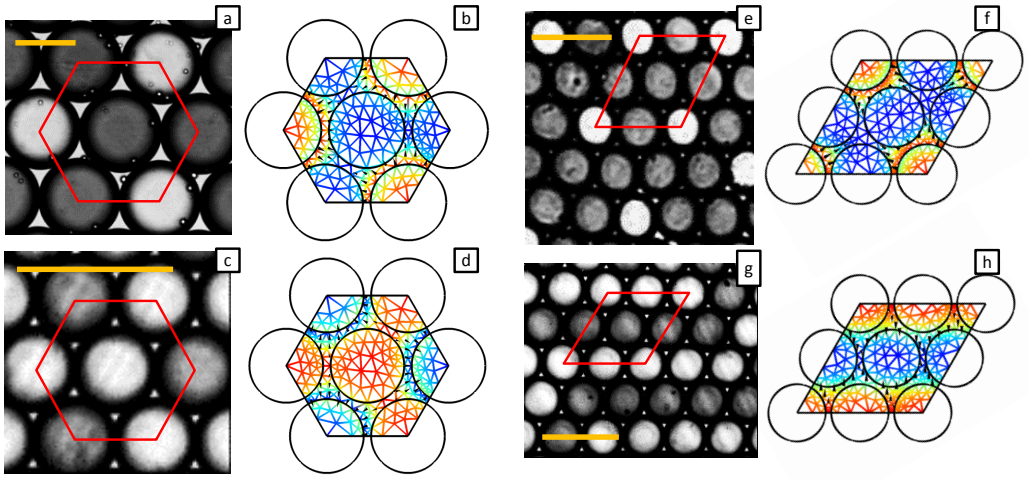

Figure 4.5: Experimentally observed stationary chemical states and finite element simulations of BZ drops in 2D. The left hand column (a, c, e, g) are experimental photographs. The yellow bar in each image is 100 μm long. The red polygon in each image is the unit cell that was simulated and displayed in the right hand column. The right hand side (b, d, f, h) are finite element calculations based on the 7-variable FKN model solved COMSOL. Bromine concentration is shown in color (orange = high, blue = low) with the bromine flux indicated by small black arrows. The small triangles in the simulations are the mesh used for calculation. The conditions for each experiment and simulation are given in Table 4.1.

Besides patterns with three-fold symmetry, we also observed patterns with two-fold symmetry, as illustrated in Figs. 4.5e & g. Diamond shaped unit cells containing 4 full drops (Figs. 4.5f & h) were used to simulate these patterns in which periodic boundary conditions

Table 4.1: Parameters in Figure 4.5.

Figure	$a(\mu\text{m})$	m (mM)	OST (%)
a	120	200	33.3
c	50	200	66.7
e	50	400	25
g	50	200	50
b	100	40	33.3
d	40	40	66.7
f	40	100	25
h	40	40	50

were also applied. The size and symmetry of the unit cell restricts the chemical states that the drops can adopt. With the hexagonal unit cell the possibilities for the fraction of drops in the stationary oxidized state are {0, 1/3, 2/3, 1}, while with the diamond cell, the possibilities are {0, 1/4, 1/2, 3/4, 1}. In order to eliminate the bias imposed by choice of the unit cell, we kept the unit cell constant and varied only one parameter at a time, i.e. the drop diameter or malonic acid concentration.

Next we examine the parameters controlling the coupling strength, i.e. malonic acid concentration m and drop diameter a, used in experiments and simulations in Fig. 4.5 as listed in Table 4.1. We consider four cases involving drops in the stationary state. In Figs. 4.5a & c, m is constant at 200 mM while a decreased from 120 μm (Fig. 4.5a) to 50 μm (Fig. 4.5c). Associated with the decrease in size is an increase in the fraction of drops in the OST state from 1/3 ($a = 120$ μm) to 2/3 ($a = 50$ μm). From Fig. 4.5c to Fig. 4.5e, the drop diameter is held constant at $a = 50\mu$m and m is increased from 200 mM to 400 mM, leading to a decrease of OST fraction from 2/3 to 1/4. In each case, the fraction of oxidized drops increases as coupling strength, S, increases. Fig. 4.5g and Fig. 4.5c were actually different parts of the same experiment, each of which are indicated by circles in Fig. 4.4c. Finite element simulations of closed packed arrays of drops as a function of a and m, shown in

Figs. 4.5b, d, f, and h, revealed the same trend in OST fraction as experimentally observed. The agreement between experiment and simulation was qualitative not quantitative. We speculate that the reasons for this quantitative mismatch are that simulation is done in two dimensions, instead of three and that the oil gap size in the finite element model was larger than in experiment. We simulated in 2D and set the minimum oil gap size between nearest neighboring drops to be 10% of the drop diameter instead of zero (for touching drops in experiments) in order to increase the speed of the numerical calculations. While dramatically saving computation time, these simplifications resulted in a weaker coupling strength for the simulations in comparison to the touching drops in experiments. Consequently, the simulations require smaller drop sizes and lower concentrations of malonic acid in order to produce the same patterns as observed experimentally.

In order to calculate a state diagram of the system of hexagonal closed packed BZ drops, we performed hundreds of simulations similar to the one shown in Fig. 4.5b for a wide range of coupling strengths by varying m and a and the results are illustrated in Fig. 4.6a. In the bottom left corner of the state diagram (blue region), where the coupling is the strongest, all drops in the hexagon unit cell are non-oscillating. Increasing m and a from the stationary region leads to the yellow region in which all three drops in the unit cell oscillate; two of the drops oscillate in-phase with each other and π radians out of phase with the third drop. We denote this pattern "00π" meaning two drops have zero phase difference and the third beats 180 degrees out of phase with the others. Weakening coupling strength by increasing drop diameter a from the stationary region leads to the dark red region, which is another pattern in which all three drops in the unit cell oscillate, but this time each drop has a 120 degrees phase shift with its two neighbors in the unit cell. We denote this pattern "$2\pi/3$". We find the same pattern in the top right corner of the diagram where the coupling is the weakest. The initial chemical conditions for each drop in the unit cell were taken from an isolated free-run drop at phase shifts of 0, 120 and 240 degrees on the limit cycle at $m = 400$ mM.

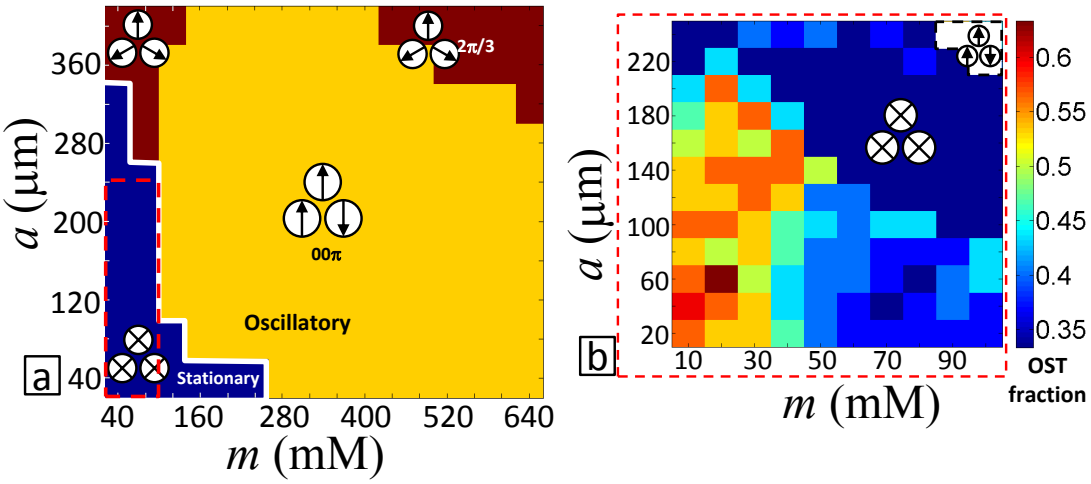

Figure 4.6: Simulated chemical state diagram with bromine only coupling and periodic boundary conditions for a hexagonal lattice of BZ drops in 2D. (a) The model was simulated at increments of 40 mM of malonic acid concentration and in increments of 40 μm of drop diameter. Blue, yellow and dark red regions represent stationary, 00π oscillation, and $2\pi/3$ oscillation, respectively. Controlled initial condition was used. (b) State diagram for stationary Turing patterns. Simulations were performed at intervals of 10 mM of malonic acid and at intervals of 20 μm, with 10 trials of random initial conditions. The randomness was limited to 20% of the average value of initial bromide ion concentration, 5e-5 M. The color scale represents the fraction of oxidized stationary Turing state, e.g. 0.33 (dark blue) means 1/3 of the drops are oxidized

Since this initial condition is the only other kind of initial condition we used for simulations besides the random initial condition, we denote it as the "controlled initial conditions" in this paper. We also numerically verified that decoupled ($P_{\mathrm{B}} = 0$) drops with conditions from the blue stationary region of the state diagram of Fig. 4.6a would oscillate autonomously, but these oscillating drops became stationary when coupled ($P_{\mathrm{B}} = 2.5$). This phenomena has been referred to as coupling-induced oscillator death[68]. Our numerical analysis suggests that the boundary between the stationary and oscillatory border in the state diagram does not depend on initial conditions.

At this point, we make a brief comparison of simulation and experiment. Qualitatively, there is a correspondence between regions of strong and weak coupling strength. For both computation and experiment at strong coupling (small drops, low malonic acid) the drops are stationary, while at weak coupling all drops oscillate in the $2\pi/3$ state. We note that there is a significant discrepancy between the computed state diagram of Fig. 4.6 and the experiments of Fig. 4.4a. In experiment, for intermediate coupling strength, indicated by Region II of Fig. 4.4a we observe the $s0\pi$ state. However, in simulation this state is never observed for homogeneous drops. Instead, all drops oscillate in the 00π state, which, in spite of hundreds of experiments, was never observed in large arrays of hexagonally packed drops. The origin of this discrepancy will be explored in the section on heterogeneity.

To explore further the stationary Turing pattern and quantify the fraction of drops in the oxidized stationary Turing state as a function of coupling strength, we performed simulations with higher resolution of m and a in part of the blue (stationary) region indicated by the red dashed lines. Fig. 4.6b shows the fraction of drops in the Oxidized Stationary Turing (OST) state using a different color map ranging from 1/3 (blue) to 2/3 (red). We observed that the OST fraction also depends on initial conditions to a certain degree. Consequently, we averaged the results from 10 trials of simulation at each point of the inset diagram with randomized initial concentrations of bromide ion, the actual inhibitor in aqueous phase[30,

31], for each of the 3 drops in the unit cell. We can see that as m increased beyond 50 mM, or once a increased beyond 200 μm, the fraction of OST decreased quickly. Overall, the computations reveal that the of fraction of stationary drops in the oxidized state increases with smaller drop diameter and/or lower malonic acid concentration, i.e. with increased stronger coupling strength. This trend agrees qualitatively with the experiments in Figs. 4.4 and 4.5.

The state diagram in Fig. 4.6a agrees with one calculated previously using a point-oscillator model[15]. The only differences are that we considered activator coupling as well as inhibitory coupling, which produced in-phase synchronous oscillations in the limit of high coupling strength[15]. We verified that in-phase oscillations at high coupling strength occur in the finite element model when activation coupling was included. Since we never observed in-phase oscillations at high coupling strength in experiment, we only considered inhibitory coupling in this section.

4.2.3.3 Heterogeneity in mixed patterns

The one qualitative difference between the simulated phase diagram and the experiments is that in spite of a large number of attempts using a wide range of parameters, simulations of a hexagon unit cell composed of identical BZ drops lack a mixed oscillatory and stationary state, such as the experimentally observed $s0\pi$ state in Fig. 4.4a, region II. As mentioned in previous work[15], some heterogeneity must be introduced to either the geometry (i.e. the drop diameter or interdrop spacing), or in the chemistry of the drops in order for the simulations to generate mixed oscillatory and stationary patterns that resemble the experimentally observed patterns.

In Fig. 4.7 we employ finite element calculations to numerically explore the effect of heterogeneity in chemistry, specifically the acidity $[H^+]$ in BZ drops. The oscillation frequency increases rapidly with increasing acidity[30, 31]. The simulation employed a hexagonal unit

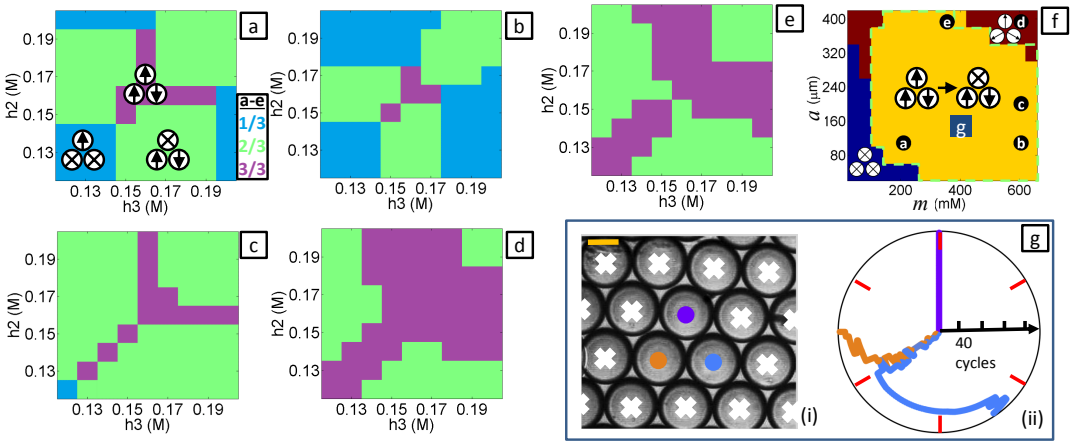

Figure 4.7: Effect of chemical heterogeneity on the states of BZ drops in hexagonal lattices. (a)–(e) are the fraction of drops that oscillate, calculated with parameters m and a as indicated in the phase diagram (f), the same phase diagram as portrayed in Fig. 4.6. The same finite element module and controlled initial condition was used for the simulations in (a)–(e) as in the phase diagram (f). The light blue region in (a)–(e) represents patterns with 1/3 of drops oscillating; light green region with 2/3 of drops oscillating; purple region for all (3/3) drops oscillating. The light green dashed line in phase diagram (f) marks the region of $s0\pi$ pattern with $h_2 = 0.15$ M and $h_1 = h_3 = 0.16$ M, which is almost identical to the yellow region of 00π for homogeneous drops. (g(i)) is a photograph of three optically isolated drops and is the closest experimental observation of the 00π pattern. The drops with "x" had light shone on them, which set those drops in the reduced, stationary state[15]. The yellow bar is 100 μm long. (g(ii)) is a radial space-time plot with the time axis radial with a length corresponding to 40 oscillations. The polar angles mark the relative phase shift between oscillating drops. The color coding identifies the drops in g(i). The phase shift is plotted relative to the purple drop and the phase of the purple drop is fixed at zero degrees.

cell consisting of three drops of identical diameter with periodic boundary conditions, such as shown in Fig. 4.5b. Each of the three drops in a unit cell are allowed to have different values of $[H^+]$: h_1, h_2, h_3. We let two of these three values, i.e. h_2 and h_3, vary from 0.12 M to 0.2 M in increments of 0.01 M and leave one drop, h_1, fixed at 0.16 M. In Figs. 4.7a to 4.7e, we vary the drop size a and malonic acid concentration m, the two parameters that most strongly control the coupling strength. The values of m and a used in Figs. 4.7a-e are indicated by the corresponding letter in Fig. 4.7f. From the strongest coupling in Fig. 4.7a to the weakest coupling in Fig. 4.7d we noticed the trend of increasing area of the fully oscillatory domain in purple, as well as the trend of diminishing area of the blue domain where only one third of the drops oscillate. All non-oscillating drops were effectively in the reduced stationary state, although they were actually oscillating with a very small amplitude that was only observable in numerical simulations. The minimum amounts of heterogeneity in $[H^+]$ needed for $s0\pi$ state were 0.01 M (i.e. 1/16) for cases a, b, c, e and 0.02 M (1/8) for case d.

In Fig. 4.7f we recalculated the phase diagram with the minimum heterogeneity in h_2 so that $h_1 = h_3 = 0.16$ M and $h_2 = 0.15$ M. The result was nearly identical to the homogeneous case in which all drops had the same acidity, $h_1 = h_2 = h_3 = 0.16$ M, shown in Fig. 4.6, except that almost all of the 00π pattern denoted by a yellow region in Fig. 4.6 transformed to the $s0\pi$ pattern as indicated by the yellow color and light green dashed line in Fig. 4.7f. The simulation agrees with what we found in experiments (Fig. 4.4a region II) in that $s0\pi$ pattern occurs at medium coupling strength.

The 00π state observed in the simulated state diagram of perfectly identical drops, shown in Fig. 4.6a, was never observed in experiments on large arrays of drops, which contain both chemical and physical heterogeneities. However, there is one experimental example of the 00π state, which was for the case of a triplet of drops isolated from the rest by using light to impose constant chemical conditions[15]. Fig. 4.7g shows our observation of the 00π state

in a system with $m = 400$ mM and $a = 150$ μm, as indicated in Figs. 4.7(f) with a blue "g". Three times of the typical Ru(bipy)$_3$ concentration was used in this particular experiment. In Fig. 4.7g(i) the drops marked with a white "x" are optically inhibited creating constant chemical boundary conditions for the three drops in a triangle indicated with colored circles. Fig. 4.7g(ii) presents a radial-phase-time plot of the three drops in Fig. 4.7g(i). Time starts at the center of the plot along the radial axis and the phase relative to the purple drop is shown on the angular axis. The whole experiment was approximately 3 hours long and contained 40 oscillations for each drop. For approximately 35 oscillations the orange and blue drops are synchronized with zero relative phase and approximately $2\pi/3$ out of phase to the purple drop. Eventually the 00π state decays into the $2\pi/3$ phase state. Although the phase difference between the purple drop and the other two was not π, this was the closest experimental pattern we could find for the 00π state.

4.3 Turing Morphogenesis

Turing argued that in Turing state d identical biological cells chemically differentiate into active and inactive states and speculated that an activated gene could catalyze an increase in the concentration of intracellular molecules, thereby driving physical differentiation by increasing the osmotic pressure in that cell, causing it to swell[1]. In Figure 4.8 we demonstrate precisely this effect in a hexagonal packing of microfluidically prepared identical drops in Turing state d. The intensity of each drop is a monotonic function of the fraction of oxidized BZ catalyst it contains. As shown in Figure 4.8a, the drops are initially homogeneous in chemistry and drop size. After an initial induction time, the drops undergo a transition from this unstable steady state to the Turing case d in which one out of three drops is in the reduced (dark) state and two out of three are oxidized (bright), shown in Figure 4.8c. This chemical differentiation occurs with the drop size remaining constant. The oxidized drops

are catabolically active, consuming reagents faster than the reduced drops. This creates an osmotic pressure imbalance causing water to flow from the oxidized to reduced drops creating a morphological transformation in which the initially homogeneous cells differentiate into two populations with distinct chemical redox states and physical sizes, as shown in Figure 4.8e.

To investigate the origin of the physical change of BZ drops, consider the net reaction in the FKN[30] model of the BZ reaction:

$$3BrO_3^- + 5CH_2(COOH)_2 + 3H^+ \rightarrow 3BrCH(COOH)_2 + 2HCOOH + 4CO_2 + 5H_2O \quad (4.3)$$

We assume that this is the major reaction that takes place in going from the reduced to the oxidized state. With the initial concentrations used, we have to take into account the counterions (every BrO_3^- comes with an Na^+, H^+ comes from H_2SO_4) and assuming the sulfuric acid starts off as $H^+ + HSO_4^-$, but HSO_4^- dissociates to $H^+ + SO_4^{2-}$ when the reaction consumes H^+. The limiting reactant is the MA. If the reaction goes to completion in the oxidized state, all the MA is consumed. We assume that essentially all the CO_2 partitions out of the drops. The initial and final concentrations are:

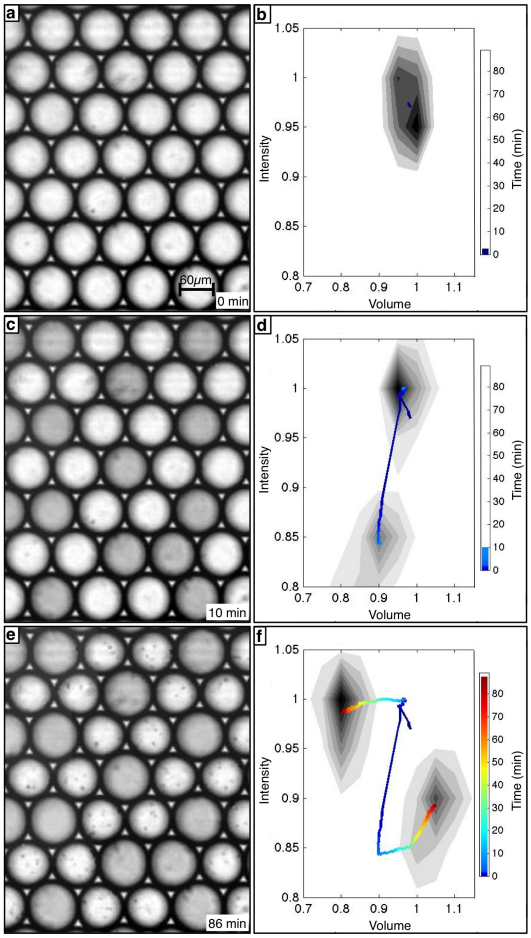

Figure 4.8: Images and histograms of drops demonstrating morphogenesis plotted as fraction of original drop area *vs.* fraction of original drop intensity. The color coded line tracks the center of each peak as a function of time. a-b) Initially, drops are homogenous in both intensity and size. Bright drops are oxidized, dark drops reduced. c-d) At intermediate times the drops undergo a Turing case *d* (q,0) instability; heterogeneous in intensity, or oxidation state, but homogenous in size. e-f) At later times drops are heterogeneous in both oxidation state and size. The oxidized (bright) drops shrink and reduced (dark) drops swell. Chemical conditions: 200 mM MA, 0.4 mM Rubipy, 0 mM NaBr, 80 mM H_2SO_4, 300 mM $NaBrO_3$, 3 mM Ferroin, 0.05 $\times$ 1 mm capillary, initial drop size $\sim$66 μm. Adapted from previous work[15].

Species	Initial conc. [mM]	Final conc. [mM]
Na^+	300	300
BrO_3^-	300	180
MA	200	0
H^+	80	40
HSO_4^-	80	0
SO_4^{2-}	0	80
BrMA	0	120
HCOOH	0	80
Total	960	800

If we further assume that the drops in the reduced state consume no malonic acid and the drops in the oxidized state go to completion, then this calculation shows that the maximum difference in molarity is 17% between a reduced and oxidized drop. This difference in molarity will drive a flux of water between the drops until the molarity of the drops is equal. In the experiment, roughly two-thirds of the drops are oxidized and one-third reduced. This leads to the prediction that the oxidized drops shrink by 6% in volume and the reduced drops swell by 12% in volume. The drops have a measured diameter of ~ 60 μm and they are confined in a rectangular capillary of 50 μm height. Assuming the drops are spheres leads to the prediction that the ratio of the radii of the swollen (reduced) to shrunken (oxidized) drops is 1.06, while assuming the drops are highly confined in height to be approximated as disks, the ratio of radii becomes 1.09. The measured ratio is 1.1, consistent with the crude estimates given above. Additionally, we can think of no other plausible mechanism to account for the change in size of the drops besides osmotic pressure. The combination of the reasonable physical mechanism and agreement between quantitative prediction and measurement leads us to conclude that osmosis drives the shape change, as speculated by Turing.

Chapter 5

Self-Oscillating Gel

The time you enjoy wasting is not wasted time.

Bertrand Russell

This chapter is a small deviation from the main topic of this thesis, yet an important potential application of BZ oscillation. Here we present some unpublished work on poly-N-isopropylacrylamide (pNIPAm) hydrogel. The main purpose of this chapter is to provide some references for the convenience of future research. We try to be brief without going into details as the concepts we describe in this chapter were better explained in the references. The results in this chapter are preliminary and unoriginal, but hopefully heuristic in preparing one to enter this field.

5.1 Experiments

Our interest in pNIPAm gel was inspired by previous works in self-oscillating gels driven by the BZ reaction as biomimetic materials[69]. As first reported in 1996 by Yoshida *et al*[70], the mechanical oscillation was achieved by inducing the BZ reaction within a copolymer gel

of NIPAm with $Ru(bpy)_3^{2+}$ covalently bonded to the polymer chain. The catalyzed pNIPAm gel swells and deswells at the oxidized and reduced states of $Ru(bpy)_3$ while converting chemical energy from the BZ reaction into the mechanical energy of the polymer network.

Despite numerous simulations that were reported to resemble the swelling and deswelling in $Ru(bpy)_3$ catalyzed pNIPAm gel[71, 72, 73], a quantitatively accurate prediction of the gel volume change cannot be made without further understanding in the underlying physics. The thermodynamics of hydrogel swelling by water absorption was founded by Flory and Huggins in the 1940's[74]. In the late 1970's, Tanaka *et al* discovered that gels change volume reversibly and discontinuously in response to environmental changes such as solvent composition, temperature, and pH change[75]. Tanaka developed the classic mean-field theory of volume phase transition in gels incorporating Flory's theory of polymer-solution mixing, elasticity, and ionic interactions[76]. Grosberg and Nechaev improved Tanaka's theory by considering the neglected influence of topological constraints on subchain conformations in the polymer network and achieved better quantitative agreement with experiments[77].

It is natural to study the swelling and shrinking of catalyzed bulk pNIPAm gels at first because of the relatively simple gelation process and the convenient methods of observation such as microscopy[78, 79]. However, since the motion of the polymer network of a gel during the time course of swelling and shrinking is described by a collective diffusion equation[80], the time needed for a gel to change its volume and shape is proportional to the square of a characteristic length of the gel. Hence microgel particles with a small radius will have a much faster response to a change of the environment. For example, the time needed for volume change is 10^7 s for a spherical gel of 1 cm radius but is only 10^{-3} s for that with 1 μm radius. The phase transition of gels is a macroscopic manifestation of the coil-to-globule transition of individual linear chains. A comparison between the $Ru(bpy)_3$ catalyzed pNIPAm microgel and polymer chains in water will improve our understanding of the swelling and shrinking mechanism of self-oscillating gels at the molecular level.

Our goal is to eventually synthesize $Ru(bpy)_3$ catalyzed pNIPAm microgel beads[81, 82] and polymer chains[83], then carry out similar investigations to the properties of these gels and polymers similarly as in the previous works[84, 85]. Therefore repeating previous investigations in non-catalyzed pNIPAm gels would be a helpful practice to learn the necessary skills for the more challenging study of the catalyzed polymer and gel.

Here is our protocol for non-catalyzed pNIPAm microgel synthesis, following Pelton's recipe[86, 87]:

1. Prepare 100 ml two-neck round bottom flask, two rubber stoppers for the flask, stir bar, reflux condenser, a rubber stopper for the condenser, needle for pressure balance, long needle for oxygen removal with nitrogen, oil bath (heavy mineral oil), thermometer with wire probe, and heat/stir plate.

2. Put 0.7 g NIPAm (N-Isopropylacrylamide, 99%), 0.07 g BIS (N,N'-Methylene-bis-acrylamide), 0.0094 g SDS (sodium dodecyl sulfate) into the flask, then add 47 ml water (do not shake the flask otherwise the powder may stick to flask wall). Set oil bath at 70° and blow nitrogen into the water solution for 30 minutes to remove oxigen. The solution is stirred at high rate with a large vortex in the center (unknown stir rate due to old device).

3. Pull the needle out of water solution but still leave it in. Add 3 ml water solution of 0.024 g (0.0001 mol) APS (ammonium persulfate, 98%) into the flask. Keep stirring for 4 hours. The stir rate is tuned down (to avoid the large vortex) after adding APS. Then let it cool down slowly in the oil bath but keep stirring.

4. Centrifuge, decantation and dispersion with deionized water to remove SDS, polymer chain and other impurities. Centrifuge speed: 12 krpm $\times$ 30 min for three times. Dispersion: 1 hour vortexing at maximum speed. Only small amount is centrifuged and the rest of the stock remains raw, as SDS may prevent microgel from aggregating.

The experiment was successful at the first (and the only) trial and we obtained 50 ml colloidal solution of fairly monodispersed pNIPAm gel microspheres with the average diam-

eter of 265.4 nm and the coefficient of variation of 7.5%. The microgel beads are shown in Fig. 5.1 as small black dots in the TEM image.

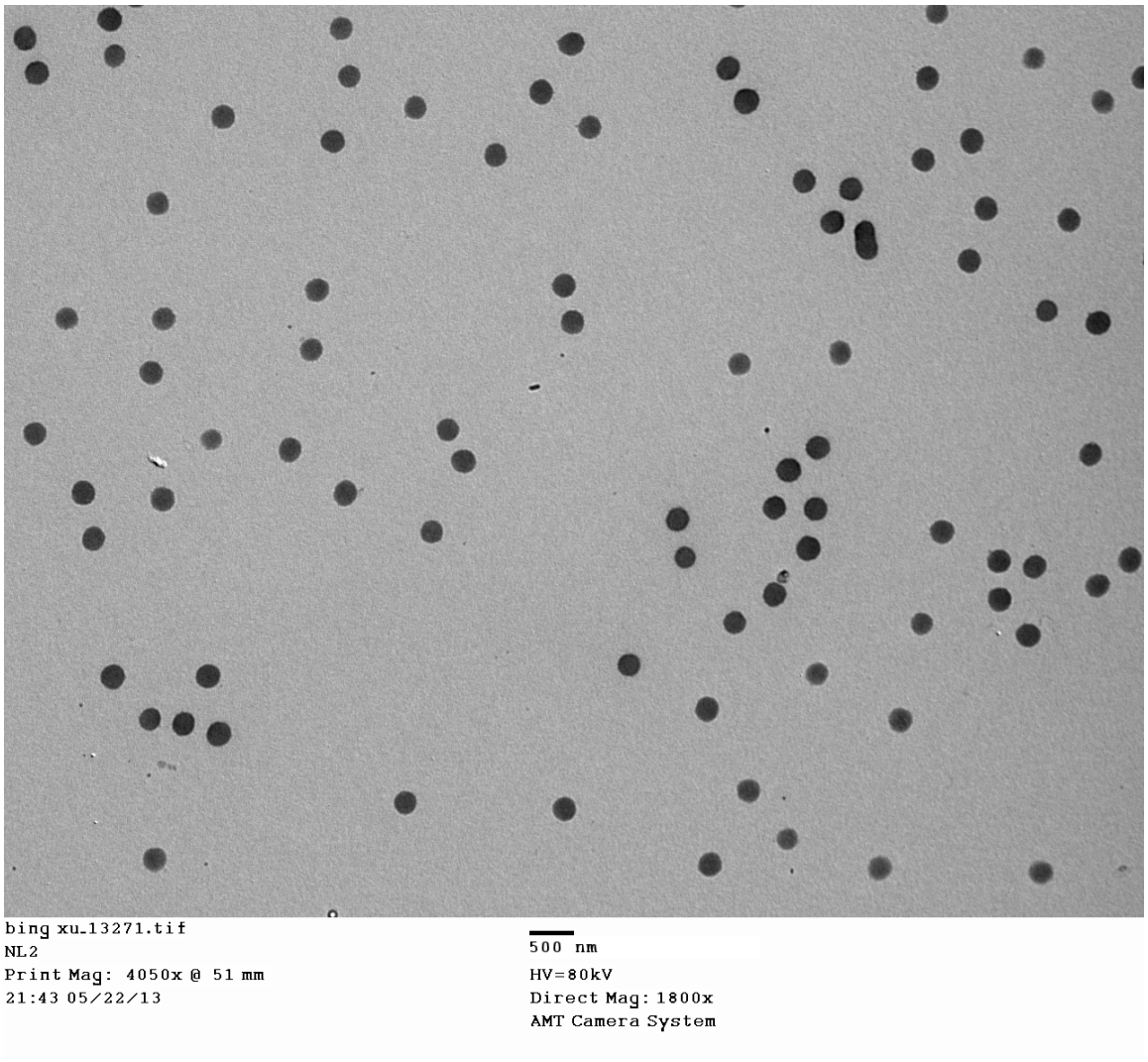

Figure 5.1: TEM image of microgel beads.

Dynamic and static laser light scattering were used in the studies of polymer chains and submicron gel beads. Small sample particles undergoing Brownian motion give fluctuation to scattered light intensity. Dynamic light scattering (DLS) is a technique that analyzes the scattered intensity correlation function at a known angle, provides the diffusion coefficient and hence the hydrodynamic radius via Stokes-Einstein equation. Measuring the radius of gel

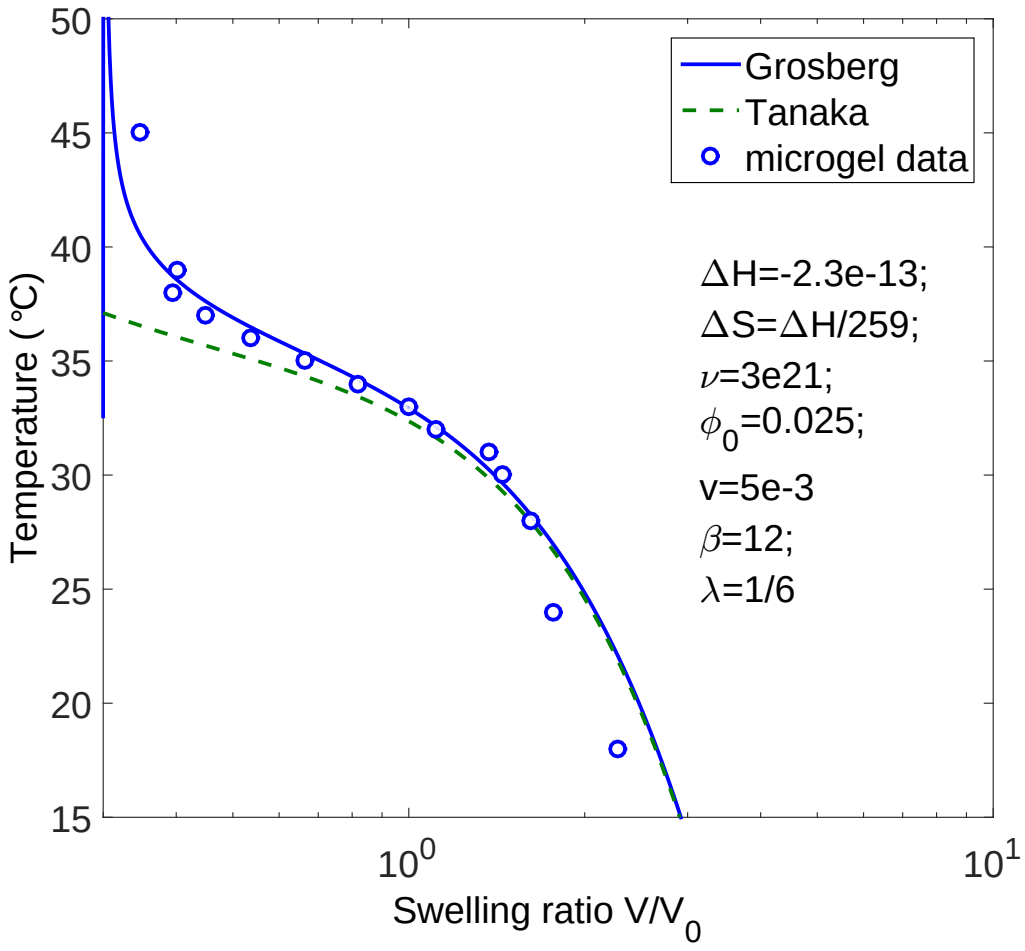

Figure 5.2: Theoretical swelling curves and experimental data of microgel.

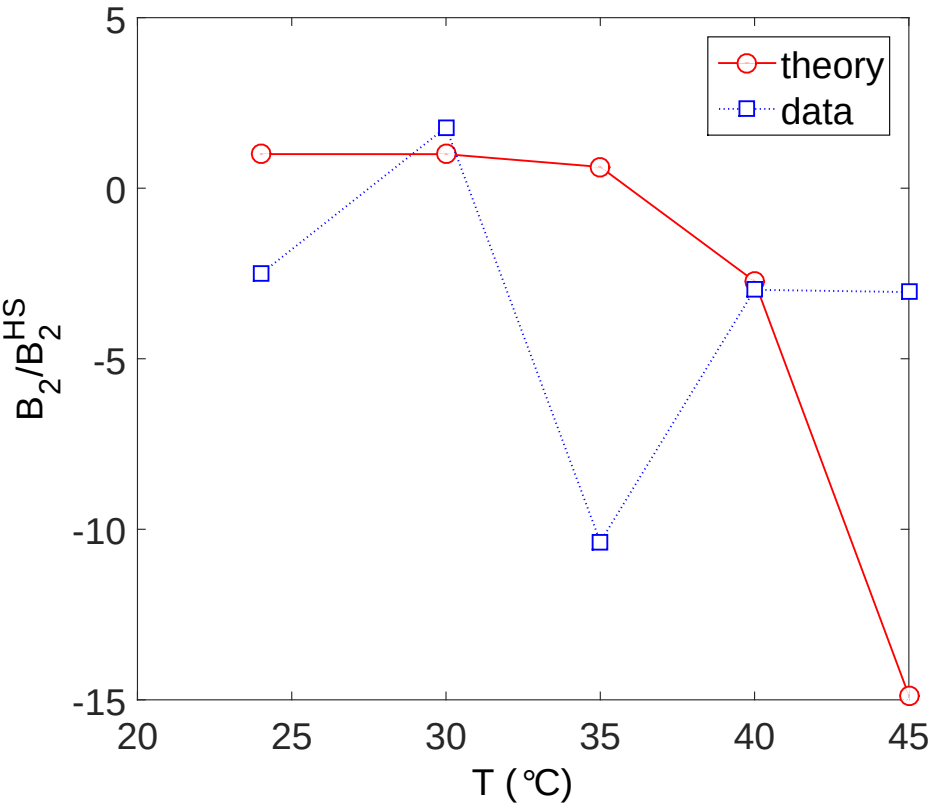

Figure 5.3: Reduced osmotic second virial coefficients. Five diluted microgel samples with concentrations evenly distributed from 0.003 to 0.015 g/L were used in the SLS measurement. dn/dC was assumed to be 0.18 ml·g^{-1} as in ref. [84] instead of accurately measured.

beads at various temperature provides the swelling curve which is the essential experimental data to be compared with theory. Static light scattering (SLS) provides the average molecular weight by measuring the intensity of the scattered light; measurement at multiple angles allows calculation of the radius of gyration; measurement for multiple sample concentrations gives the second virial coefficient, which depends on the pair interaction between the particles and therefore is an important parameter in understanding the swelling mechanism at the molecular level.

In Fig. 5.2, we compare the experimental swelling curve from our microgel (diluted to 0.015 g/L, using DLS) with theories of Tanaka and Grosberg, as shown in Eqs (8) and (11) in ref. [77], respectively. The improvement to Tanaka's theory made by Grosberg is demonstrated with the better agreement with experimental data.

We also measured the second virial coefficient of the microgel beads using SLS and compared with the theory in Fig. 4 of ref. [85]. The result, as shown in Fig. 5.3, was unsatisfactory and further investigation is needed.

5.2 Simulations

Numerous simulation results for self-oscillating BZ gels have been reported previously[71, 72, 73]. Finite element methods are commonly used in these simulations. Using diffusion module and strain module in COMSOL Multiphysics with Tyson-Fife model for BZ chemistry[88], we explored the possibility of simulating BZ gel volume oscillation. The results are preliminary yet promising. We followed the frame of theory in ref. [73] which was based on the model developed by Suo *et al*[89, 90]. The COMSOL implementation of the theory was learned from a Master's thesis[91]. The model file "gel_volume_oscillation(diffusion-strain-TF).mph" can be found in Fraden lab's homegroup space.

We demonstrate the prototype COMSOL simulation with a simple 2D square geometry

(with a width of 1e-4 m), representing a small piece of square gel soaked in BZ solution. The geometry was meshed into 68 triangular elements with deformable mesh frame enabled. The concentrations c1 and c2 in Tyson-Fife model correspond to the activator X and the oxidized catalyst Z in the FKN model. And the total displacement evaluated at the top left corner of the square gel is synchronized with c2 as shown in Fig. 5.4.

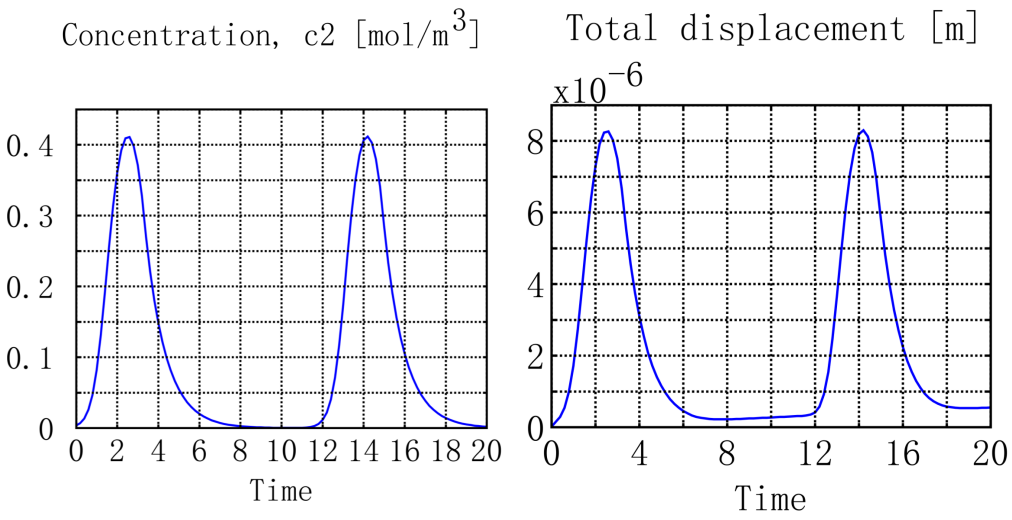

Figure 5.4: Catalyst concentration c2 and displacement.

Snapshots for minimum volume at $t = 8$ s and maximum volume at $t = 14.2$ s are shown in Fig. 5.5. Color scale is for c2 concentration (red is high) and the black arrows are displacement vectors (therefore no arrow for minimum volume).

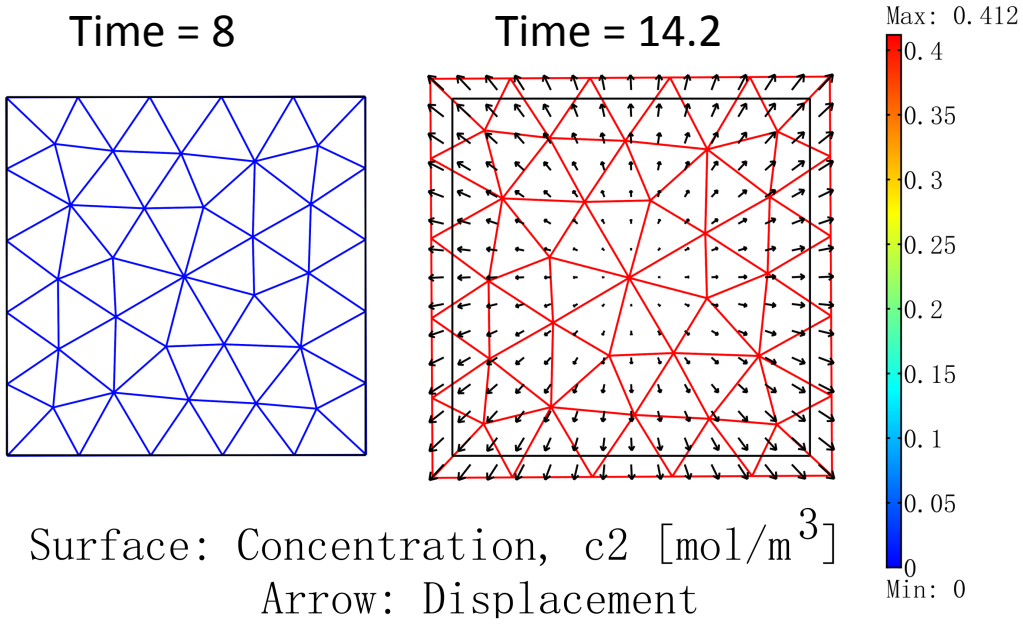

Figure 5.5: Snapshots for minimum and maximum volume. The deformed mesh used for simulation is shown here.

Chapter 6

Conclusion

The point of philosophy is to start with something so simple as not to seem worth stating, and to end with something so paradoxical that no one will believe it.

Bertrand Russell

Through the development of an experimental system of diffusively coupled synthetic cells containing the Belousov-Zhabotinsky chemical reaction we performed the first quantitative experimental tests of how well the Turing model describes reaction-diffusion cellular systems in linear arrays, rings and 2D hexagonal networks. Each of the BZ chemical species is known and as transport is restricted to permeation through the oil separating BZ drops, reaction-diffusion is the only possible mechanism accounting for the phenomena reported in this thesis. Quantitative synchronization experiments are consistent with the functional form of the coupling term, but our calculation overestimates coupling strength.

In arrays of drops confined to lines and rings, five of the six distinct states corresponding predicted by Turing's linear stability analysis are observed, but their locations and final forms

are significantly modified by nonlinearities. The implication is that linear analysis serves as a qualitative guide to behavior; the prediction that two of the states are stationary and non-uniform and three are synchronized oscillatory states is borne out, but a full non-linear numerical treatment is necessary for quantitative and predictive theory.

First, we learned that in 1D BZ systems, emulsions introduce a new length scale, the drop separation, with two regimes of behavior: strong and weak coupling, depending on whether or not the reaction-diffusion length (λ) is longer (strong) or shorter (weak) than the drop separation. For the conditions we study, emulsions confined to one dimension, inhibition due to inter-drop diffusion of Br_2 causes neighboring drops to oscillate out-of-phase with each other. In experiments on large numbers of drops in a linear array at high concentrations of malonic acid, we measure transient phase defects that take a long time to anneal, indicative of weak chemical coupling. In contrast, at low malonic acid, the transients anneal quickly. Simulations bear out this observation and also indicate that the boundaries influence the phase differences between oscillators. The influence of the boundaries is a function of malonic acid; the boundary influence is greater at high malonic acid, corresponding to weak coupling between oscillators. In order to study interacting BZ droplets systematically, we developed a programmable illumination system that allows the setting of both boundary and initial conditions. We studied the behavior of groups of 3, 4 and 5 drops. The attractors are predominantly out-of-phase as a consequence of the inhibitory coupling, but are modified in non-trivial ways by the boundary conditions. In the case of 4 drops, a second attractor, reflecting the symmetry of the system, is observed. The simulations for the small drop system are in very good agreement with experiment with no adjustable parameters.

We then further investigated 1D systems with more significant excitatory coupling. While we have not been able to manipulate the inhibitory and excitatory coupling completely independently, the present experimental system affords considerably more control over coupling than experiments in which interaction between oscillators occurs via an aqueous phase, so

that all species participate in proportion to their concentrations[49], or systems in which the inhibitor dominates the coupling between droplets. Numerical investigations of the more complex 1D patterns suggest that both excitatory and inhibitory coupling are involved.

The fact that our experimental system is closed prevents us from obtaining true attractors, but the persistence of patterns that exhibit the same qualitative behavior for many cycles of oscillation suggests that these behaviors would be stable if we were able to maintain constant conditions indefinitely. This conjecture is supported by the striking similarities of even the most complex patterns in our experiments with the results of the simulations in open systems, which represent true attractors.

The main conclusions for 1D BZ systems are:

1. The dynamical phase behavior of a chain of BZ drops is a function of coupling strength. As coupling strength increases, the following sequence is observed in experiment and numerical models: anti-phase, bistable anti-phase and in-phase / stationary Turing states, in-phase.

2. Malonic acid concentration controls the coupling between BZ drops in oil by varying the balance between excitatory and inhibitory coupling. Mechanistically, malonic acid removes the inhibitor; therefore decreasing malonic acid increases inhibitory coupling. Drop size is a more dominant factor in coupling strength than the length of the oil gap. Theory suggests inhibitory coupling strength is characterized by $S = P_{\mathrm{Br_2}} D/(a(a+b)k_{\mathrm{eff}})$.

3. Numerical models demonstrate that weak coupling solely through the inhibitors, Br_2 and Br^-, produces phase repulsive coupling, leading to anti-phase synchrony, while coupling solely with activators, $HBrO_2$ or $BrO_2\cdot$, produces attractive phase coupling, leading to in-phase synchrony. Strong inhibitory coupling also produces in-phase synchrony; essentially the drops lose their individual identities and effectively act as a single drop in the strong coupling limit. The transition from weak to strong coupling is marked by a transition from out-of-phase to in-phase synchrony and occurs at $S \approx 1$.

4. Comparing a finite element model to experiment, we conclude that Br_2, $BrO_2\cdot$, and $HBrO_2$ exchange between drops with partition coefficients $P_{Br_2} = 2.5$, $P_{BrO_2\cdot} = 1$, and $P_{HBrO_2} \approx 0.01$; both excitatory and inhibitory coupling need to be included in the models to agree with the experiments.

5. The point oscillator model qualitatively agrees with experiment and a realistic 3D finite element model.

6. An accurate phase model was constructed for the case of weak coupling and anti-phase attractors.

7. Malonic acid concentration decreases with time in the closed system of microfluidic drops. In contrast, our numerical models consider the malonic acid concentration to be constant.

8. Malonic acid and bromine react in the oil, which is not accounted for in our numerical models.

9. Simple numerical models account for the majority of the observations.

In 2D arrays, we described the transition from oscillatory to stationary chemical states with increasing coupling strength, controlled by independently varying the reaction chemistry within a drop and diffusive flux between drops. For stationary drops, we studied how the ratio of stationary oxidized to stationary reduced drops varies with coupling strength. We observed one mixed oscillatory and stationary state that is inconsistent with the linear and nonlinear versions of the Turing model, as well as with finite element calculations. Our theoretical analysis of the $s0\pi$ state requires slight sample heterogeneity, which was not considered in the original Turing model. As our theory is generic and heterogeneity is ubiquitous in nature, we expect the $s0\pi$ state to occur in a wide range of reaction-diffusion systems. Finally, we experimentally establish for the first time, Turing's prediction that interacting identical cells differentiate into chemically distinct populations, which subsequently transform physically

in size, thereby demonstrating that these synthetic cells are pluripotent and that abiotic materials can undergo morphogenesis *via* the Turing mechanism.

The main conclusions for 2D BZ systems are:

1. Both reaction and diffusion mediate the coupling strength through the dimensionless parameter S. Chemical reactions through the malonic acid concentration, m and physical diffusion through the drop diameter, a. Chemically, increasing m increases bromine consumption *via* the bromination of malonic acid inside a drop, hence the bromine diffusing from other drops would have less effect at increasing the bromine concentration inside the drop with high m, and thereby the coupling strength is weak. Physically, increasing a increases the time for bromine to diffuse from one drop to another and thereby gives the bromine more time to react with the malonic acid. Thus the bromine in a large drop is less likely to diffuse to a neighboring drop before it is consumed. When m and a are small enough, the diffusive lateral inhibition becomes strong enough to induce oscillator death and cause stationary patterns to emerge in 2D systems. A stationary drop can be either oxidized stationary that is continuously emitting bromine, or reduced stationary that is continuously being inhibited. As m or a are decreased further, the diffusive lateral inhibition gets even stronger. More stationary drops were found in the oxidized state and fewer in the reduced state; in other words, more drops were doing the inhibiting and fewer drops were inhibited.

2. Finite element methods provide the highest accuracy for simulations of reaction-diffusion systems in complex geometries. This level of accuracy is necessary to properly simulate our 2D systems, at the price of higher computational power and longer computing time compared to simplified point models. Using the finite element model we have simulated patterns resembling all the stationary patterns we found in experiments. Over a wide range of coupling strength we generated a simulated state diagram that agreed qualitatively with experiments. The trend of increasing fraction of oxidized stationary drops with increasing coupling strength, observed in experiment, was also found in simulations. We performed

simulations with various combinations of coupling species and the best results are obtained when the coupling is through only bromine.

The current finite element model (with 3 drops inside a hexagon unit cell) can be improved for better quantitative agreement with experiments in the future by allowing the drops to touch, and by constructing a fully 3D geometry. Moreover, a larger unit cell would provide insight on the effect of diffusion beyond that of nearest neighbors.

3. Microfluidic devices generate physically and chemically monodispersed BZ droplets with only a few percent of variance. We have demonstrated that a few percent of chemical variance in simulations ($\sim$6% in acidity, which controls the oscillatory frequency) was enough to generate the $s0\pi$ pattern, which in spite of great effort, could not be found in simulations employing identical drops. Experimental observation of the 00π pattern was limited to the case of three optically isolated drops. The 00π pattern was never observed in large arrays of drops for which, inevitably, there was some heterogeneity in the lattice and hence in the coupling strength. It would be interesting to systematically investigate the effect of heterogeneity in the future by deliberating varying the physical size, chemical composition, and positions of individual drops in a variety of two dimensional lattices and networks.

Bibliography

[1] A. M. Turing. The Chemical Basis of Morphogenesis. *Philosophical Transactions of the Royal Society of London*, 237(641):37–72, 1952.

[2] Keiko U. Torii. Two-Dimensional Spatial Patterning in Developmental Systems. *Trends in Cell Biology*, 22(8):438–446, 2012.

[3] Michael Cohen, Buzz Baum, and Mark Miodownik. The Importance of Structured Noise in The Generation of Self-Organizing Tissue Patterns Through Contact-Mediated CellCell Signalling. *Journal of The Royal Society Interface*, 8(59):787–798, 2011.

[4] Pau Formosa-Jordan and Marta Ibñaes. Diffusible Ligand and Lateral Inhibition Dynamics for Pattern Formation. *Journal of Statistical Mechanics: Theory and Experiment*, 2009(03):P03019, 2009.

[5] Andrew D. Economou, Atsushi Ohazama, Thantrira Porntaveetus, Paul T. Sharpe, Shigeru Kondo, M. Albert Basson, Amel Gritli-Linde, Martyn T. Cobourne, and Jeremy B. A. Green. Periodic Stripe Formation by A Turing Mechanism Operating at Growth Zones in The Mammalian Palate. *Nature Genetics*, 44(3):348–352, MAR 2012.

[6] Rob Phillips, Jane Kondev, Julie Theriot, Hernan Garcia. *Physical Biology of the Cell*. Garland Science, 2nd edition, 2012.

[7] Irving R. Epstein and John A. Pojman. *An Introduction to Nonlinear Chemical Dynamics: Oscillations, Waves, Patterns, and Chaos*. Oxford University Press, 1 edition, 1998.

[8] Vicenc Mendez, Sergei Fedotov, and Werner Horsthemke. *Reaction-Transport Systems: Mesoscopic Foundations, Fronts, and Spatial Instabilities*. Springer Series in Synergetics. Springer, 2010.

[9] Masahiro Toiya, Hector O. Gonzlez-Ochoa, Vladimir K. Vanag, Seth Fraden, and Irving R. Epstein. Synchronization of Chemical Micro-Oscillators. *The Journal of Physical Chemistry Letters*, 1(8):1241–1246, 2010.

[10] Jorge Delgado, Ning Li, Marcin Leda, Hector O. Gonzalez-Ochoa, Seth Fraden, and Irving R. Epstein. Coupled Oscillations in a 1D Emulsion of Belousov-Zhabotinsky Droplets. *Soft Matter*, 7:3155–3167, 2011.

[11] A. N. Zaikin and A. M. Zhabotinsky. Concentration Wave Propagation in Two-Dimensional Liquid-Phase Self-Oscillating System. *Nature*, 225:535–537, 1970.

[12] R. J. Field and M. Burger. *Oscillations and Traveling Waves in Chemical Systems*. Wiley, New York, 1985.

[13] H. Fukuda, H. Morimura, and S. Kai. Global Synchronization in Two-Dimensional Lattices of Discrete Belousov-Zhabotinsky Oscillators. *Physica D - Nonlinear Phenomena*, 205:80–86, 2005.

[14] Francesc Sagués and Irving R. Epstein. Nonlinear Chemical Dynamics. *Dalton Trans.*, pages 1201–1217, 2003.

[15] Nathan Tompkins, Ning Li, Camille Girabawe, Michael Heymann, G. Bard Ermentrout, Irving R. Epstein, and Seth Fraden. Testing Turing's Theory of Morphogenesis in Chemical Cells. *Proceedings of the National Academy of Sciences*, 2014.

[16] C. Holtze, A. C. Rowat, J. J. Agresti, J. B. Hutchison, F. E. Angile, C. H. J. Schmitz, S. Koster, H. Duan, K. J. Humphry, R. A. Scanga, J. S. Johnson, D. Pisignano, and D. A. Weitz. Biocompatible Surfactants for Water-in-Fluorocarbon Emulsions. *Lab Chip*, 8:1632–1639, 2008.

[17] Ning Li, Jorge Delgado, Hector O. Gonzalez-Ochoa, Irving R. Epstein, and Seth Fraden. Combined Excitatory and Inhibitory Coupling in a 1-D Array of Belousov-Zhabotinsky Droplets. *Phys. Chem. Chem. Phys.*, 16:10965–10978, 2014.

[18] Hans Meinhardt. Turing's Theory of Morphogenesis of 1952 and the Subsequent Discovery of the Crucial Role of Local Self-Enhancement and Long-Range Inhibition. *Interface Focus*, 2012.

[19] Masahiro Toiya, Vladimir K. Vanag, and Irving R. Epstein. Diffusively Coupled Chemical Oscillators in a Microfluidic Assembly. *Angewandte Chemie International Edition*, 47(40):7753–7755, 2008.

[20] Shelley L. Anna, Nathalie Bontoux, and Howard A. Stone. Formation of Dispersions using "Flow Focusing" in Microchannels. *Applied Physics Letters*, 82(3):364–366, 2003.

[21] T.M. Squires and S.R. Quake. Microfluidics: Fluid Physics at the Nanoliter Scale. *Reviews of modern physics*, 77(3):977–1026, 2005.

[22] Vito DePalma and Nolan Tillman. Friction and Wear of Self-Assembled Trichlorosilane Monolayer Films on Silicon. *Langmuir*, 5(3):868–872, 1989.

[23] August Köhler. New Method of Illimination for Phomicrographical Purposes. *Journal of the Royal Microscopical Society*, 14:261–262, 1894.

[24] K. Agladze, S. Obata, and K. Yoshikawa. Phase-Shift as a Basis of Image Processing in Oscillating Chemical Medium. *Physica D: Nonlinear Phenomena*, 84(12):238–245, 1995.

[25] Rita Toth and Annette F. Taylor. The Tris (2,2-bipyridyl) Ruthenium-Catalysed Belousov-Zhabotinsky Reaction. *Progress in Reaction Kinetics and Mechanism*, 31(2):59–115, 2006.

[26] Kazuyoshi Itoga, Masayuki Yamato, Jun Kobayashi, Akihiko Kikuchi, and Teruo Okano. Cell Micropatterning using Photopolymerization with a Liquid Crystal Device Commercial Projector. *Biomaterials*, 25(11):2047–2053, 2004.

[27] J. David Musgraves, Brett T. Close, and David M. Tanenbaum. A Maskless Photolithographic Prototyping System using a Low-Cost Consumer Projector and a Microscope. *American Journal of Physics*, 73(10):980–984, 2005.

[28] Thomas Naiser, Timo Mai, Wolfgang Michel, and Albrecht Ott. Versatile Maskless Microscope Projection Photolithography System and its Application in Light-Directed Fabrication of DNA Microarrays. *Review of Scientific Instruments*, 77(6):063711–063711–11, 2006.

[29] Newcombe D.T., Cardwell T.J., Cattrall R.W., and Kolev S.D. An Optical Redox Chemical Sensor Based on Ferroin Immobilised in a Nafion(R) Membrane. *Analytica Chimica Acta*, 401(1):137–144, 1999.

[30] Richard M. Noyes, Richard Field, and Endre Körös. Oscillations in Chemical Systems. I. Detailed Mechanism in a System Showing Temporal Oscillations. *Journal of the American Chemical Society*, 94(4):1394–1395, 1972.

[31] Richard J. Field, Endre Körös, and Richard M. Noyes. Oscillations in Chemical Systems. II. Thorough Analysis of Temporal Oscillation in the Bromate-Cerium-Malonic Acid System. *Journal of the American Chemical Society*, 94(25):8649–8664, 1972.

[32] Richard J. Field and Richard M. Noyes. Oscillations in chemical systems. IV. Limit cycle behavior in a model of a real chemical reaction. *The Journal of Chemical Physics*, 60(5):1877–1884, 1974.

[33] Vladimir K. Vanag and Irving R. Epstein. A Model for Jumping and Bubble Waves in the Belousov–Zhabotinsky-aerosol OT System. *The Journal of Chemical Physics*, 131(10):104512, 2009.

[34] Vladimir K. Vanag and Irving R. Epstein. Excitatory and Inhibitory Coupling in a One-Dimensional Array of Belousov-Zhabotinsky Micro-Oscillators: Theory. *Physical Review E*, 84:066209:1–11, 2011.

[35] Yoshiki Kuramoto. Self-Entrainment of a Population of Coupled Non-Linear Oscillators. In Huzihiro Araki, editor, *International Symposium on Mathematical Problems in Theoretical Physics*, volume 39 of *Lecture Notes in Physics*, pages 420–422. Springer Berlin Heidelberg, 1975.

[36] Yoshiki Kuramoto. *Chemical Oscillations, Waves and Turbulence*. Springer, 1984.

[37] Michael Giver, Zahera Jabeen, and Bulbul Chakraborty. Phase and frequency entrainment in locally coupled phase oscillators with repulsive interactions. *Phys. Rev. E*, 83:046206, Apr 2011.

[38] F Julicher, K. Kruse, J Prost, and JF Joanny. Active behavior of the cytoskeleton. *Physics Reports-Review Section Of Physics Letters*, 449(1-3):3–28, 2007.

[39] John Toner, Yuhai Tu, and Sriram Ramaswamy. Hydrodynamics and Phases of Flocks. *Annals of Physics*, 318(1):170–244, 2005. Special Issue.

[40] E Karsenti. Self-Organization in Cell Biology: A Brief History. *Nature reviews. Molecular cell biology*, 9(3):255262, March 2008.

[41] Neil A Whitehead, Anne M.L. Barnard, Holly Slater, Natalie J.L. Simpson, and George P.C. Salmond. Quorum-Sensing in Gram-Negative Bacteria. *FEMS Microbiology Reviews*, 25(4):365–404, 2001.

[42] Andrej Vilfan and Frank Jülicher. Hydrodynamic Flow Patterns and Synchronization of Beating Cilia. *Phys. Rev. Lett.*, 96:058102, Feb 2006.

[43] Boris Guirao and Jean-François Joanny. Spontaneous Creation of Macroscopic Flow and Metachronal Waves in an Array of Cilia. *Biophysical Journal*, 92(6):1900–1917, 2007.

[44] Leon Glass. Synchronization and Rhythmic Processes in Physiology. *Nature*, 410:277–284, 2001.

[45] Stephen C. Pratt. Quorum Sensing by Encounter Rates in the Ant Temnothorax Albipennis. *Behavioral Ecology*, 16(2):488–496, 2005.

[46] Steven Strogatz. *Nonlinear Dynamics And Chaos: With Applications To Physics, Biology, Chemistry, And Engineering*. Westview Press, 1 edition, 2001.

[47] Arkady Pikovsky, Michael Rosenblum, and Jürgen Kurths. *Synchronization: A Universal Concept in Nonlinear Sciences*. Cambridge University Press, 1 edition, 2003.

[48] Thomas M. Massie, Bernd Blasius, Guntram Weithoff, Ursula Gaedke, and Gregor F. Fussmann. Cycles, Phase Synchronization, and Entrainment in Single-Species Phytoplankton Populations. *Proceedings of the National Academy of Sciences*, 107(9):4236–4241, 2010.

[49] Annette F. Taylor, Mark R. Tinsley, Fang Wang, Zhaoyang Huang, and Kenneth Showalter. Dynamical Quorum Sensing and Synchronization in Large Populations of Chemical Oscillators. *Science*, 323(5914):614–617, 2009.

[50] Taiji Okano, Akane Kitagawa, and Kenji Miyakawa. Array-Enhanced Coherence Resonance and Phase Synchronization in a Two-Dimensional Array of Excitable Chemical Oscillators. *Phys. Rev. E*, 76:046201, Oct 2007.

[51] Taiji Okano and Kenji Miyakawa. Feedback-Controlled Dynamics in a Two-Dimensional Array of Active Elements. *Phys. Rev. E*, 80:026215, Aug 2009.

[52] Laszlo Hegedus, Maria Wittmann, Zoltan Noszticzius, Shuhua Yan, Atchara Sirimungkala, Horst-Dieter Forsterling, and Richard J. Field. HPLC Analysis of Complete BZ Systems. Evolution of the Chemical Composition in Cerium and Ferroin Catalysed Batch Oscillators: Experiments and Model Calculations. *Faraday Discuss.*, 120:21–38, 2002.

[53] Tamas Turanyi, Laszlo Gyorgyi, and Richard J. Field. Analysis and Simplification of the GTF Model of the Belousov-Zhabotinskii Reaction. *The Journal of Physical Chemistry*, 97(9):1931–1941, 1993.

[54] Anatol M. Zhabotinsky, Frank Buchholtz, Anatol B. Kiyatkin, and Irving R. Epstein. Oscillations and Waves in Metal-Ion-Catalyzed Bromate Oscillating Reactions in Highly Oxidized States. *The Journal of Physical Chemistry*, 97(29):7578–7584, 1993.

[55] F W Schneider. Periodic Perturbations of Chemical Oscillators: Experiments. *Annual Review of Physical Chemistry*, 36(1):347–378, 1985.

[56] M. Dolník, I. Schreiber, and M. Marek. Dynamic Regimes in a Periodically Forced Reaction Cell with Oscillatory Chemical Reaction. *Physica D: Nonlinear Phenomena*, 21(1):78–92, 1986.

[57] Eugene M. Izhikevich. *Dynamical Systems in Neuroscience: The Geometry of Excitability and Bursting*. Computational Neuroscience. The MIT Press, 2010.

[58] Arthur T. Winfree. *The Geometry of Biological Time*, volume 12 of *Interdisciplinary Applied Mathematics*. Springer, 2 edition, 2001.

[59] Jun Miyazaki and Shuichi Kinoshita. Determination of a Coupling Function in Multicoupled Oscillators. *Phys. Rev. Lett.*, 96:194101, May 2006.

[60] Philip K. Maini, Ruth E. Baker, and Cheng-Ming Chuong. The Turing Model Comes of Molecular Age. *Science*, 314(5804):1397–1398, 2006.

[61] Masafumi Inaba, Hiroaki Yamanaka, and Shigeru Kondo. Pigment Pattern Formation by Contact-Dependent Depolarization. *Science*, 335(6069):677, 2012.

[62] J. Reinitz. Pattern Formation: Turing at 100. *Nature*, 482:2012, 2012.

[63] A. Gierer and H. Meinhardt. A Theory of Biological Pattern Formation. *Kybernetik*, 12:30–39, 1972.

[64] Shigeru Kondo and Takashi Miura. Reaction-Diffusion Model as a Framework for Understanding Biological Pattern Formation. *Science*, 329:1616–1620, 2010.

[65] P. Müller, K. W. Rogers, B. M. Jordan, J. S. Lee, D. Robson, S. Ramanathan, and A. F. Schier. Differential Diffusivity of Nodal and Lefty Underlies a Reaction-Diffusion Patterning System. *Science*, 336:721–724, 2012.

[66] Luis G. Morelli, Koichiro Uriu, Saul Ares, and Andrew C. Oates. Computational Approaches to Developmental Patterning. *Science*, 336:187–191, 2012.

[67] Vladimir K. Vanag and Irving R. Epstein. Diffusive instabilities in heterogeneous systems. *Journal of Chemical Physics*, 119(14):7297–7307, 2003.

[68] D. G. Aronson, G. B. Ermentrout, and N. Kopell. Amplitude Response of Coupled Oscillators. *Phys. D*, 41(3):403–449, 1990.

[69] Ryo Yoshida. Self-Oscillating Gels Driven by the Belousov-Zhabotinsky Reaction as Novel Smart Materials. *Advanced Materials*, 22(31):3463–3483, 2010.

[70] Ryo Yoshida, Toshikazu Takahashi, Tomohiko Yamaguchi, and Hisao Ichijo. Self-Oscillating Gel. *Journal of the American Chemical Society*, 118(21):5134–5135, 1996.

[71] Victor V. Yashin and Anna C. Balazs. Chemomechanical Synchronization in Heterogeneous Self-Oscillating Gels. *Phys. Rev. E*, 77:046210, Apr 2008.

[72] Olga Kuksenok, Pratyush Dayal, Amitabh Bhattacharya, Victor V. Yashin, Debabrata Deb, Irene C. Chen, Krystyn J. Van Vliet, and Anna C. Balazs. Chemo-Responsive, Self-Oscillating Gels that Undergo Biomimetic Communication. *Chem. Soc. Rev.*, 42:7257–7277, 2013.

[73] Pengfei Wang, Shaobao Liu, Jinxiong Zhou, Feng Xu, and Tianjian Lu. Kinetic Modelling and Bifurcation Analysis of Chemomechanically Miniaturized Gels under Mechanical Load. *The European Physical Journal E*, 36(9), 2013.

[74] Paul J. Flory. *Principles of Polymer Chemistry*. The George Fisher Baker Non-Resident Lectureship in Chemistry at Cornell University. Cornell University Press, 1 edition, 1953.

[75] Toyoichi Tanaka. Collapse of Gels and the Critical Endpoint. *Phys. Rev. Lett.*, 40:820–823, Mar 1978.

[76] Mitsuhiro Shibayama and Toyoichi Tanaka. Volume Phase Transition and Related Phenomena of Polymer Gels. In K. Dušek, editor, *Responsive Gels: Volume Transitions I*, volume 109 of *Advances in Polymer Science*. Springer Berlin Heidelberg, 1993.

[77] A. Yu. Grosberg and S. K. Nechaev. Topological Constraints in Polymer Network Strong Collapse. *Macromolecules*, 24(10):2789–2793, 1991.

[78] Ye Zhang, Ning Li, Jorge Delgado, Ning Zhou, Ryo Yoshida, Seth Fraden, Irving R. Epstein, and Bing Xu. Structural Modulation of Self-Oscillating Gels: Changing the Proximity of the Catalyst to the Polymer Backbone to Tailor Chemomechanical Oscillation. *Soft Matter*, 8:7056–7061, 2012.

[79] Ye Zhang, Ning Zhou, Ning Li, Megan Sun, Dongshin Kim, Seth Fraden, Irving R. Epstein, and Bing Xu. Giant Volume Change of Active Gels under Continuous Flow. *Journal of the American Chemical Society*, 136(20):7341–7347, 2014.

[80] Yoshiharu Hirose, Takayuki Amiya, Yoshitsugu Hirokawa, and Toyoichi Tanaka. Phase Transition of Submicron Gel Beads. *Macromolecules*, 20(6):1342–1344, 1987.

[81] Takamasa Sakai and Ryo Yoshida. Self-Oscillating Nanogel Particles. *Langmuir*, 20(4):1036–1038, 2004.

[82] Jingyi Shen, Srinivasa Pullela, Manuel Marquez, and Zhengdong Cheng. Ternary Phase Diagram for the Belousov-Zhabotinsky Reaction-Induced Mechanical Oscillation of Intelligent PNIPAM Colloids. *The Journal of Physical Chemistry A*, 111(48):12081–12085, 2007.

[83] Ryo Yoshida, Takamasa Sakai, Shoji Ito, and Tomohiko Yamaguchi. Self-Oscillation of Polymer Chains with Rhythmical Soluble-Insoluble Changes. *Journal of the American Chemical Society*, 124(27):8095–8098, 2002.

[84] Chi Wu and Shuiqin Zhou. Light Scattering Study of Spherical Poly(N-Isopropylacrylamide) Microgels. *Journal of Macromolecular Science-Physics*, B36(3):345–355, 1997.

[85] Jianzhong Wu, Gang Huang, and Zhibing Hu. Interparticle Potential and the Phase Behavior of Temperature-Sensitive Microgel Dispersions. *Macromolecules*, 36(2):440–448, 2003.

[86] Wayne McPhee, Kam Chiu Tam, and Robert Pelton. Poly(N-Isopropylacrylamide) Latices Prepared with Sodium Dodecyl Sulfate. *Journal of Colloid and Interface Science*, 156(1):24–30, 1993.

[87] Robert Pelton. Temperature-Sensitive Aqueous Microgels. *Advances in Colloid and Interface Science*, 85(1):1–33, 2000.

[88] John J. Tyson and Paul C. Fife. Target Patterns in a Realistic Model of the Belousov-Zhabotinskii Reaction. *The Journal of Chemical Physics*, 73(5), 1980.

[89] Wei Hong, Xuanhe Zhao, Jinxiong Zhou, and Zhigang Suo. A Theory of Coupled Diffusion and Large Deformation in Polymeric Gels. *Journal of the Mechanics and Physics of Solids*, 56(5):1779–1793, 2008.

[90] Jiaping Zhang, Xuanhe Zhao, Zhigang Suo, and Hanqing Jiang. A Finite Element Method for Transient Analysis of Concurrent Large Deformation and Mass Transport in Gels. *Journal of Applied Physics*, 105(9):093522, 2009.

[91] Amélie Burel. Numerical Implementation of a Non-Linear Constitutive Equations for Hydrogels. *Master's thesis*, 2009.